UNIVERSITY OF CALIFORNIA, SAN DIEGO

Hyperbolic metamaterials for high-speed optical communications

A dissertation submitted in partial satisfaction of the
requirements for the degree
Doctor of Philosophy

in

Materials Science and Engineering

by

Lorenzo Ferrari

Committee in charge:

Professor Zhaowei Liu, Chair
Professor Eric E. Fullerton
Professor Boubacar Kanté
Professor Donald J. Sirbuly
Professor Andrea R. Tao

2017

The dissertation of Lorenzo Ferrari is approved, and it is acceptable in quality and form for publication on microfilm and electronically:

_____

_____

_____

_____

_____

Chair

University of California, San Diego

2017

DEDICATION

To Maria Grazia, Gabriele and Alessandro.

EPIGRAPH

Ma l'impresa eccezionale, dammi retta

è essere normale.

—Lucio Dalla

TABLE OF CONTENTS

LIST OF FIGURES

LIST OF TABLES

ACKNOWLEDGEMENTS

I would like to warmly thank my advisor, Prof. Zhaowei Liu, for his guidance and his support throughout my PhD. His unresting mind and unconstrained curiosity have been a powerful source of inspiration, and a stimulus to always think forward and never miss the big picture. He introduced me to the field of plasmonics and hyperbolic metamaterials, and shaped my approach to theoretical and experimental study with rigorous feedback. From him I learned how to critically evaluate my research strategies, establishing goals that are both physically sound and practically achievable when time and resources must be wisely allocated. His attention for group management, with a strong emphasis on brainstorming and collective idea sharing, is a precious example for my professional growth.

I am very grateful to Prof. Eric E. Fullerton, Prof. Boubacar Kanté, Prof. Donald J. Sirbuly and Prof. Andrea R. Tao for serving on my PhD committee. I owe a substantial part of my achievements to their guidance and to their generous sharing of experimental and hardware resources. This dissertation would not be possible without the fruitful discussions and collaborations that I had with them and their group members. From Prof. Fullerton's group, I would like to thank Dr. Sergio Montoya, Dr. Sohini Manna, Tyler Hennen, Dr. Rajasekhar Medapalli, Dr. Dokyun Kim, Robert Tolley, Sheena Patel and Haowen Ren. I would like to express my gratitude to Dr. Conor Riley and Dr. Qian Huang from Prof. Sirbuly's group, and to Dr. Matthew Rozin and Dr. Tyler Dill from Prof. Tao's group.

I had the pleasure to share my PhD years with brilliant labmates, who helped me learn experimental techniques and provided weekly feedback and discussion. My previous and current group fellows are Dr. Joseph L. Ponsetto, Dr. Dylan Lu, Dr. Conor Riley, Dr. Feifei Wei, Dr. Hao Shen, Dr. Yuzhe Xiao, Dr. Dominic Lepage, Dr. Bahar Khademhosseinieh, Dr. Conrad Rizal, Dr. Wenwei Zheng, Dr. Justin Park, Kangwei

Wang, Jie Zhao, Dongwon Park, Yunfeng Jiang, Huan Hu, Devin Cela, Werner Jiang, Bryan VanSaders, Joshua Hoemke, Dr. Anna Bezryadina, Eric Huang, Haoliang Qian, Qian Ma, Li Chen, Jeff Chen, Junxiang Zhao, Tiansong Zhang and Sonika Obheroi.

Hardware support and experienced advice in dealing with GaN LEDs were provided to me by the "MOCVD team", including Prof. Paul K. Yu, Prof. Shadi Dayeh, Atsunori Tanaka, Kangwei Wang and Lorraine Hossain. I am also grateful to Prof. Yeshaiahu "Shaya" Fainman and his group members Dr. Joseph S. T. Smalley, Dr. Felipe Vallini, Dr. Qing Gu and Dr. Abdelkrim El Amili for our discussions and collaborations.

Serving as a teaching assistant for Prof. Ertugrul Cubukcu, in coordination with the other teachers and TA's of the NANO120B course including Prof. David Fenning, Prof. Jian Luo, Prof. Donald J. Sirbuly, Grace Luo, Spencer Ward and Weidong Xiao, challenged and improved my capability of communicating science and effectively managing student teams.

I would like to thank for their support the current and former Chairs of the Materials Science and Engineering Program, Prof. Prabhakar R. Bandaru and Prof. Sungho Jin, and the current and former Graduate Program Advisors, Katie Hamilton and Charlotte Lauve. Ordering experimental equipment and solving logistic issues were made easier by the experience of our ECE Faculty Assistants, Tawnee Gomez, Stefanie Battaglia and Julie Moritz. I am especially grateful to the Director of the Center for Memory and Recording Research (CMRR), Prof. Eric E. Fullerton, for having hosted me and always kindly answered my research questions. I would like to extend my thankfulness to CMRR Business Officer Iris Villanueva, Fund Manager Marina Robenko and Administrative Assistant Agapi "Gabby" Tshamjyan.

The UCSD Nano3 cleanroom boasts a unique mix of experts, who helped me develop and refine my nanofabrication processes with patience and competence. I would like to thank the Director, Dr. Bernd Fruhberger, and the staff, including Ryan Anderson,

Larry Grissom, Sean Parks, Dr. Xuekun Lu, Hal Romans, Dr. Jeff Wu and Ivan Harris.

I am grateful to the current and former Directors of the von Liebig Entrepreneurism Center of the Jacobs School of Engineering, Dennis Abremski and Dr. Rosibel Ochoa, and to the staff, including Jay Gilberg, Dr. Jay Kunin, Kai Wenk-Wolff, Dr. Robert Logan, Mark Leibowitz, Dr. Lori Deaton, Dr. Albert Liu, Lynn Bautista, Jennifer Yturralde, Executive Entrepreneur in Residence Larry Morgan, and my mentors John Kohut and Chris Rowan. I also greatly appreciated the help of Victoria Cajipe and Briana Weisinger from the UCSD Office of Innovation and Commercialization.

I would like to thank all the officers of UCSD Graduate Division. In particular, I am thankful to Assistant Dean and Director April Bjornsen for having provided me help and support in a moment of need. I fruitfully worked with Student Affairs Officer Shana Slebioda and Program Manager Sara Danford; I appreciated the teaching of Richard Mayhew and Dragos Craciun, and the collaboration with the Director of the UCSD International Faculty and Scholar Office, Dr. Roark Miller.

I would also like to express once again my gratitude to Prof. Claudio Oleari (University of Parma), who supervised my undergraduate thesis work, and Prof. Paolo Milani (University of Milan) and Dr. Vojislav Srdanov (University of California, Santa Barbara) who supervised my Master's thesis work.

The present dissertation is dedicated to my mother, Maria Grazia, my father, Gabriele, and my brother, Alessandro. Growing up I received from them the silent gift of example, which enlightened the not always linear path of my PhD. The work ethics and the human values that I learned from them, together with the stubbornness of smiling at difficulties, are the live roots that connect us and keep inspiring my life.

Chapters 1 and 2, in part, are a reprint of the material as it appears on Progress in Quantum Electronics 40, 1–40 (2015). L. Ferrari, C. Wu, D. Lepage, X. Zhang and Z.

Liu, “Hyperbolic metamaterials and their applications”. The dissertation author is the first author of this paper.

Chapters 1 and 5 and Appendix A, in part, have been submitted for publication. L. Ferrari, J. S. T. Smalley, Y. Fainman and Z. Liu, “Hyperbolic metamaterials for dispersion-assisted directional light emission”. The dissertation author is the first author of this paper.

Chapter 3, in part, is a reprint of the material as it appears on Optics Express 22, 4301–4306 (2014). L. Ferrari, D. Lu, D. Lepage, Z. Liu, “Enhanced spontaneous emission inside hyperbolic metamaterials”. The dissertation author is the first author of this paper.

Chapter 6 and Appendix B, in part, are being prepared for submission for publication. L. Ferrari, J. S. T. Smalley, H. Qian, A. Tanaka, D. Lu, S. Dayeh, Y. Fainman and Z. Liu, “Design and analysis of blue InGaN/GaN plasmonic LED for high-speed, high-efficiency optical communications”. The dissertation author is the co-first author of this paper.

VITA

2007	B. S. in Physics, Università degli Studi di Parma, Italy
2010	M. S. in Physics, Università degli Studi di Milano, Italy
2011	Researcher in the Sterilisation and Hygienic Systems group, Tetra Pak, Modena, Italy
2012	M. S. in Materials Science and Engineering, University of California, San Diego
2011-2017	Graduate Research Assistant, University of California, San Diego
2016	Graduate Teaching Assistant, Department of Nanoengineering, University of California, San Diego
2017	Ph. D. in Materials Science and Engineering, University of California, San Diego

PUBLICATIONS

L. Ferrari, J. S. T. Smalley, H. Qian, A. Tanaka, D. Lu, S. Dayeh, Y. Fainman and Z. Liu, "Design and analysis of blue InGaN/GaN plasmonic LED for high-speed, high-efficiency optical communications", paper in preparation.

Q. Ma, H. Qian, W. Bao, S. Montoya, **L. Ferrari**, H. Hu, E. E. Fullerton, X. Zhang and Z. Liu, "Metamaterial spatial-to-spectral transformation microscopy", paper in preparation.

L. Ferrari, J. S. T. Smalley, Y. Fainman and Z. Liu, "Hyperbolic metamaterials for dispersion-assisted directional light emission", paper submitted.

J. Ponsetto, A. Bezryadina, F. Wei, K. Onishi, H. Shen, E. Huang, **L. Ferrari**, Q. Ma, Y. Zou and Z. Liu, "Experimental demonstration of localized plasmonic structured illumination microscopy", *ACS Nano* (2017).

H. Shen, L. Chen, **L. Ferrari**, M.-H. Lin, N. A. Mortensen, S. Gwo and Z. Liu, "Optical observation of plasmonic nonlocal effects in a 2D superlattice of ultrasmall gold nanoparticles", *Nano Letters* 17, 2234–2239 (2017).

J. S. T. Smalley, F. Vallini, S. Montoya, **L. Ferrari**, S. Shahin, C. T. Riley, B. Kanté, E. E. Fullerton, Z. Liu and Y. Fainman, "Luminescent Hyperbolic Metasurfaces", *Nature Communications* 8, 13793 (2017).

L. Ferrari, C. Wu, D. Lepage, X. Zhang and Z. Liu, "Hyperbolic metamaterials and their applications", *Progress in Quantum Electronics* 40, 1–40 (2015).

D. Lu, **L. Ferrari**, J. J. Kan, E. E. Fullerton, and Z. Liu, "Nanopatterned multilayer hyperbolic metamaterials for spontaneous light emission control", paper in preparation.

L. Ferrari, D. Lu, D. Lepage, Z. Liu, "Enhanced spontaneous emission inside hyperbolic metamaterials", *Optics Express* 22, 4301–4306 (2014).

L. Ferrari, "Determination of the enthalpies of sublimation from absorbance data: application to organic semiconductors", *Master Thesis*, Supervisors: Dr. Vojislav Srdanov (University of California, Santa Barbara), Prof. Paolo Milani (Università degli Studi di Milano) (2010).

L. Ferrari, "Characterization of pigments and formulation of dyes in the industrial world according to the Kubelka-Munk model", *Bachelor Thesis*, Supervisor: Prof. Claudio Oleari (Università degli Studi di Parma) (2007).

ABSTRACT OF THE DISSERTATION

Hyperbolic metamaterials for high-speed optical communications

by

Lorenzo Ferrari

Doctor of Philosophy in Materials Science and Engineering

University of California, San Diego, 2017

Professor Zhaowei Liu, Chair

Hyperbolic metamaterials are a class of artificial optical media characterized by anisotropic light dispersion. Their unprecedented properties, unattainable with natural materials, can be controlled and tuned over the entire optical range with careful design of their subwavelength units. Among the applications enabled by hyperbolic media, spontaneous emission engineering occupies a prominent position for optical communications. Coupling of an incoherent optical source with a hyperbolic nanostructure results in shortened spontaneous emission lifetime, corresponding to increased modulation bandwidth. This thesis explores solutions to enhance the spontaneous emission, the output power, the directionality and the electronic integrability of emitter-hyperbolic medium systems.

After a solid compendium of the hyperbolic metamaterials field is provided, a method to enhance the Purcell factor of a multilayer Si/Ag hyperbolic medium is proposed. Moving the emitter location from the outside to the inside of the multilayer results in a 300-fold Purcell enhancement at visible frequencies, and up to 10-fold power enhancement with respect to free space is obtained by means of 1D gratings. The study then focuses on improving the directional control of power outcoupling, either by shaping the hyperbolic medium into a cylindrical nanoantenna, or by introducing a novel paradigm based on dispersion engineering, which lifts the need for gratings or nanostructures. Design guidelines are provided to achieve emission from the top or from the side of an unpatterned hyperbolic block, and a dipole-hyperbolic block system is optimized for lateral outcoupling at $\lambda_0 = 530$ nm. Finally, the integration of a plasmonic nanostructure (which can be seen as a special case of hyperbolic nanostructure with 100% metallic component) with an InGaN/GaN LED is addressed. The proposed architecture enables simultaneous high-speed modulation and efficient light emission while preserving effective electrical excitation. Different plasmonic LED structures operating at $\lambda_0 = 450$ nm are fabricated, and characterized with time-resolved photoluminescence. A limit 2 GHz modulation bandwidth is predicted based on lifetime measurements. A subsequent cross-sectional analysis identifies the nanostructure geometry that maximizes light extraction, providing a clear guideline for future fabrication and contact integration.

Chapter 1

Introduction

1.1 Genesis of hyperbolic metamaterials

In the past decade, the development of nanofabrication techniques allowed the experimental demonstration of various kinds of optical metamaterials, designed to exhibit properties unattainable with conventional media [1]. The initial efforts were motivated by the predictions of Veselago, who in the late 1960s had envisioned a material with negative refractive index [2], a feature thus far believed to be irrealistic and - as such - of no physical relevance. His studies led eventually to artificial media exhibiting negative refraction [3], and to a critical reexamination of other paradigms in electromagnetism and related fields.

Among the varieties of metamaterials proposed and fabricated since then, hyperbolic metamaterials (HMMs) have rapidly gained a central role in nanophotonics, thanks to their unprecedented ability to access and manipulate the near-field [1] of a light emitter or a light scatterer. This feature derives directly from the excitation, inside of

[1] The *near-field* is defined by distances shorter than the wavelength of light in vacuum. Within this spatial domain, the electromagnetic field manifests a behavior that may significantly deviate from the conventional one, valid at distances much larger than one wavelength (*far-field*).

HMMs, of coupled surface plasmons (SPs) [4, 5, 6, 7, 8]. A SP is a collective oscillation of electrons, confined to the surface of a metal in contact with a dielectric. If the metal and the dielectric are shaped as thin layers, their interface is flat, and the metal surface supports *propagating* surface plasmons (or "surface plasmon polaritons" (SPPs)). If instead the metal has the shape of a nanoparticle or a nanowire, the surface of the metallic domain supports *localized* surface plasmons. The excitation of these coherent electronic vibrations is accompanied by the generation of an electromagnetic field. The latter decays very fast on both the dielectric and the metallic side, and thereby interacts principally with the near-field of the interface. When sub-wavelength metallic/dielectric layers are periodically stacked, or metallic nanowires are regularly arranged with sub-wavelength separation in a dielectric matrix, the electromagnetic fields bounded to the individual plasmonic interfaces couple, giving rise to a collective response. Such response can be interpreted, in the limit of infinite number of interfaces, as originating from bulk effective media, with a unique anisotropic dispersion, termed hyperbolic. The interaction of these metamaterials with their near-field results in applications including high-resolution imaging and lithography [9, 10, 11, 12], broadband absorption engineering [13, 14], thermal control at the nanoscale [15], enhanced nonlinear processes [16, 17] and spontaneous emission engineering [18, 19]. The work presented in this thesis focuses on the latter, emphasizing its ultimate link to fast optical data transfer.

1.2 Hyperbolically-enhanced incoherent light sources

The capability of controlling spontaneous emission is technologically relevant to the field of high-speed optical communications. As pointed out in a recent work [20], incoherent light sources with a spontaneous emission rate enhanced via plasmonic [21, 22, 23] or hyperbolic nanostructures can achieve modulation speeds comparable

to or larger than those of coherent sources, at a lower manufacturing and operational cost. The radiative spontaneous decay rate of a quantum emitter (molecule, electron-hole pair in quantum wells (QWs) or quantum dots (QDs)) $\gamma_r = 1/\tau_r$, where τ_r represents the radiative spontaneous emission lifetime [24], defines the upper bound to the 3dB electrical modulation bandwidth, f_{3dB}, of a light-emitting diode (LED), according to the formula $f_{3dB} = (2\pi\tau_r)^{-1} = (2\pi)^{-1}\gamma_r$ [25]. When such a quantum light source is brought within the near field of a HMM, the waves with large k-vectors contained in its emission spectrum couple to the hyperbolic medium – which supports their propagation – instead of decaying evanescently in the surrounding environment (usually air). The local photonic density of states (PDOS) accessible to the emitter is therefore much larger in HMMs than in conventional media. Fermi's Golden Rule states that the enhancement in PDOS, quantified by the Purcell factor, is proportional to the enhancement in radiative spontaneous decay rate [26]: because γ_r is proportional to f_{3dB} as shown above, we conclude that the emitter-HMM coupling enhances the electrical modulation bandwidth. The contextual increase in the data transmission rate of the emitter (proportional to f_{3dB} according to the Shannon Sampling Theorem [25]) opens up a host of opportunities in high-speed wireless (Light-Fidelity (Li-Fi) [27], underwater [28]) and fiber-optic [29] communication.

The path from the first experimental demonstrations of hyperbolic emission enhancement to the commercialization of hyperbolically-engineered light sources is not straightforward. Several key challenges need to be addressed, in order to boost the performance of HMMs, increase their functionality and integrability and enable their mass production. What is the location of an emitter relative to a HMM that maximizes its decay rate? Are there nanostructures simultaneously capable of extracting radiation from HMMs and controlling its directionality? Is a grating the only feasible light outcoupling mechanism? Which design allows the effective integration of electrically

pumped emitters and HMMs, enhancing the emitter's modulation speed but maintaining a reasonable radiation intensity? These and other questions are answered in the following chapters, also in light of the recent progress in photonic materials research.

1.3 Thesis content

The present thesis provides a comprehensive review of HMMs theory and applications, showing how their unprecedented properties enable novel advances in nanophotonics. It then focuses on the interaction between HMMs and quantum light emitters, analyzing its two main aspects: spontaneous emission enhancement and directional radiation outcoupling. Finally, it proposes and experimentally evaluates a viable solution to integrate emitter and hyperbolic medium into a light-emitting device capable of high-speed modulation.

Here in Chapter 1 we have framed our study into its technology perspective: the unique behavior of HMMs can be leveraged to enhance the modulation speed of an incoherent light source, ultimately yielding an optical transmitter capable to compete with lasers in specific contexts and operative conditions.

In Chapter 2 we introduce the concept of hyperbolic medium, describing the physical properties that result from its peculiar optical dispersion. The two practical implementations of HMM, the multilayer (ML) stack and the nanowire (NW) array, are successively discussed, together with their constituent materials - whose choice is dictated by the operational spectral range - and their fabrication methods. Once such background is provided, the chapter reviews the main applications of HMMs emerged so far in literature: high-resolution imaging and lithography, spontaneous emission engineering, thermal emission engineering, and active and tunable devices. The picture is complemented by a miscellanea of less established related topics (enhanced absorption,

waveguiding, optical forces). We conclude by critically evaluating the limitations of the current theoretical approach, both in a classical framework and when the HMM feature size approaches the domain of quantum physics.

Chapter 3 is devoted to spontaneous emission (SE) enhancement with HMMs. We investigate how the decay rate of an emitter, already enhanced by its proximity to the surface of a multilayer HMM, is further boosted when its location is moved from the outside to the inside of the hyperbolic medium. Once the optimum position is identified, two grating geometries are proposed to effectively extract radiation from the multilayer into the far field.

Chapters 4 and 5 are devoted to directional radiation outcoupling from HMMs. In Chapter 4, a HMM coupled to a quantum source is shown to possess directional emission properties when shaped into a cylindrical nanoantenna. We observe that, for a given antenna geometry, certain emitter locations and wavelengths correspond to directional emission patterns, parallel or perpendicular to the antenna axis. Chapter 5 provides a novel paradigm for radiation outcoupling from HMMs, based on dispersion engineering. If the filling fraction of a hyperbolic medium is properly selected, light extraction is achieved without the need for a grating, for any HMM type (I or II) and geometry (multilayer or nanowire).

In Chapter 6 we discuss the fabrication of an optical source, operating in the visible range, whose electrical modulation speed is plasmonically/hyperbolically enhanced. We integrate in a custom-grown GaN wafer Ag nanostructures with different geometric parameters, to simultaneously optimize both decay rate and light extraction efficiency.

We summarize the results of our work in Chapter 7, emphasizing the significance of this study for future research directions.

Chapter 1, in part, is a reprint of the material as it appears on Progress in Quantum

Electronics 40, 1–40 (2015). L. Ferrari, C. Wu, D. Lepage, X. Zhang and Z. Liu, "Hyperbolic metamaterials and their applications". The dissertation author is the first author of this paper.

Chapter 1, in part, has been submitted for publication. L. Ferrari, J. S. T. Smalley, Y. Fainman and Z. Liu, "Hyperbolic metamaterials for dispersion-assisted directional light emission". The dissertation author is the first author of this paper.

Chapter 2

Fundamentals and applications of HMMs

2.1 Introduction

This chapter reviews the conceptual and experimental milestones that established and consolidated the field of hyperbolic metamaterials, together with the latest trends. We focus our analysis on devices intended to work at optical frequencies, which span the ultraviolet, visible, near- and mid-infrared range. We start in Section 2.2 by introducing the properties of an ideal hyperbolic medium, and the physical phenomena that they determine (Subsection 2.2.1). Two artificial structures have been shown to possess effective hyperbolic dispersion: a multilayer stack and a nanowire array. We provide formulas describing the respective effective parameters and discuss their validity, also evaluating suitable material combinations (Subsection 2.2.2). Section 2.3 examines the most promising areas of application of HMMs. These media support the propagation of high wavevectors, a characteristic which can be exploited to break the diffraction limit. The ability of resolving sub-wavelength objects has been predicted and demonstrated with the

invention of the hyperlens, that we discuss alongside its implications for nanolithography in Subsection 2.3.1. HMMs can enhance the spontaneous emission of quantum sources by offering a fast decay channel with tunable and broadband features (Subsection 2.3.2). In an analogous fashion, hyperbolic modes in the infrared can increase heat transfer and lead to a super-planckian thermal emission in the near-field (Subsection 2.3.3). The possibility of implementing gain and mechanisms of dynamical tuning in HMMs is considered in Subsection 2.3.4, while Subsection 2.3.5 presents a miscellanea of emerging directions including enhanced absorption, waveguiding and optical forces. In Section 2.4 we highlight the limitations of classical hyperbolic medium models, and observe how a quantum treatment of the HMM constituent units necessarily results in spatial dispersion. A critical analysis of the limitations of HMMs and of future directions concludes our work.

2.2 Hyperbolic media

2.2.1 Definition and properties

The concept of a material with hyperbolic behavior originates from the optics of crystals. In such media, the constitutive relations connecting the electric displacement **D** and the magnetic induction **B** to the electric and magnetic fields **E** and **H** can be written

$$\mathbf{D} = \varepsilon_0 \bar{\bar{\varepsilon}} \mathbf{E} \tag{2.1}$$

$$\mathbf{B} = \mu_0 \bar{\bar{\mu}} \mathbf{H}, \tag{2.2}$$

where ε_0 and μ_0 are the vacuum permeability and permittivity, and $\bar{\bar{\varepsilon}}$ and $\bar{\bar{\mu}}$ are the relative

permeability and permittivity tensors. Throughout the present work we will consider nonmagnetic media, so that $\overline{\overline{\mu}}$ simply reduces to the unit tensor. Upon diagonalization, $\overline{\overline{\varepsilon}}$ assumes the form

$$\overline{\overline{\varepsilon}} = \begin{bmatrix} \varepsilon_{xx} & 0 & 0 \\ 0 & \varepsilon_{yy} & 0 \\ 0 & 0 & \varepsilon_{zz} \end{bmatrix}, \tag{2.3}$$

in a Cartesian frame of reference oriented along the so-called *principal axes* of the crystal. The three diagonal components are all positive, and in general depend on the angular frequency ω; the crystal is termed *biaxial* when $\varepsilon_{xx} \neq \varepsilon_{yy} \neq \varepsilon_{zz}$, *uniaxial* when $\varepsilon_{xx} = \varepsilon_{yy} \neq \varepsilon_{zz}$, and becomes *isotropic* when $\varepsilon_{xx} = \varepsilon_{yy} = \varepsilon_{zz}$.

To determine the dispersion relation of light in a medium described by Eq. (2.3), let us consider the following two Maxwell's equations in the absence of sources:

$$\nabla \times \mathbf{E} = -\frac{\partial \mathbf{B}}{\partial t} \tag{2.4}$$

$$\nabla \times \mathbf{H} = \frac{\partial \mathbf{D}}{\partial t}, \tag{2.5}$$

where $\mathbf{D}$ and $\mathbf{B}$ are as in Eq. (2.1) and Eq. (2.2). By inserting into Eq. (2.4) and Eq. (2.5) the plane wave expressions $\mathbf{E} = \mathbf{E}_0 e^{i(\omega t - \mathbf{k}\cdot\mathbf{r})}$ and $\mathbf{H} = \mathbf{H}_0 e^{i(\omega t - \mathbf{k}\cdot\mathbf{r})}$, where $\mathbf{k}$ is the wavevector, we obtain:

$$\mathbf{k} \times \mathbf{E} = \omega \mu_0 \mathbf{H} \tag{2.6}$$

$$\mathbf{k} \times \mathbf{H} = -\omega\varepsilon_0\bar{\bar{\varepsilon}}\mathbf{E}. \tag{2.7}$$

Substitution of Eq. (2.6) into Eq. (2.7) yields the eigenvalue problem for the electric field **E**:

$$\mathbf{k} \times (\mathbf{k} \times \mathbf{E}) + \omega^2\mu_0\varepsilon_0\bar{\bar{\varepsilon}}\mathbf{E} = 0, \tag{2.8}$$

which can be developed in matrix form:

$$\begin{bmatrix} k_0^2\varepsilon_{xx} - k_y^2 - k_z^2 & k_xk_y & k_xk_z \\ k_xk_y & k_0^2\varepsilon_{yy} - k_x^2 - k_z^2 & k_yk_z \\ k_xk_z & k_yk_z & k_0^2\varepsilon_{zz} - k_x^2 - k_y^2 \end{bmatrix} \begin{bmatrix} E_x \\ E_y \\ E_z \end{bmatrix} = 0, \tag{2.9}$$

where $k_0 = \omega/c$ is the magnitude of wavevector and $c = 1/\sqrt{\varepsilon_0\mu_0}$ the speed of light in vacuum. We now focus our attention on uniaxial media, with optical axis oriented along the $\hat{\mathbf{z}}$ direction, $\varepsilon_{xx} = \varepsilon_{yy} \equiv \varepsilon_\perp$ and $k_\perp = \sqrt{k_x^2 + k_y^2}$. The imposition of nontrivial solutions to Eq. (2.9) leads to the dispersion relation:

$$\left(k_\perp^2 + k_z^2 - \varepsilon_\perp k_0^2\right)\left(\frac{k_\perp^2}{\varepsilon_{zz}} + \frac{k_z^2}{\varepsilon_\perp} - k_0^2\right) = 0. \tag{2.10}$$

When set to zero, the two terms above correspond respectively to a spherical and an ellipsoidal isofrequency surface in the k-space; the first describes waves polarized in the *xy* plane (*ordinary* or *TE waves*), the second waves polarized in a plane containing the

optical axis (*extraordinary* or *TM waves*).

The situation changes substantially if we assume an extreme anisotropy, namely if one between $\varepsilon_\perp$ and ε_{zz} is negative. Media with such an optical signature are termed *indefinite* from the point of view of algebra [30], since their permittivity tensor represents an indefinite nondegenerate quadratic form, and exhibit a number of unconventional properties. Permittivity components with an opposing sign result in a hyperboloidal isofrequency surface for the extraordinary polarization - hence the physical denomination *hyperbolic* media. As a consequence, waves with arbitrarily large wavevectors retain a propagating nature, while in isotropic materials they become evanescent due to the bounded isofrequency contour [24]. The choice $\varepsilon_\perp > 0$, $\varepsilon_{zz} < 0$ corresponds to a two-fold hyperboloid, and the hyperbolic medium is called *dielectric* (with reference to its behavior in the *xy* plane) [31] or *Type I* [32]; the choice $\varepsilon_\perp < 0$, $\varepsilon_{zz} > 0$ describes a one-fold hyperboloid, namely a *metallic* or *Type II* medium. Fig. 2.1 shows the isofrequency surfaces and the dispersion relation for the two cases.

Another unique feature of a hyperbolic environment is the strongly directional light emission. The group velocity $\mathbf{v}_g(\omega) = \nabla_{\mathbf{k}}\omega(\mathbf{k})$ and the time-averaged Poynting vector $\hat{\mathbf{S}} = \frac{1}{2}Re\{\mathbf{E} \times \mathbf{H}^*\}$, associated respectively with the directions of *propagation* and *energy flow* of light rays, are orthogonal to the isofrequency surfaces [34, 30, 33]. Let us consider a section of the metallic-type hyperboloid in the $k_x k_z$ plane, illustrated in Fig. 2.2. Except for a small region in proximity of the origin, the normals to the hyperbola coincide with those to its asymptotes, defined by:

$$k_z = \pm\sqrt{-\frac{\varepsilon_\perp}{\varepsilon_{zz}}}k_\perp. \tag{2.11}$$

Therefore, electromagnetic radiation and energy travel preferentially along a *cone*, with axis coincident with the optical axis $\hat{\mathbf{z}}$ and half-angle

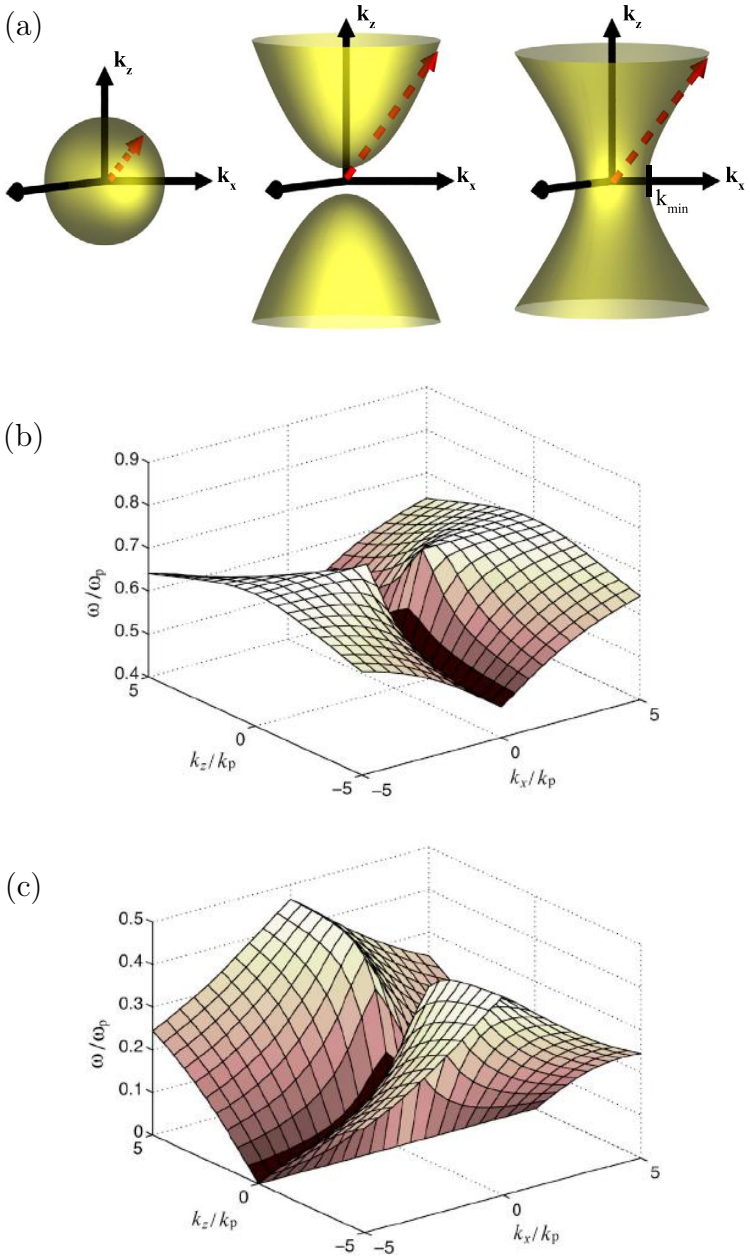

Figure 2.1: (a) Isofrequency surface $\omega(k_x, k_y, k_z) = \text{const.}$ in the tridimensional k-space for an isotropic medium ($\varepsilon_\perp, \varepsilon_{zz} > 0$) and a hyperbolic medium with dielectric or Type I ($\varepsilon_\perp > 0, \varepsilon_{zz} < 0$) and metallic or Type II ($\varepsilon_\perp < 0, \varepsilon_{zz} > 0$) response. (b) Dispersion relation $\omega(k_x, k_z)$ for a hyperbolic medium in the dielectric and (c) metallic regime. k_p is the wavevector correspondent to the plasma frequency ω_p of the metallic constituent (see Subsection 2.2.2). (a) reproduced from Ref. [32], (b) and (c) from Ref. [33].

$$\theta = arctan\left(\sqrt{-\frac{\varepsilon_{\perp}}{\varepsilon_{zz}}}\right). \tag{2.12}$$

Such a spatial grouping of light is forbidden in conventional dielectric media, described by spherical or ellipsoidal isofrequency surfaces: in that case the normals point in all directions, resulting in isotropic emission patterns.

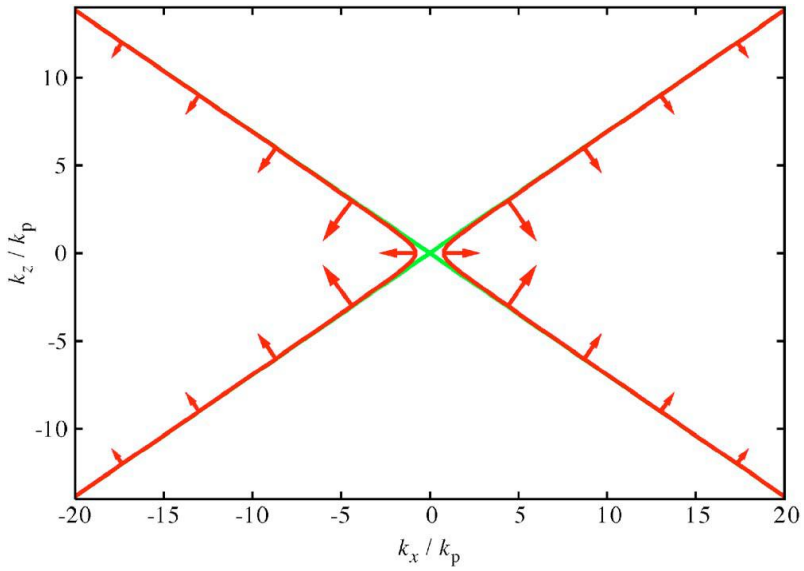

Figure 2.2: Isofrequency contour in the k_x, k_z plane at $\omega = 0.2\omega_p$ for the dielectric-type hyperbolic medium of Fig. 2.1(c). The group velocity is directed as the arrows and proportional to their magnitude, the green straight lines are the asymptotes given by Eq. (2.11). Reproduced from Ref. [33].

The peculiar anisotropic character does not manifest itself only in the bulk of hyperbolic media, but also at the interface with dielectrics, enabling negative refraction of energy [35, 36]. With reference to Fig. 2.3, let us consider an isotropic material, where $\mathbf{k}$ and $\hat{\mathbf{S}}$ are parallel, in contact with a hyperbolic medium of the dielectric type ($\varepsilon_{\perp} > 0$ and $\varepsilon_{zz} < 0$). We want to determine the refraction of a TM-polarized plane wave (electric field in the xz plane), with x-component of the wavevector $k_x > 0$, impinging from the isotropic side on the interface between the two media, lying in the xy plane. The fact that

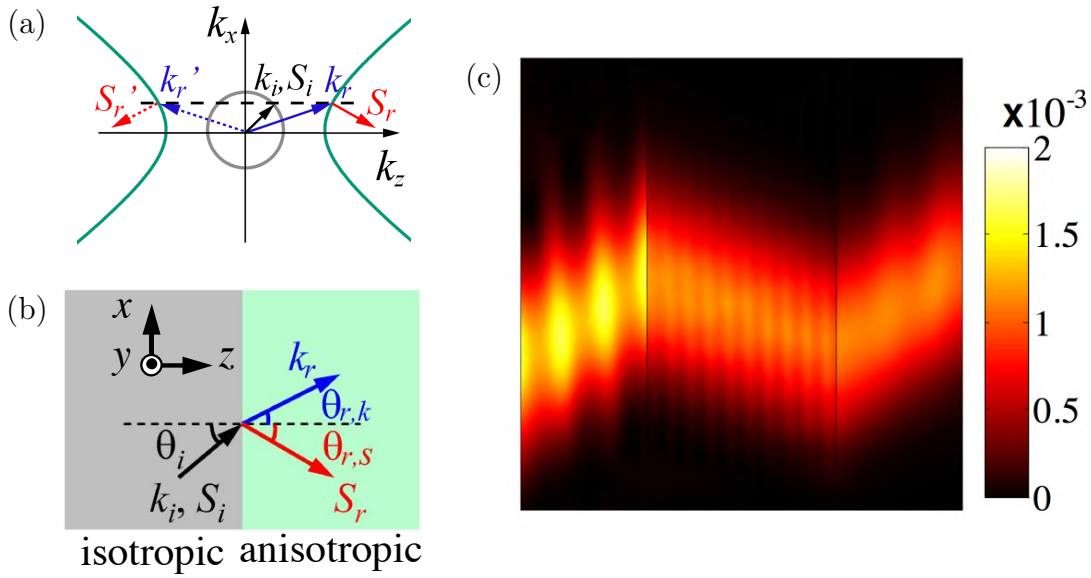

Figure 2.3: (a) Isofrequency contour of an indefinite material with $\varepsilon_{xx} = 4.515$ and $\varepsilon_{zz} = -2.530$ (green hyperbola), and of an isotropic material (gray circle). Light incident from an isotropic medium, where the vavevector $\mathbf{k}_i$ and the Poynting vector $\mathbf{S}_i$ are parallel (black arrow), can generate in a hyperbolic medium two possible sets (solid and dashed arrows) of refracted wavevector (blue)/ Poynting vector (red), both satisfying Eq. (2.13) and the conservation of the k-component tangential to the interface. The physically correct one (b) is selected by invoking the causality principle. (c) Finite-element simulation showing negative refraction of a TM Gaussian beam at $\lambda_0 = 632.8$ nm through a slab of hyperbolic medium. The color bar represents the time-averaged Poynting vector. Reproduced from Ref. [35].

in the anisotropic half-space k_x and k_z are connected by

$$\frac{k_x^2}{\varepsilon_{zz}} + \frac{k_z^2}{\varepsilon_{\perp}} = k_0^2, \tag{2.13}$$

namely $\mathbf{k}$ is constrained to the hyperbolic contour, and the conservation of the tangential component k_x, following from the absence of optical discontinuities in the xy plane, restrict the refracted wavevector to one between the dashed and the solid blue arrow in Fig. 2.3(a). Furthermore, the causality principle requires that $\hat{S}_z > 0$ (the energy flux has to be away from the interface): and only the solid blue arrow satisfies

$$\hat{S}_z = \frac{\hat{\mathbf{z}} \cdot \mathbf{k}}{\varepsilon_\perp} \frac{H_0^2}{2\omega\varepsilon_0} > 0. \tag{2.14}$$

This selected orientation implies that the wavevector, representing the propagation of phase fronts, undergoes positive refraction at the interface (Fig. 2.3(b)). If we evaluate instead the tangential component of $\hat{\mathbf{S}}$,

$$\hat{S}_x = \frac{k_x}{\varepsilon_{zz}} \frac{H_0^2}{2\omega\varepsilon_0}, \tag{2.15}$$

it results < 0, since the conserved quantity $k_x > 0$ while $\varepsilon_{zz} < 0$. This means that the sign of $\hat{S}_x$ flips across the interface (Fig. 2.3(b)), and hence that energy is negatively refracted when passing from an isotropic to a hyperbolic medium or viceversa (Fig. 2.3(c)).

2.2.2 Implementations

We now ask ourselves the question whether a natural material exists which possesses direction-dependent permittivities with opposing sign. Permittivity represents the mascroscopic response of a system of charged particles to an externally applied electric field. A positive permittivity implies a polarization parallel to the field, and characterizes insulators. A negative permittivity, indicating an antiparallel polarization, is observed at infrared frequencies in dielectrics and semiconductors, in bands comprised between transverse and longitudinal phonons ("Reststrahlen band") [37], and in systems described as free electron gases below the plasma frequency [38].

A difference in frequency between phononic modes parallel and perpendicular to the optical axis causes triglycine sulphate and sapphire to exhibit hyperbolic dispersion respectively in the low-terahertz ($250 < \lambda_0 < 268\,\mu$m) and mid-infrared (around $20\,\mu$m)

range, while bismuth owes its 10-μm anisotropy window in the far-infrared ($53.7 < \lambda_0 < 63.2\,\mu m$) to direction-dependent effective masses [39]. Highly oriented pyrolitic graphite displays hyperbolic behavior in the ultraviolet, allowed by the free motion of electrons along parallel atomic layers, but its performance is limited by absorption losses [40]. Therefore, the available alternatives do not grant access to the visible range, and are too scarce to constitute a solid and versatile tool for applications.

In order to design a hyperbolic medium and customize its properties, one needs to artificially induce a negative permittivity in one or two spatial dimensions. The first attempt in this direction dates back to the late 1960s, when permittivity engineering was proposed by restricting to 1D the motion of a magnetized electron plasma by means of a constant magnetic field [41]. This approach, unpractical in terms of device portability and again limited in frequency, was overcome in the past decade thanks to progresses in nanofabrication, which allowed the confinement in less than three dimensions of the free electrons of metals. Currently, two structures have been shown to generate the desired kind of anisotropy: a stack of deep subwavelength alternating metallic and dielectric layers, termed *multilayer*, and a lattice of metallic nanowires embedded in a dielectric matrix, termed *nanowire array* (Fig. 2.4). The optical response of these discontinuous media can be homogenized via an effective medium theory (EMT), resulting in a hyperbolic effective permittivity tensor. The ML and the NW array constitute within such approximation *hyperbolic metamaterials*[1]. The physical mechanism that originates in the real implementations the properties discussed in Subsection 2.2.1 is the coupling of surface plasmons (in the ML case) or localized surface plasmons (in the NW case) of individual metallic/dielectric interfaces [4, 5]; we will delve deeper in this aspect in the following section.

The effective parameters in the limit of infinitesimal layer thickness for a ML

[1] Photonic crystals exhibit a periodicity analogous to that of MLs and NW arrays, but are not metamaterials as they cannot be represented by effective bulk parameters.

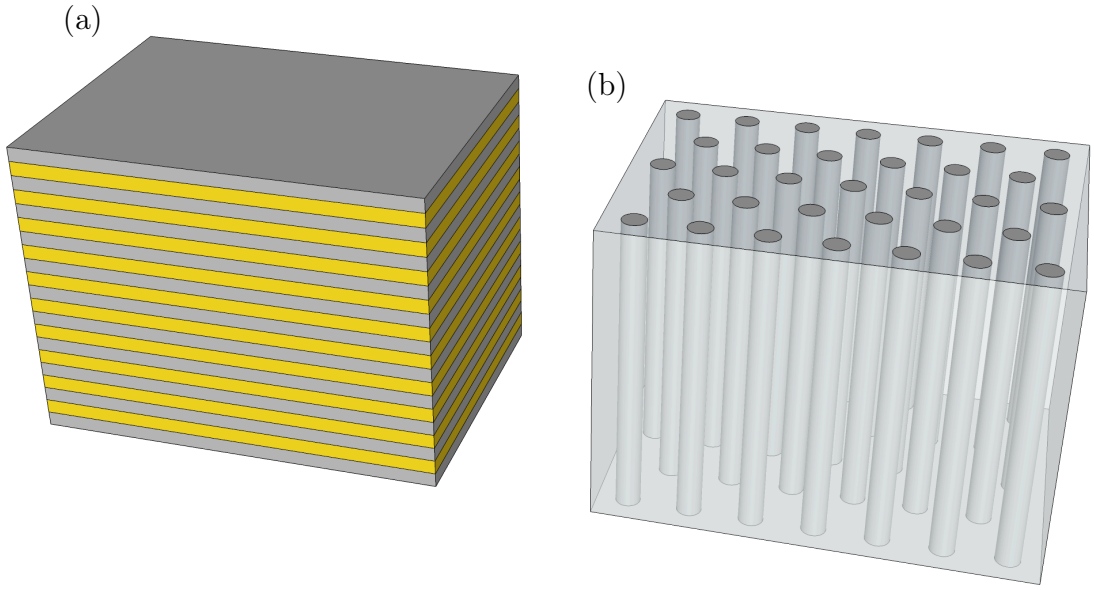

Figure 2.4: Schematics of (a) a multilayer and (b) a nanowire hyperbolic metamaterial.

parallel to the *xy* plane, originally derived by Rytov [42] and later reobtained with the characteristic matrix formalism by Wood *et al.* [33], are:

$$\varepsilon_{xx} = \varepsilon_{yy} = p\varepsilon_m + (1-p)\varepsilon_d \tag{2.16}$$

$$\varepsilon_{zz} = \left(\frac{p}{\varepsilon_m} + \frac{1-p}{\varepsilon_d} \right)^{-1}, \tag{2.17}$$

where the *filling ratio* $p = t_m/(t_m + t_d)$ is the volume percentage of metal in a unit cell or *period*, constituted of a dielectric layer and a metallic layer with thicknesses t_d and t_m and permittivities ε_d and ε_m. In general, ε_d and ε_m are complex quantities exhibiting temporal dispersion (i.e. they depend on the angular frequency ω), and so are ε_{xx} and ε_{zz}. As we chose the '+' sign in the plane wave time-dependence $e^{i\omega t}$ (Subsection 2.2.1), our sign convention for permittivity will be $\varepsilon = \varepsilon' - \varepsilon''$. The real part ε', < 0 for ε_m and > 0 for ε_d, accounts for polarization response, while the imaginary part ε'', > 0 for

both ε_d and ε_m, models the dissipative (or "Ohmic") losses in the material. The real and imaginary parts of the effective parameters of a Ag/SiO_2 ML are plotted in Fig. 2.5 for two different filling ratios. As p and ω are varied, the medium described by Eqs. (2.16) and (2.17) can exhibit Type I or Type II hyperbolic character, but also behave as an effective dielectric ($\varepsilon_{xx}, \varepsilon_{zz} > 0$) or an effective metal ($\varepsilon_{xx}, \varepsilon_{zz} < 0$), as summarized in the optical phase diagrams of Fig. 2.6 [32, 43]. A proper selection of parameters allows access to the epsilon-near-zero (ENZ) regime [44].

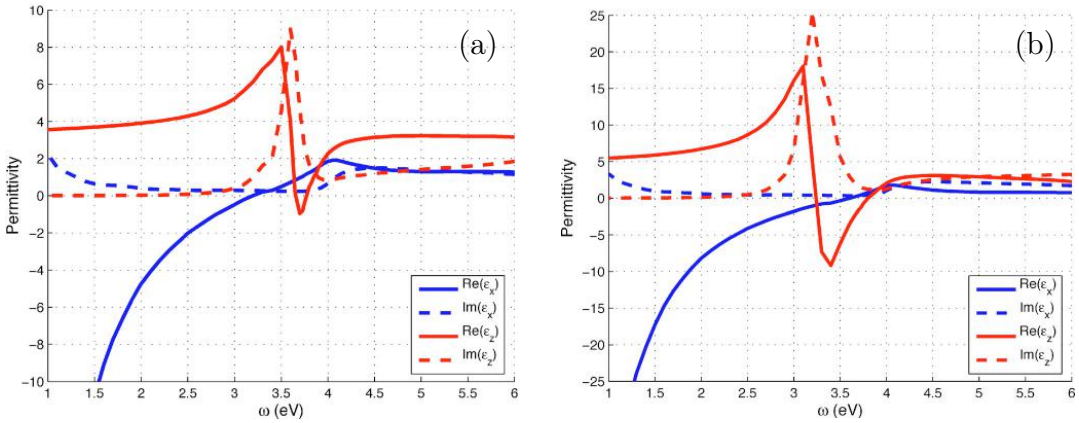

Figure 2.5: (a) Real and imaginary parts of the in-plane ε_x and perpendicular ε_z permittivity components for a Ag/SiO_2 multilayer with filling ratio $p = 0.4$ and (b) $p = 0.6$. Reproduced from Ref. [33].

ML HMMs are fabricated by electron-beam or sputter deposition in vacuum of both the metallic and non-metallic constituents. Fig. 2.7 shows a most recently demonstrated ML HMM of superior quality, fabricated with sputtering technology. The choice of materials depends on the target spectral range, on losses and on the impedance match. The latter requires that the absolute values of ε'_d and ε'_mdo not differ by more than an order of magnitude, in which case radiation coming from the dielectric side is reflected instead of propagating. The plasma frequencies of Ag and Au fall in the ultraviolet, at 9.2 and 8.9 eV [38]. Below those values, the real part of permittivity of such plasmonic metals becomes negative, and increases in magnitude as frequency

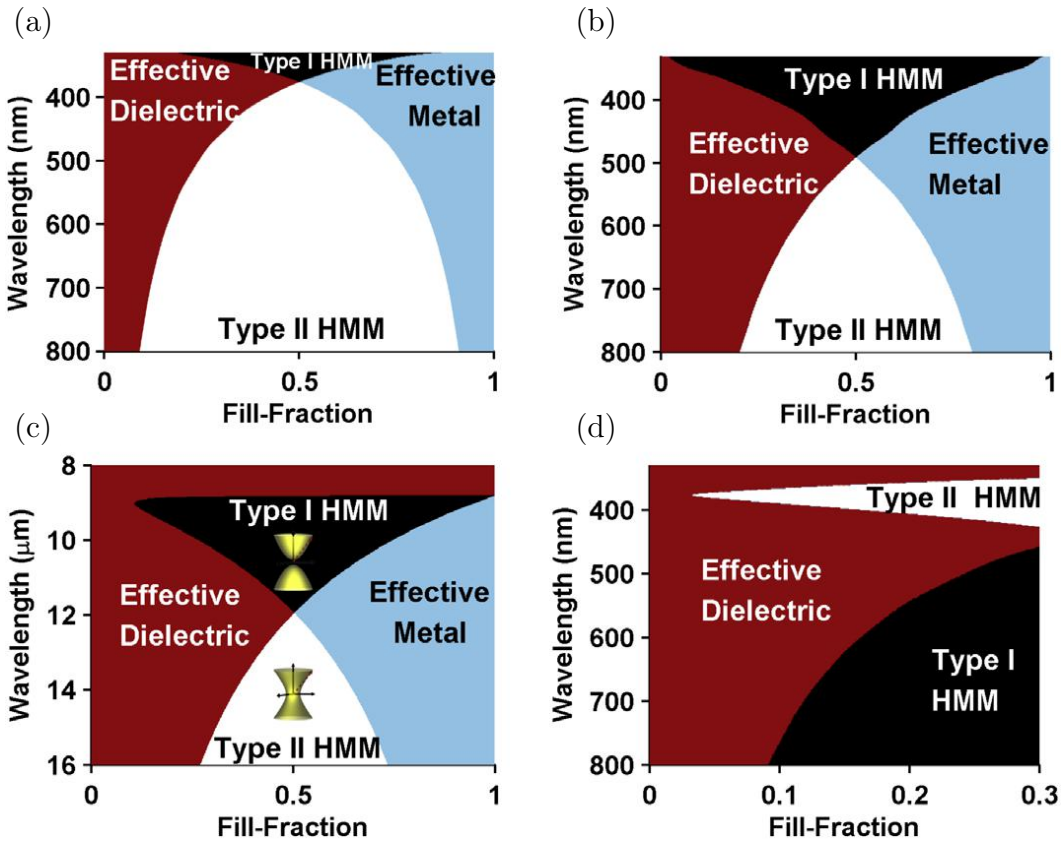

Figure 2.6: Optical phase diagrams for (a) a Ag/Al_2O_3 multilayer system, (b) a Ag/TiO_2 multilayer system, (c) an AlInAs/InGaAs multilayer system and (d) Ag nanowires in an Al_2O_3 matrix. Reproduced from Ref. [32].

progressively decreases. Throughout the ultraviolet and visible regions, on one hand losses are limited, and on the other hand the relatively small ε'_m can be impedance-matched with the ε'_d of poorly absorbing dielectrics such as Al_2O_3 and TiO_2. When moving to the infrared, the real part of permittivity in metals becomes so negative that it causes an impedance mismatch with any other media. Therefore, Ag and Au need to be replaced with semiconductors, whose plasma frequency falls in the infrared and can be controlled by doping. Accordingly, intrinsic semiconductors play the role of dielectrics [45].

Alternative plasmonic materials for optical applications have been proposed to operate in the near-infrared and mid-infrared range [38, 46], while graphene was predicted

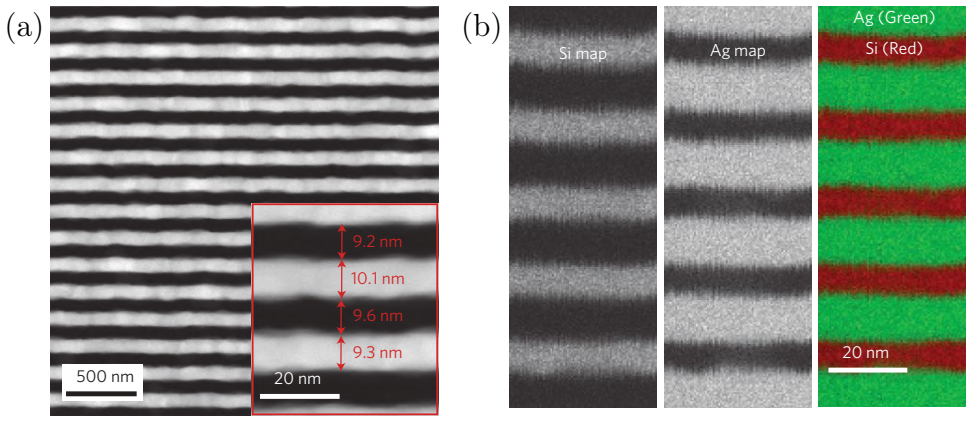

Figure 2.7: (a) Dark-field STEM images of the cross-sections of Ag/Si multilayers, deposited by DC magnetron sputtering, showing well-formed periodic lattice structures (filling ratio $\rho = 0.5$, period 20 nm). The white color corresponds to Ag, the black one to Si. (b) Element mapping for the constituent materials (Si and Ag), verifying the established multilayer lattice with some minor diffusion of Ag into Si. Reproduced from Ref. [18].

to induce a tunable hyperbolic response at THz frequencies [47, 48, 49, 50, 51]; SiC/SiO_2 layered media, which derive their anisotropy from phononic resonances [52], are currently being investigated for thermal engineering of the near field [53, 54]. Table 2.1 collects the experimentally demonstrated material combinations that lead to MLs with hyperbolic properties.

We observe that Eqs. (2.16) and (2.17) only depend on the filling ratio p, disregarding the period. This is because such approximations are obtained in the limit of vanishing thicknesses of the constituent layers. Strictly speaking that situation should be treated in a different way, since quantum size effects induce in metals a spatial dispersion, in addition to the ordinary temporal dispersion (so that ε_m becomes a function not only of the frequency ω, but also of the wavevector $\mathbf{k}$), which alters their hyperbolic character [66, 67, 68, 69, 70, 71, 72, 73]. We shall analyze the implications of extremely reduced sizes in Subsection 2.4.1. As a rule of thumb, in metal layers thicker than 5 nm spatial dispersion can be neglected. A practical criterion for Eqs. (2.16) and (2.17) to be

Table 2.1: Material combinations for the fabrication of multilayer hyperbolic metamaterials.

Range	Materials	Period [nm]	p	N. of periods	Reference
UV	Ag/Al_2O_3	70	0.5	8	[9]
Visible	Au/Al_2O_3	38	0.5	8	[55, 56, 57]
	Au/Al_2O_3	40	0.5	8	[58]
	Au/Al_2O_3	43	0.35	10	[59]
	Au/TiO_2	48	0.33	4	[60]
	$Ag/PMMA$	55	0.45	10	[61]
	Ag/LiF	75	0.4	8	[61]
	Ag/MgF_2	50	0.4	8	[61]
	Ag/MgF_2	60	0.42	7	[62]
	Ag/TiO_2	31	0.29	5	[43]
	Ag/Ti_3O_5	60	0.5	9	[63]
	Ag/SiO_2	30	0.5	3	[31]
	Ag/Si	20	0.5	15	[18]
IR	$AlInAs/InGaAs$	160	0.5	50	[45]
	$Al:ZnO/ZnO$	120	0.5	16	[64]
	Ag/Ge	50	0.4	3	[65]

applicable is that the ML period must be much smaller than the wavelength of operation (thereby preventing radiation from perceiving optical discontinuities); a more accurate description, that includes the dependence on layer thickness in a second order term, was adopted in [56]. In real media, fabrication poses a limit to the number of periods that can be stacked while preserving an actual ML structure; a total of eight layers was estimated

to be the threshold to observe the predictions of the EMT [32], although as little as six layers were shown to achieve an effective hyperbolic behavior [65, 31].

To determine EMT parameters for NW media is not as straightforward as for MLs, since the homogenization adopted strongly depends on the frequency range of interest. Spatial dispersion cannot be neglected [74, 75, 76] and leads to non-hyperbolic isofrequency contours, except in the optical region, where it is reduced by the kinetic inductance and by the losses of the metallic constituent [77, 78]. With a z axis orientation parallel to the wires, the effective permittivity tensor takes the form [79, 35, 80, 81]:

$$\varepsilon_{xx} = \varepsilon_{yy} = \frac{[(1+p)\,\varepsilon_m + (1-p)\,\varepsilon_d]\,\varepsilon_d}{(1-p)\,\varepsilon_m + (1+p)\,\varepsilon_d} \tag{2.18}$$

$$\varepsilon_{zz} = p\varepsilon_m + (1-p)\varepsilon_d, \tag{2.19}$$

where this time p is the percentual area occupied by NWs in an xy section of the medium. As for ML HMMs, the response of NW media can be tuned to different regimes by varying ω and p (Fig. 2.6(d)); an example of effective parameters for two typical filling ratios is shown in Fig. 2.8.

Due to the extremely high aspect ratio, most of the practical NW HMMs are fabricated by electrochemical deposition of Ag or Au inside a self-assembled porous alumina (Al_2O_3) template [82, 83, 84, 79, 36]. The geometrical features of such matrix, prepared by electrochemical anodization of Al, can be finely tailored via multiple fabrication parameters or through extra steps (such as focussed-ion-beam (FIB) pre-patterning), ensuring the formation of ordered and extremely dense pores (Fig. 2.9). Table 2.2 reports the characteristic sizes of Al_2O_3 templates, together with other possible material choices for the host matrix. Arrays of carbon nanotubes in the metallic state have been proposed

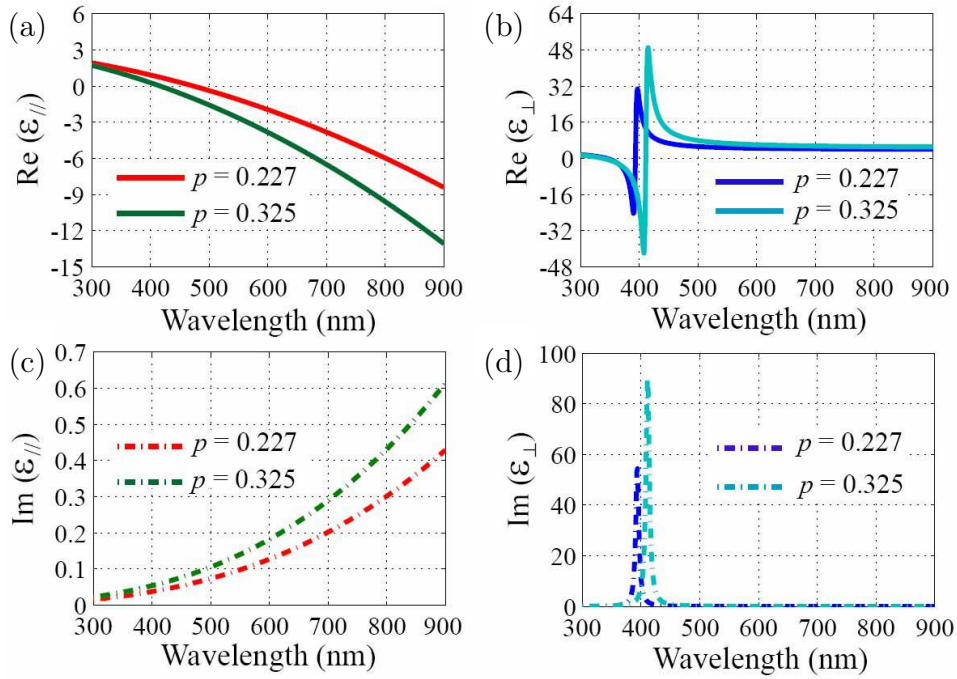

Figure 2.8: Effective permittivities for Ag nanowires embedded in an Al_2O_3 matrix with two different filling ratios p. (a) and (b) plot the real part of the permittivity parallel and perpendicular to the nanowire, respectively. (c) and (d) are the corresponding imaginary parts. Reproduced from Ref. [35].

as an alternative to the template-NW scheme, thanks to their capability to quench spatial dispersion and the high degree of control of their growth [85].

The chemical processes and the self-organizational mechanisms through which porous templates are manufactured confer on NW HMMs an advantage over their ML counterparts, in terms of ease and cost of fabrication. Besides their potential application in imaging as negatively refracting materials [35, 36, 86] and in spontaneous emission engineering [87], these media have been demonstrated to be superior biosensors [88]. A guided mode can be excited under resonant conditions in an assembly of Au nanorods, either embedded in an Al_2O_3 template or free-standing, in contact with the liquid to analyze. In analogy to conventional SP-based devices, an increase in the refractive index causes a redshift of the resonance, but with a sensitivity two order of magnitude

higher (32,000 nm per RIU). In addition, the probe depth is large (500 nm), and the discontinuous porous nanotexture of the nanorod matrix allows degrees of freedom in experiment design unaccessible with uniform plasmonic films.

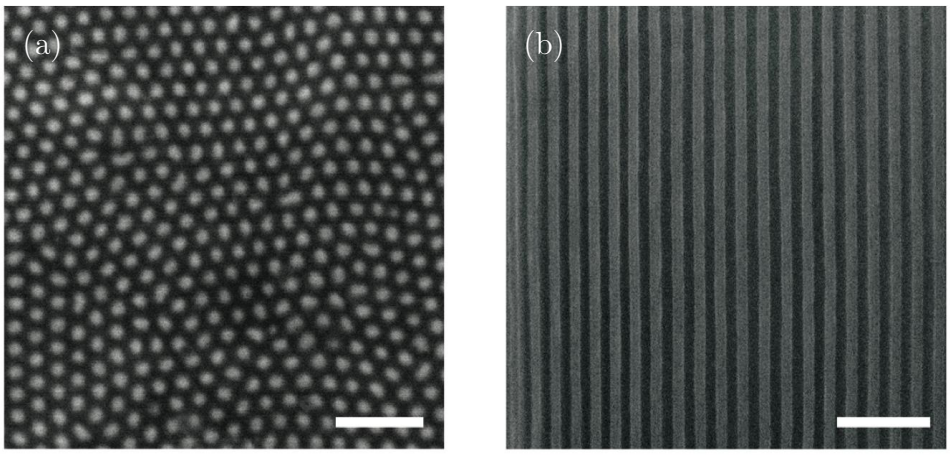

Figure 2.9: SEM images of the earliest experimentally demonstrated nanowire hyperbolic metamaterial, consisting of Ag nanowires electrochemically plated in an anodic aluminum oxide (AAO) template. (a) Top view and (b) cross section of the nanowires (light gray regions), with a diameter of 60 nm and a center-to-center distance of 110 nm. Scale bars: 500 nm. Reproduced from Ref. [36].

Table 2.2: Main parameters of nanoporous matrices made of Al_2O_3, $A^{III}B^{V}$ semiconductor compounds and porous-Si by electrochemical etching. Reproduced from Ref. [78].

Material	Pore diameter	Pore wall thickness	Thickness of matrices
Al_2O_3	20–70 nm	15–30 nm	>2 μm
$A^{III}B^{V}$	20–500 nm	10–100 nm	>150 μm
Si	10 nm–several μm	10 nm–several μm	>400 μm

2.3 Applications

2.3.1 High-resolution imaging and lithography

Light emitted or scattered off an object can be can be thought of as a Fourier superposition of plane waves. Low k-vector components of the spatial spectrum encode large geometric features, while high k-vectors describe finer details. In an isotropic medium, characterized by bounded isofrequency contours, momenta larger in magnitude than k_0 correspond to evanescent waves: therefore, they are forbidden from propagating into the far-field, which results in loss of information. This phenomenon, known as diffraction limit, causes resolution in conventional imaging devices to be limited to distances $R > (0.61\lambda)/NA$ (Rayleigh criterion), where NA is the numerical aperture of the imaging system [24].

The technological challenge for high-resolution microscopy is to recover in the far-field the evanescent components of the spectrum [89]. Different approaches have been proposed based on near-field optical scanning [90], fluorescent imaging [91] or stochastic optical reconstruction imaging [92], with the common disadvantage of low throughput and speed. An extremely thin Ag slab can act as a superlens, which enhances evanescent waves via resonant excitation of surface plasmons [93, 94, 95]. The non-propagating nature of these components stays inaltered while they are transmitted through the metallic medium, so that a coupling element is ultimately required to scatter them into the far-field.

HMMs offer a completely new paradigm to tackle the problem [96]. Their unique anisotropic dispersion naturally supports high k-vector components without relying on resonant mechanisms (intrinsically limited in frequency, and detrimental to image formation due to absorption losses), and makes them ideal candidates not only to read but also to write nanoscale information.

Fundamental phenomena such as negative refraction [97, 98, 99, 36, 100] and

partial focusing of radiation [101, 102, 103, 31] make clear the impact of HMMs on the field of imaging. The experimental efforts to shape hyperbolic media into imaging devices resulted in the invention of the hyperlens, that we discuss together with its numerous developments and implications in the following two subsubsections.

Hyperlens

Any plane wave illuminating an object can be written as an expansion of cylindrical waves,

$$exp(ikx) = \sum_{m=-\infty}^{\infty} i^m J_m(kr) exp(im\phi), \tag{2.20}$$

where i is the imaginary unit, k is the magnitude of the wavevector, $J_m(kr)$ denotes the Bessel function of the first kind, m is the angular momentum mode number of the cylindrical wave and r, ϕ are cylindrical coordinates (distance from the origin and azimuthal angle) [104]. In an ordinary isotropic medium, the radial component of the electric field decays exponentially at the origin as m becomes higher (Fig. 2.10(a)). The conservation of angular momentum, $m = k_\theta r$, implies indeed that a progressively smaller distance r from the center corresponds to a larger tangential wavevector component k_θ. In order for the isotropic dispersion relation

$$k_r^2 + k_\theta^2 = \varepsilon \frac{\omega^2}{c^2} \tag{2.21}$$

to be satisfied, the arbitrary growth of k_θ necessarily results in an imaginary radial component k_r, and therefore in a mode evanescent near the origin. On the other hand, in a hyperbolic medium with strong *cylindrical anisotropy* – radial permittivity $\varepsilon_r < 0$,

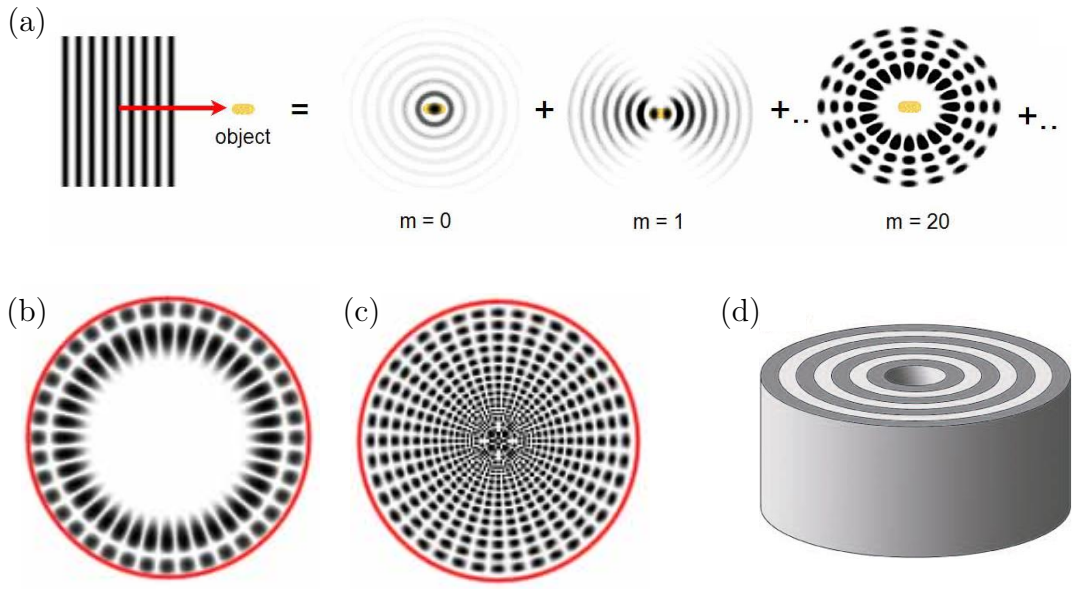

Figure 2.10: (a) Cylindrical wave expansion of a plane wave scattered by a target (yellow object). The regions of high electric field intensity are shown in black, those of low intensity in white. (b) High angular momentum state in an isotropic dielectric cylinder and (c) in a cylinder made of an effective hyperbolic medium with $\varepsilon_r < 0$ and $\varepsilon_\theta > 0$. (d) Possible realization of a hyperlens, consisting in alternating concentric metallo/dielectric layers. Reproduced from Ref. [104].

tangential permittivity $\varepsilon_\theta > 0$ – k_r and k_θ are connected by

$$\frac{k_r^2}{\varepsilon_\theta} - \frac{k_\theta^2}{|\varepsilon_r|} = \frac{\omega^2}{c^2}. \tag{2.22}$$

This dispersion is unbounded, so that now as k_θ increases toward the center, k_r also increases, staying real for any value of r and m. As a consequence, high-m modes are allowed to reach the origin, and access small object features. The comparison between the field distribution in an isotropic medium (Fig. 2.10(b)) and in a metamaterial with cylindrical hyperbolic anisotropy (Fig. 2.10(c)) shows that in the second case not only the mode penetrates toward the center, but also that the distance between the field nodes at the core gradually decreases, enabling sub-wavelength probing of spatial details.

A practical configuration that exploits the cylindrical dispersion (2.22) is obtained by bending a flat multilayer into a hollow core cylinder like the one in Fig. 2.10(d). This device can act as a hyperlens, in that it turns sub-wavelength objects inscribed on its inner walls with radius R_{in} into magnified images on the outer surface with radius R_{out}. Such behavior is made possible by two simultaneous mechanisms. The first is the propagation of high k-vector waves, which the hyperbolic environment prevents from becoming evanescent. The second is the compression of the tangent wavevector component k_θ as the waves travel along the radial direction, dictated by the angular momentum conservation ($k_\theta \sim 1/r$). This near-to-far field conversion of information from the internal to the external boundary of the cylinder results in a magnification factor simply given by the ratio R_{out}/R_{in} [104, 105].

The first experimental implementation of a hyperlens was optimized for ultraviolet frequencies [9, 106]. It consisted of a curved stack of 16 alternating Ag and Al_2O_3 layers, each 35 nm thick, deposited by electron-beam evaporation on a half-cylindrical quartz mold (Fig. 2.11). Sub-diffraction limited objects were inscribed into a 50-nm-thick Cr layer located at the inner surface, and - upon illumination at the wavelength $\lambda_0 =$

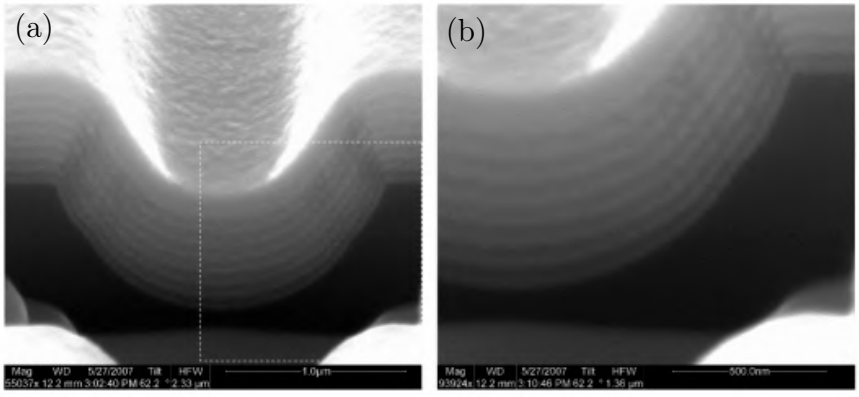

Figure 2.11: (a) SEM image of the cross section of the cylindrical hyperlens. Bright and dark layers correspond to Ag and Al_2O_3 respectively, while the topmost thick and bright layer is Cr. (b) Zoomed detail of the white dashed square in (a). Reproduced from Ref. [106].

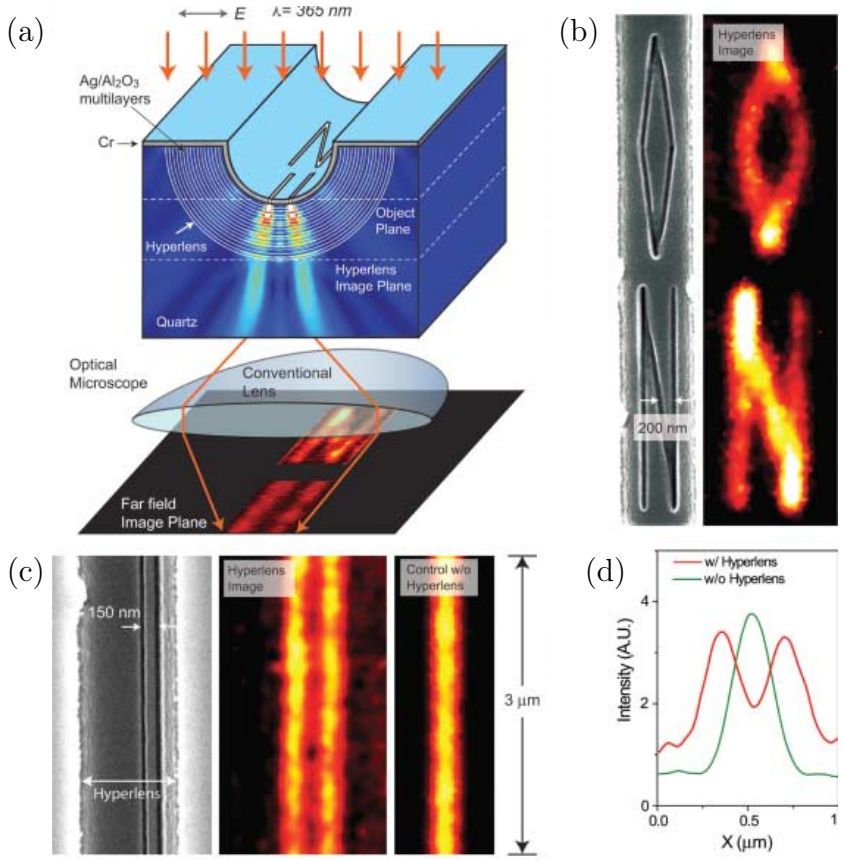

Figure 2.12: (a) Schematic of the cylindrical hyperlens with a numerical simulation showing imaging of sub-diffraction limited objects. (b) Arbitrary object (the word "ON") imaged with sub-diffraction resolution. The width of the lines composing the object is about 40 nm. (c) Left to right: SEM top view of a 150-nm-spaced line pair object fabricated near the inner surface of the hyperlens, magnified image obtained with the hyperlens that clearly resolves the object and diffraction-limited image from a control experiment without the hyperlens. (d) Averaged cross-section of the object in (c), imaged with (red curve) and without (green curve) the hyperlens. Reproduced from Ref. [9].

365 nm - magnified at the outer boundary of the hyperlens, where they were detected via a conventional imaging system with $\lambda_0/1.4$ (corresponding to 260 nm) resolution (Figs. 2.12(a) and 2.12(b)). A control experiment showed that in the absence of the hyperlens the same objects could not be resolved by the same apparatus (Figs. 2.12(c) and 2.12(d)). The device was able to image features as closely spaced as 125 nm, therefore achieving a $\lambda_0/2.92$ resolution [106].

This cylindrical prototype of hyperlens is impractical for imaging applications since its magnification is limited to one dimension. The use of a spherical geometry in combination with a different material choice allowed 2D resolution improvement in the visible range [63]. The spherical hyperlens was fabricated by conformal deposition of 18 alternating layers of Ag and Ti_3O_5, all of equal thickness 30 nm, onto a hemi-spherical quartz mold (Fig. 2.13). A high-index dielectric material such as Ti_3O_5 matches the larger magnitude of permittivity of Ag in the visible, as compared to the ultraviolet, moving accordingly the operational wavelength to that region [107]. Objects with different shapes and configurations were inscribed in the inner side of the hyperlens and illuminated at

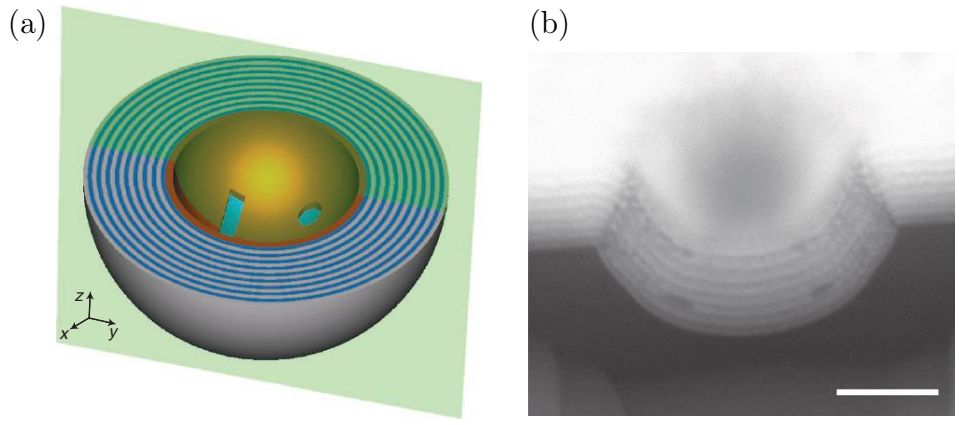

Figure 2.13: (a) Schematic of the spherical hyperlens: 9 Ag (30 nm)/Ti_3O_5 (30 nm) periods, and a 50-nm Cr layer with two inscribed sample objects. (b) SEM image of the cross section of the spherical hyperlens. Scale bar 500 nm. Reproduced from Ref. [63].

$\lambda_0 = 410\,\text{nm}$. Two apertures separated by 160 nm generated images with a 333 nm spacing, corresponding to an averaged magnification ratio of 2.08 (Fig. 2.14). The performance of the spherical hyperlens is limited by defects in fabrication, resulting in loss of concentricity of the layers and in a position-dependent magnification, and by the curved outer surface of the device, which causes distortion in the subsequent far-field image.

Besides the disadvantage just discussed, a curved geometry, based on which the first hyperlens predictions were formulated [104, 108, 109], is hard to implement in biological applications. As an alternative, planar configurations were proposed that replaced both the inner and the outer (Fig. 2.15(a)) of just the outer (Figs. 2.15(b) and 2.15(c)) curved surface with parallel planes by redesigning the layer shape, or more generally the space properties, via transformation optics [110, 111, 112, 113]. A hybrid-superlens hyperlens, where an object on a flat input surface is imaged at a curved output boundary, was recently investigated (Fig. 2.15(d)) [114]. An inherent limitation of strongly anisotropic media is the huge impedance mismatch at the interface with low-index dielectrics. To mitigate the in-coupling and out-coupling reflection losses of the

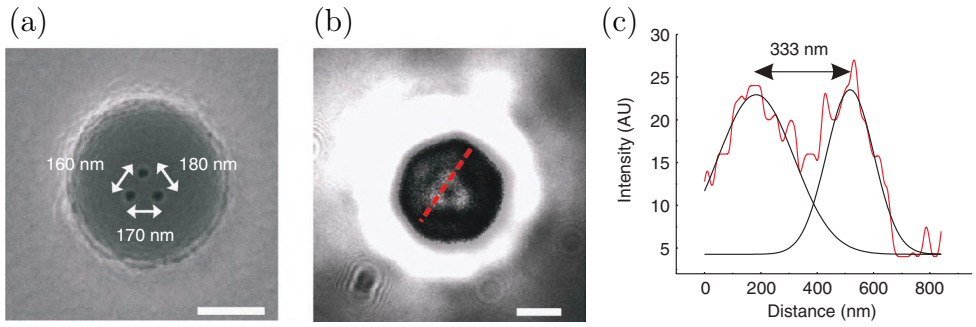

Figure 2.14: (a) SEM image of three dots positioned triangularly with gaps of 180, 170 and 160 nm on the inner side of the spherical hyperlens. (b) Image and (c) cross section along the red dashed line of the object after being magnified. The black curved, corresponding to a cross-sectional analysis, Scale bar in (a) and (b) is 500 nm. Reproduced from Ref. [63].

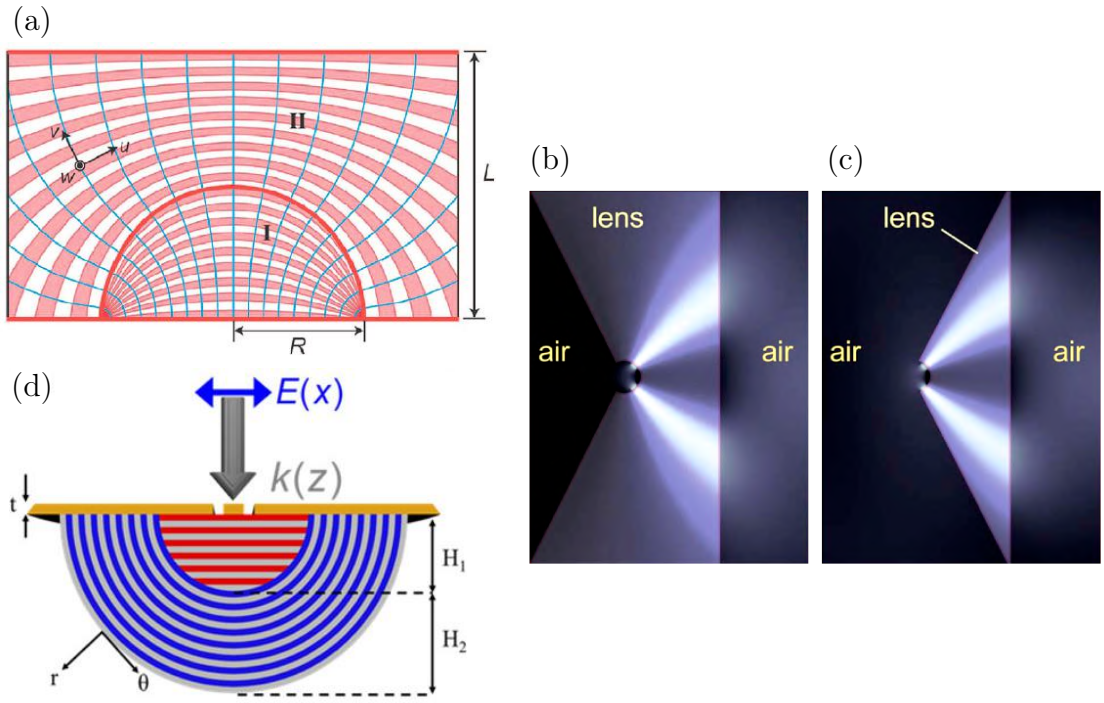

Figure 2.15: (a) Schematic of an optical transformer consisting of two domains of alternating curved layers of metal (pink) and semiconductor (white). The light flows along the v axis (curved blue lines), and the interfaces between the layers comply with the u axis. (b) Magnetic field map inside a 3/4-body and (c) a 1/4-body hyperlens with flat output surface. (d) Schematic of the hybrid-superlens hyperlens. (a) Reproduced from Ref. [110], (b) and (c) from Ref. [111], (d) from Ref. [114].

hyperlens one can customize $\overline{\overline{\mu}}$ and $\overline{\overline{\varepsilon}}$ through transformation optics: a radius-dependent permeability allows simultaneous match at both interfaces, while a nonmagnetic medium can only act either on the inner or on the outer boundary (Figs. 2.16(a) and 2.16(b)) [115]. A complementary approach to suppress scattering consists in immersing the hyperlens into high-index liquids (Figs. 2.16(c) and 2.16(d)) [107]. In order for a device to behave as a conventional lens, it should be capable to focus plane waves. This is forbidden to hyperlenses, since they lack a phase compensation mechanism [105]. Metalenses realizing the Fourier transform function were designed by providing with such mechanism a slab of hyperbolic medium [116, 117, 118].

Absorption losses due to the metallic constituent are ineliminable, but can be

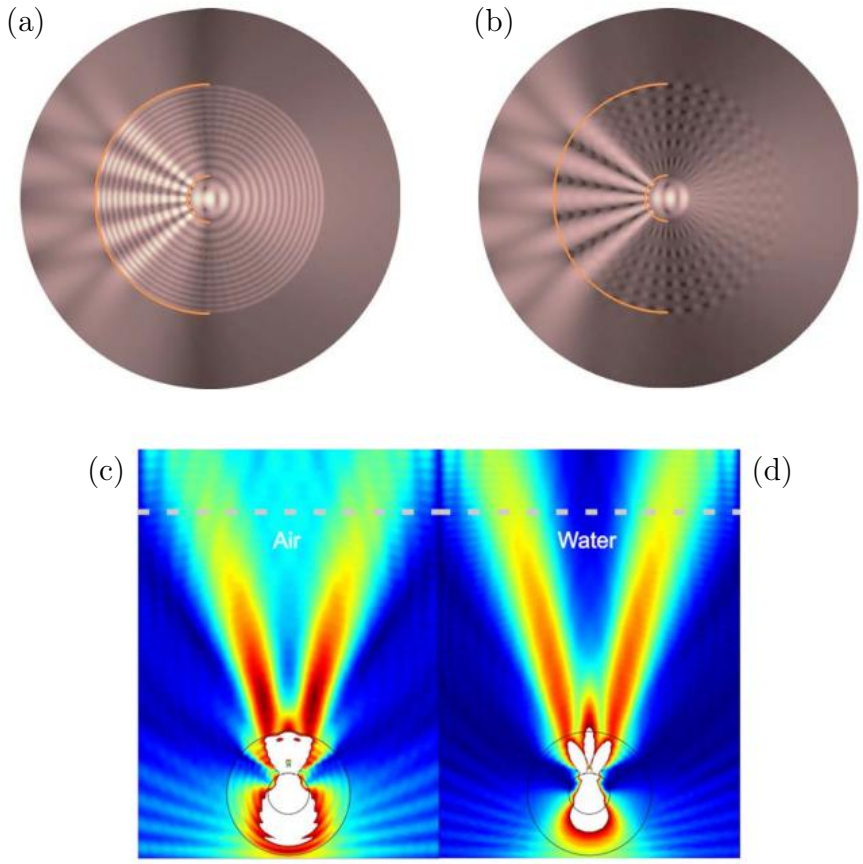

Figure 2.16: (a) Magnitude of the H-field for a cylindrical hyperlens designed to be impedance-matched at the internal and (b) at the external interface. (c) Normalized H-field distribution in a cylindrical hyperlens immersed in air and (d) water. (a) and (b) Reproduced from Ref. [115], (c) and (d) from Ref. [107].

circumscribed by increasing the percentage of dielectric or shifting the operating range to longer wavelengths [107]. A major source of nonideality in the experimentally demonstrated hyperlenses are fabrication imperfections, that can either be incorporated in theoretical models [119] or reduced at the manufacture stage with rolled-up technology [120, 121, 122, 123].

Recent works studied a nonlinear hyperlens [124], a tunable hyperlens [51], and a hyperbolic metamaterial lens with hydrodynamical nonlocal response [72]. In the first, dielectric layers with high Kerr-type nonlinearity were introduced to minimize diffraction

inside a hyperlens, allowing longer propagation distances and broadband operation in the ultraviolet. In the second, the metallic layers of a cylindrical hyperlens were replaced with single sheets of graphene [50, 125]. The plasmonic response of this material can be dynamically manipulated in the THz region by controlling the chemical potential with an external bias voltage [126]: at a fixed frequency, the effective permittivities of a curved ML were tuned until they entered the desired hyperbolic regime. In the last study, the focussing properties of a slab of ML HMM were shown to depend on the metal permittivity model - nonlocal versus local - adopted: such system was therefore indicated as a potential candidate to test the validity of the hydrodynamic nonlocal theory.

The ability of detecting and manipulating sub-wavelength information is not a prerogative of ML implementations, but is also attainable with a NW geometry [78]. Wires can transport over a few wavelengths low k-vector information thanks to plasmonic resonances, a phenomenon known as canalization [127]. This corresponds to a superlensing behavior, which includes magnification if the wire arrangement is made divergent ("tapered configuration") instead of parallel [128], and is effective at THz or lower frequencies [129, 130, 131]. The hyperbolic properties of NW HMMs, that emerge in the infrared and visible range, enable negative refraction [36], and therefore image focussing inside and outside a slab of such media [35, 86]. Transport at telecom wavelengths (1510 - 1580 nm) of features as small as $\lambda_0/4$ over a distance $> 6\lambda_0$ was demonstrated in a Au/Al_2O_3 NW HMM [132]. The quasi-TEM collective mode that guided the image was mostly localized in the dielectric matrix (pore diameter 12 nm, pore-to-pore average spacing 25 nm), which minimized the absorption losses. In addition, bottom-up grown templates allow the imaging of large areas, as compared with those available to hyperlenses. However, the lack of a magnification mechanism required a near-field scanning optical microscope (NSOM) to detect the transmitted image (Fig. 2.17), which impedes the integration of this technology in far-field devices. To the best of our knowledge,

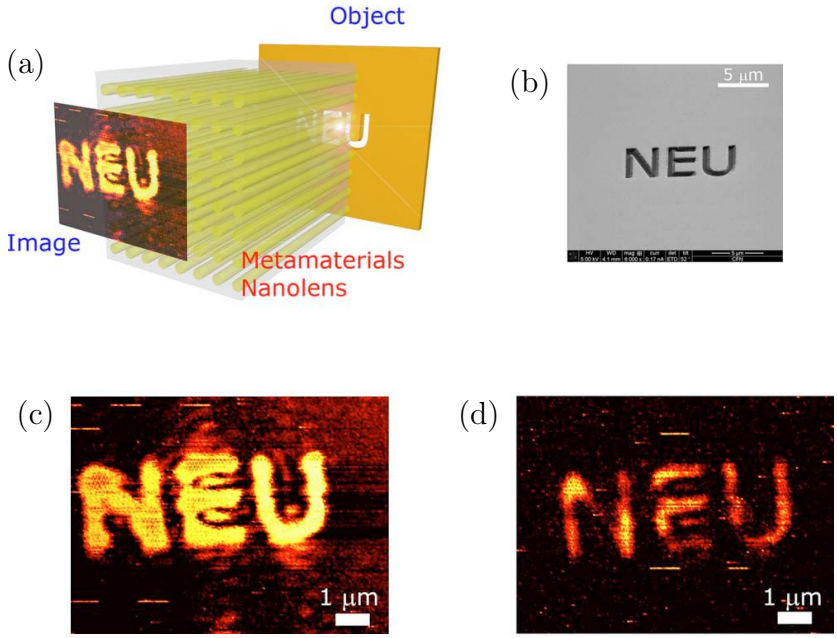

Figure 2.17: (a) Schematic of sub-wavelength image transport with a NW HMM at $\lambda_0 = 1550$ nm. (b) SEM image of the "NEU" letters milled in 100-nm-thick Au film. The letters have 600-nm-wide arms (0.4 λ_0). (c) NSOM scan of the source object in the near-field (d) NSOM scan of the corresponding image by the NW HMM at the output surface. Reproduced from Ref. [132].

the performance of the ML-based hyperlens - diffraction-limited image transport and retrieval in the far field, entirely ascribable to bulk hyperbolic properties - has not been equaled with NW HMMs at optical frequencies.

Nanolithography

The diffraction limit poses a constraint not only on object details detectable with far-field equipment, but also on the resolution of patterns written by photolithography. In order to define sub-wavelength features, such a cost-effective and high-throughput technique is replaced by alternative forms of lithography, based for instance on electron-beam, focussed-ion-beam or imprint, that involve expensive machines and/or cleanroom processing.

A different solution consists in utilizing HMMs to miniaturize far-field information. This approach still relies on conventional photo-lithographic procedures, but wave propagation through an anisotropic space enables ratios between the transferred image and the object smaller than 1:1. A Ag/SiO_2 ML slab was proposed to generate sub-diffraction-limited patterns from traditional 1D or 2D diffraction-limited masks. [133]. TM-polarized light at the wavelength of $\lambda_0 = 405$ nm was shone on a 1D mask with period $\Lambda = 400$ nm (Fig. 2.18(a)). The ML supported exclusively the propagation of those waves with tangential wavevector larger than nk_0 (n: refractive index of the medium on the transmission side of the grating); furthermore, its spatial frequency pass band could be tuned with design parameters to allow only one diffraction order ($\pm m$-th order) from the mask. The superposition of diffracted waves of the selected $\pm m$-th order formed on the other side of the slab a sub-diffraction-limited pattern with period $\Lambda/2m$. Specifically, the choice $m = 3$ resulted in a 6-fold miniaturization of the mask profile.

The hyperlens also exhibits writing capabilities, exploitable by simply reversing its direction of operation: a diffraction-limited pattern defined on the outer surface of radius R_{out} can be reduced to a sub-diffraction-limited one on the inner side of radius R_{in} by virtue of tangential wave vector de-compression, with a de-magnification given by the ratio R_{in}/R_{out} [11]. Finite element simulations (Fig. 2.18(b)) showed that a Ag/Al_2O_3 cylindrical hyperlens operating at $\lambda_0 = 375$ nm transforms a 1D mask of openings with period 280 nm and width 140 nm in a pattern with period 40 nm. This corresponds to a reduction factor of $1/7$, which matches the radii ratio 120 nm/840 nm. To obtain flat input and output planes, the hyperlens can be polished as in Fig. 2.18(c). The linear reduction achieved is $x_i/x_o = (R+D)/R$, where R is the radius of the inner surface of the original hyperlens, and D is the thickness of the flat hyperlens.

Currently, none of the alternative lithography schemes discussed has seen experimental implementation.

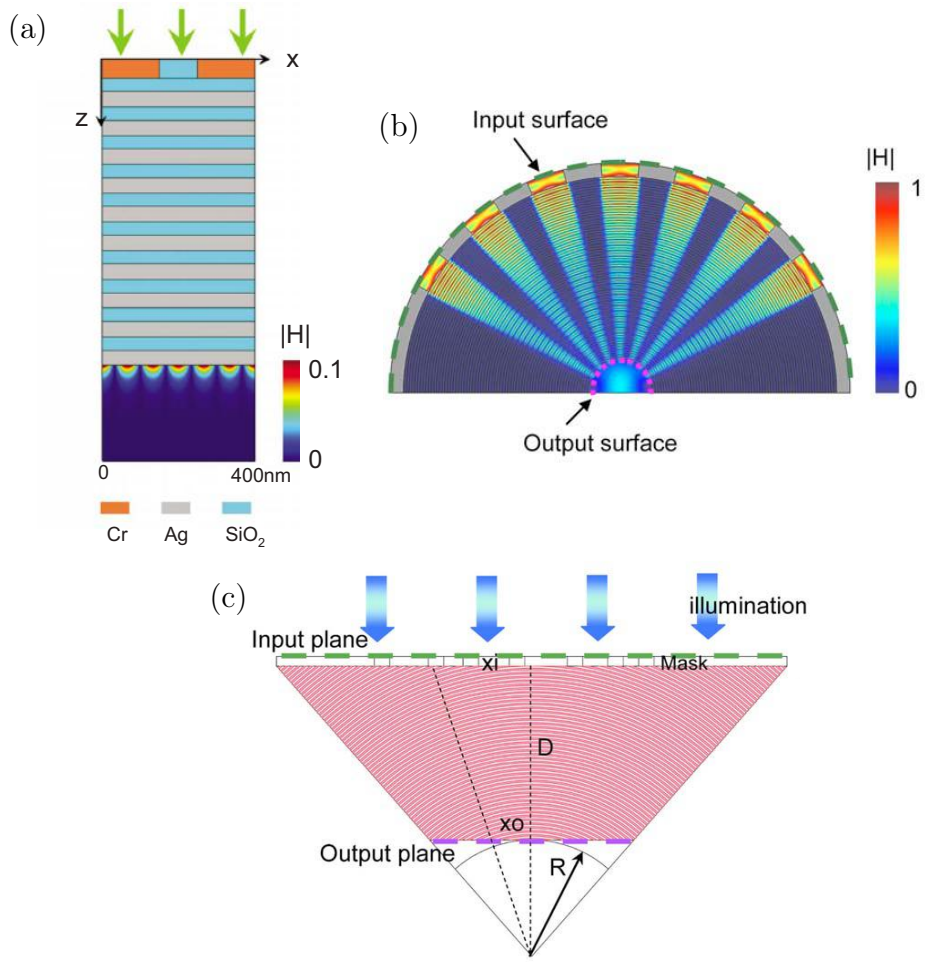

Figure 2.18: (a) Nanolithography assisted by a ML slab: light (green arrows) incident on a 1D mask is converted into a sub-diffraction pattern. The color diagram represents the simulated magnitude of the H-field after the ML. Only one period (400 nm) of the Cr grating mask is shown. (b) Magnitude of the H-field in a cylindrical hyperlens used for nanolithography, showing the conversion of a 1D diffraction-limited pattern at the input surface into a sub-diffraction-limited one at the output surface. (c) Schematic of nanolithography with a flat interface hyperlens. (a) reproduced from Ref. [133], (b) and (c) from Ref. [11].

2.3.2 Spontaneous emission engineering

Solid state lighting [134, 135], optical communications [136], quantum computing with single photons [137, 138] and fluorescence imaging [139] are examples of research fields where enhancing spontaneous emission from quantum sources (single atoms, ions or molecules, quantum dots, electron-hole pairs in quantum wells, color

and nitrogen-vacancy centers in diamond, defects in SiC) is highly desirable. Such quantity depends not only on the dipole moment μ of the transition, but also on the electromagnetic environment that hosts the emitter [24]. Fermi's Golden Rule states indeed that an initial excited state with 0 photons $|i,0_{\mathbf{k}}\rangle$ decays into a final state $|f,1_{\mathbf{k}}\rangle$ with 1 photon of wavevector $\mathbf{k}$ at a rate [140]

$$\Gamma_{fi} = \frac{2\pi}{\hbar} |\langle f,1_{\mathbf{k}}| H_{int} |i,0_{\mathbf{k}}\rangle|^2 \rho(\hbar\omega_{\mathbf{k}}). \tag{2.23}$$

where $\hbar$ is Dirac's constant, $H_{int} = \mu \cdot \mathbf{E}$ is the Hamiltonian of interaction between the dipole moment and the electric field $\mathbf{E}$ and ρ is the photonic density of states, namely the density of available final photon states with frequency $\omega_{\mathbf{k}} = \omega_{fi}$, the transition frequency. ρ can be increased with respect to its value inside a homogeneous dielectric medium, conventionally termed "free space", by suitably designing the emitter's surroundings.

The concept of SE engineering was originally explored by Purcell, who quantified the ratio between the SE rate in a cavity at radio frequencies and the SE rate in free space as $F_P = 3\lambda_0^3 Q/4\pi^2 n^3 V$ [141]. This *Purcell factor* relates the SE enhancement at the resonant wavelength $\lambda = \lambda_0/n$ to the quality factor Q and the mode volume V of a cavity with refractive index n. The Purcell factor has been extended as a figure of merit to optical cavities of micrometric [142] and nanometric size, for instance formed by defects in photonic cystals [136] or by metallic-coated semiconductor pillars [143]. The imperfect confinement of radiation at nanoscale requires Purcell enhancement to be deducted either indirectly from lifetime measurements [136] or by properly redefining Q and V [143].

Plasmonics offers to SE engineering a physical route alternative to the constructive interference exploited in cavities. An emitter embedded in a dielectric medium within the near-field of a metallic flat surface relaxes from an excited state via three competing

processes: the emission of a photon that propagates in the far field, the emission of a surface plasmon polariton bound to the metal/dielectric interface, and the generation of lossy surface waves, that account for electron scattering and electron-hole excitation [144, 145]. A SP increases the PDOS by channeling the emission into k-vectors larger than those accessible with photons ($k > k_0$); nevertheless, it constitutes a decay route inherently radiative, although to be observed in the far field it requires a natural (metallic surface roughness) or artificial (dispersion of nano-sized scatterers on the metallic surface, periodic nanopatterning of said surface) outcoupling mechanism [134].

Both the cavity and the SP approach have the intrinsic disadvantage of being resonant processes, which limits the overlap of the enhanced modes with the emission spectrum of the source. HMMs overcome these drawbacks thanks to their peculiar structure [146]. In a ML HMM, several parallel metal/dielectric interfaces are aligned at distances of a few tens of nanometers from each other. The mutual interaction of these interfaces, which individually support the same plasmonic resonance, results in a hybridized response [147, 19]. In other words, the single plasmonic mode of a conventional metal/dielectric boundary (Fig. 2.19(a)) is replaced by multiple modes which cover a broader portion of the frequency spectrum (Fig. 2.19(b)). The same kind of coupling occurs between the metallic rods of a NW HMM, except in this case not only propagating surface plasmons but also localized surface plasmons are involved.

The SE enhancement allowed by HMMs possesses therefore the unique feature of being broadband. It is also easily tunable at the design stage by adjusting the metal filling ratio p [18]. The efficiency of such mechanism is inevitably reduced by the ohmic losses associated with the metallic constituent [148]. Nonetheless, compared to a bulk metallic medium of the same size (corresponding to a filling ratio p of 1), a HMM displays lower ohmic dissipation, as the percentage of metal in the structure is always less than 100% ($p < 1$).

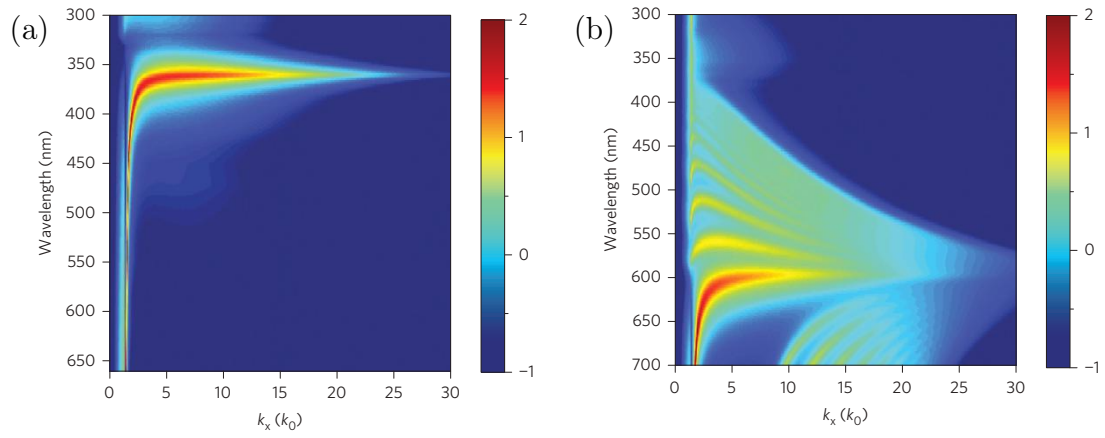

Figure 2.19: Normalized dissipated power spectra (intensity on a logarithmic scale) for a dipole perpendicular to and at a distance of d=10 nm above a uniform Ag single layer (a) and a Ag/Si multilayer HMM (b), each with the same total thickness of 305 nm. Reproduced from Ref. [18].

The capability of increasing the decay rate can be directly inferred from the anisotropic properties of hyperbolic media. A mode-counting procedure in k-space shows indeed that the PDOS at the angular frequency ω is proportional to the shell delimited by the isofrequency surfaces at ω and $\omega + d\omega$ [55]. In the case of an isotropic environment, such shell is spherical: therefore, it encloses a limited portion of the k-space, resulting in a finite PDOS. In the frequency range where a material behaves ideally as hyperbolic, the shells become instead hyperboloidal, and as such unbounded, leading to a broadband singularity in the PDOS. In real implementations, the number of available photon states is prevented from becoming infinite by several factors [149, 146]. First, the finite size a of the unit cell imposes an upper limit $k_{max} \sim 1/a$ to the maximum k-vector supported by the metamaterial along the direction of periodicity; accordingly, $\rho \sim k_{max}^3$ [55, 149, 146, 150, 151]. It was shown that the PDOS becomes infinite only in the limit of infinitesimally small emitter; a realistic spherical source of characteristic size s can achieve a maximum Purcell factor $\sim \lambda_0^3/s^3$ [151]. Furthermore, a finite distance from the HMM limits the access of the emitter to the largest k-vectors potentially available

[146]. Finally, describing the permittivity of the metallic constituent of a ML with the hydrodynamic Drude model introduces spatial dispersion, which in turn leads to an upper bound to the PDOS proportional to ω^2/v_F^3, where v_F is the electron Fermi velocity of the metal [70].

As mentioned in the previous paragraph, to evaluate the SE enhancement induced by HMMs one can associate to such structures a suitable Purcell factor. Rather than adapting the original formula by Purcell, which is difficult since the radiation confinement is not as strong as in a cavity, a reasonable solution is to compute straightforwardly $F_P = \Gamma_{HMM}/\Gamma_0$, where Γ_{HMM} and Γ_0 are the SE rates in the presence of the hyperbolic environment and in free space.

This ratio can be obtained by means of the dyadic Green function $\overline{\overline{G}}$, a mathematical tool utilized to predict the emission patterns of point-like sources inside different environments [24]. In hyperbolic media, both the electric field of a point dipole and the associated Poynting vector exhibit a characteristic conical shape, due to the anisotropic wave propagation discussed in Subsection 2.2.1 [152, 150]. The Green tensor was used to determine the Purcell factor of a single dipole embedded in a homogeneous hyperbolic space [152] and in an infinite cubic lattice of interacting dipoles in vacuum, where the hyperbolic properties were contained in the polarizability $\overline{\overline{\alpha}}$ of the individual grid elements (Discrete Dipole Approximation) [150]. In the case of layered media, $\overline{\overline{G}}$ in the half-space above the ML can be obtained by adding up the free space field and the field reflected from the anisotropic region, retrieved with a transfer matrix method [58] or with an effective transmission line theory [153]. Effective permittivities accounting for a nonlocal metallic response were implemented in the Green function of a ML HMM, and were predicted to suppress the singularity of Purcell factors computed in local approximation [70].

An approach alternative to the one discussed above extends the tractation of Ford

and Weber, who developed a SE enhancement formula for single plasmonic interfaces [144], to the case of ML HMMs [43, 154, 18]. This semiclassical method approximates ratios of rates with ratios of powers, and is equivalent to a fully quantum theory in the weak coupling limit [154, 155]. In [18] and [19], a method was proposed to compute the Purcell factor of uniform or nanopatterned HMM structures with finite element method (FEM) simulations. A derivation of the Purcell factor for a medium with elliptical and hyperbolic dispersion in the framework of quantum optics was carried out in [156].

Several experiments have been conducted to demonstrate SE modification in HMMs for a variety of quantum sources [55, 87, 56, 43, 157, 57, 18]. The temporal signature of Purcell enhancement is a decrease in the lifetime of the emitters when the latter are dispersed within the near field of the hyperbolic medium. Fig. 2.20(a) shows the decay curves of single molecules separated by a 21 nm transparent spacer from different substrates of identical thickness 305 nm, represented by a single layer of dielectric (Al_2O_3), a single layer of metal (Au), and a ML of 8 dielectric/metal periods

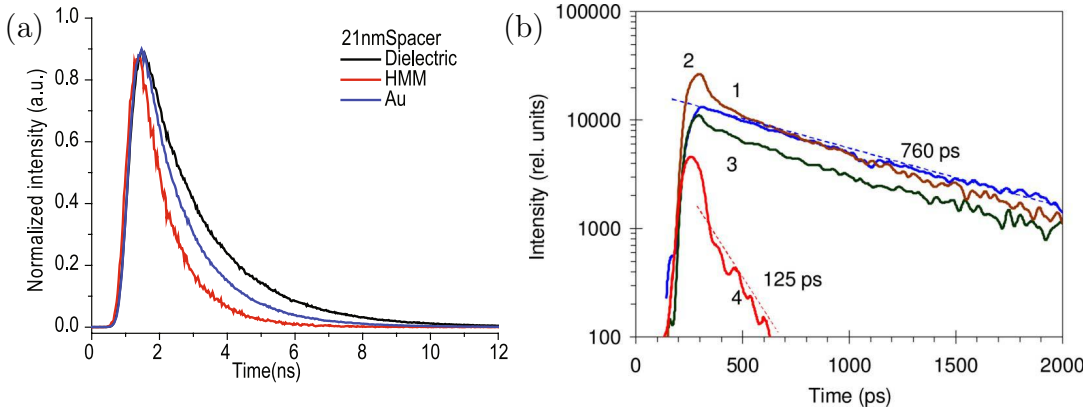

Figure 2.20: Enhanced spontaneous emission of dye molecules on multilayer and nanowire HMMs. (a) SE dynamics of Rhodamine 800 excited at $\lambda_0 = 635$ nm on top of Al_2O_3 (black), Au (blue) and a Au/Al_2O_3 multilayer (red). (b) SE dynamics of IR140 excited at $\lambda_0 = 800$ nm on top of (1) a pure Al_2O_3 membrane, (2) a Au film on glass, (3) a Ag film on glass, and (4) a Ag/Al_2O_3 nanowire medium. (a) reproduced from Ref. [55], (b) from Ref. [87].

[55]. The introduction of a spacer is necessary, since excessively short distances from the metallic or the HMM surface would make quenching in metal the dominant decay channel. While the metallic substrate exhibits a faster decay than the dielectric one, due in part to plasmons excitation and in part to quenching, the ML achieves an even better performance thanks to its large number of hyperbolic states available and to the lower ohmic losses. SE can be enhanced also in NW media [87]. In Fig. 2.20(b), deposition on an Al_2O_3 template filled with Ag nanowires causes the lifetime of a laser dye, measured to be 760 ps on top of the void template, to drop to 125 ps. The comparison with Au and Ag substrates, where quenching due to ohmic losses is expected to be higher than in the HMM, connects again the observed change to the excitation of high-k propagating waves rather than of lossy waves. CdSe/ZnS quantum dots were utilized to probe the optical topological transition (cf. Fig. 2.6) in a Ag/TiO_2 ML with filling ratio 29% [43]. When the wavelength λ_0 crossed the critical point $\lambda_{0,c} = 621$ nm, the effective parameters of said HMM evolved from the elliptic to the hyperbolic regime. The correspondent increase in the PDOS manifested itself in a shortening of lifetime, clearly discernible in Fig. 2.21. For the present application, the choice of QDs was critical: their photoluminescence (PL), peaked at $\lambda_{0,c}$, had a full-width at half-maximum (FWHM) of ~ 40 nm, which allowed the characterization of both the elliptical and the hyperbolic behavior on the same sample. Even larger FWHMs are exhibited by nitrogen-vacancy (NV) centers in diamond, promising candidates for the field of quantum information as they show single-photon generation and long spin coherence times [158]. An efficient production of quantum bits relies on a broadband SE enhancement mechanism, essential to match the spectrally wide emission of these light sources. The interaction between NV centers in nanodiamonds and a Au/Al_2O_3 ML was studied in a recent work [57]. Over the spectral interval $650 - 720$ nm, the average lifetime on top of the HMM was reduced by a factor of 13.48 with respect to a control sample (Fig. 2.22), resulting in an experimental Purcell

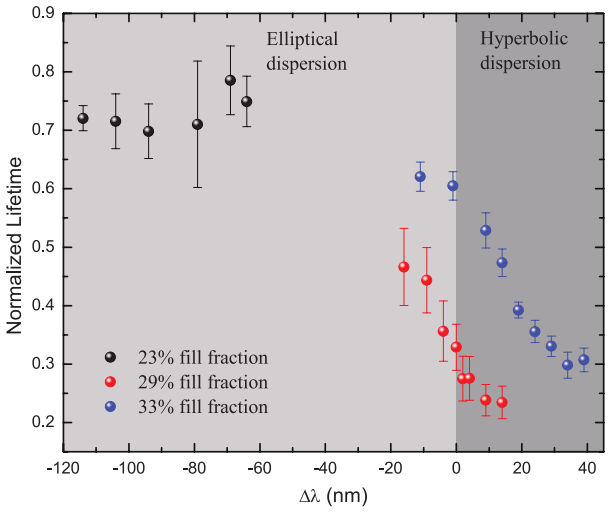

Figure 2.21: Lifetime of CdSe/ZnS colloidal quantum dots on top of Ag/TiO_2 MLs with different filling ratios, normalized to the control samples. $\Delta\lambda$ represents the detuning with respect to the topological transition wavelength, $\lambda_{0,c} = 621$ nm, at the filling fraction 29%. Reproduced from Ref. [43].

factor of 2.57. Finally, SE enhancement when the source is located inside a HMM rather than on top of it was explored experimentally, by functionalizing layers of dielectric with dye molecules [61], and with theoretical studies [19, 154]. A dynamically tunable Purcell enhancement can be achieved at far-infrared frequencies if the metal layers are replaced with graphene sheets [47, 49].

Despite the emission speed is increased in the presence of HMM substrates, the emission intensity is always concomitantly reduced. The high-wavevector states responsible for the SE enhancement are indeed propagating inside the hyperbolic medium, but become immediately evanescent as they enter the outer isotropic space. As a result, the net amount of radiation that reaches the far field is decreased with respect to free space, unless a conversion mechanism is introduced that outcouples the "trapped" waves. The extra k-vector that impedes propagation in free space can be lost by scattering with natural or artificial corrugations of the HMM surface, such as nanoparticles or gratings with various geometries and shapes (Figs. 2.23(a) and 2.23(b)) [18, 19]. Figs. 2.23(c) and

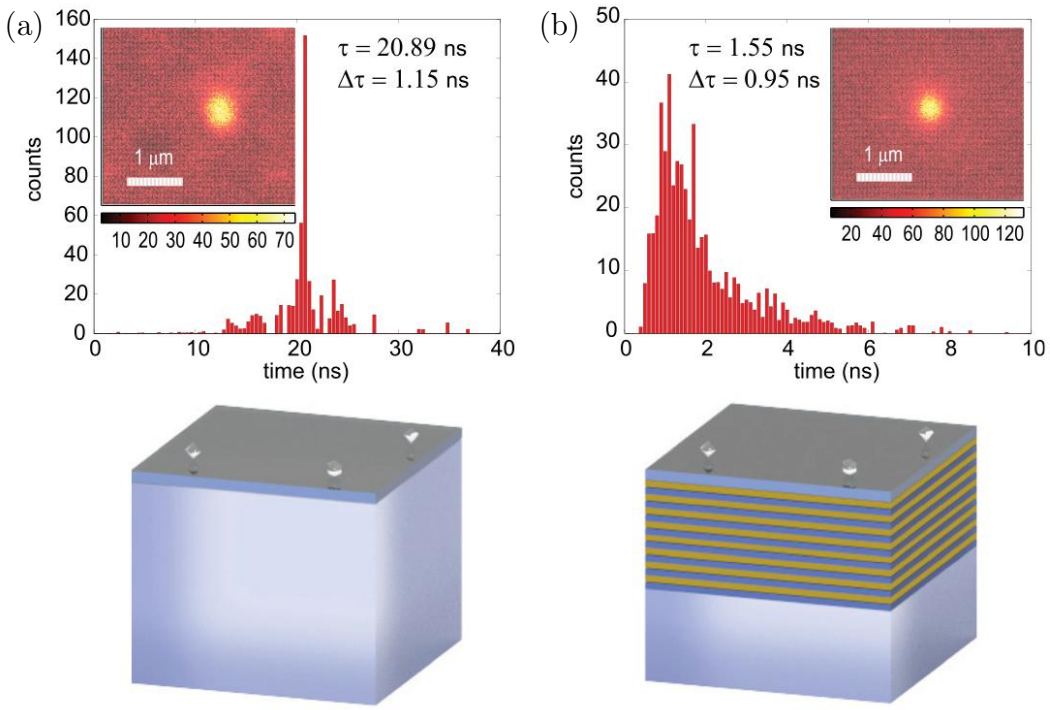

Figure 2.22: Histograms of spontaneous emission lifetimes of Nitrogen-Vacancy centers in diamond on top of (a) a glass coverslip (control sample) and (b) an Al_2O_3 multilayer. The corresponding mean value and standard deviation of the lifetime distribution are (a) 20.89 ns and 1.15 ns, (b) 1.55 ns and 0.95 ns. Reproduced from Ref. [57].

2.23(d) show the dependence of Purcell factor and intensity enhancement on the period of 1D gratings with rectangular profile patterned in a Ag/Si ML. As the grating period is decreased, both quantities increase, the change becoming more marked below 150 nm. A finer periodicity results indeed in a better match with high-k plasmonic modes; a period of 80 nm reaches a Purcell factor as high as 76, and an intensity enhancement with respect to an unpatterned ML close to 80-fold, much higher than the 8-fold one achieved with larger periods.

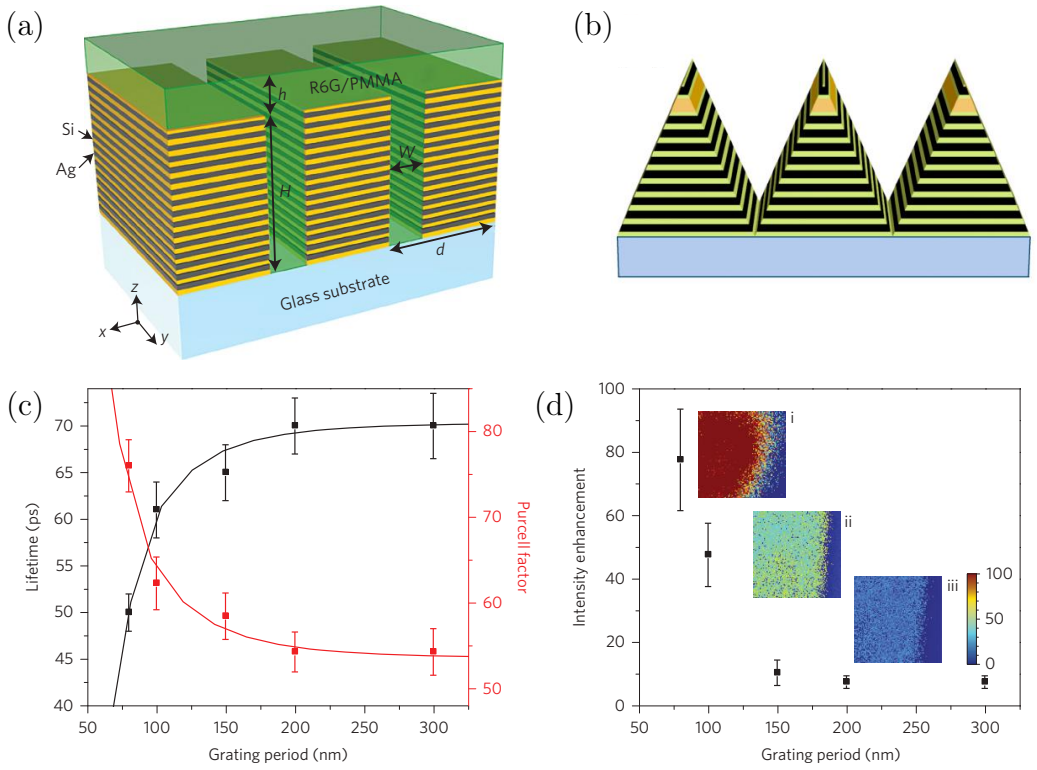

Figure 2.23: (a) and (b): outcoupling geometries for multilayer hyperbolic metamaterials. (a) rectangular 1D grating patterned on a Ag/Si multilayer, with emitters contained in the green region. (b) triangular 1D grating patterned on a Ag/Si multilayer, with emitters contained in the ochre region. (c) Spontaneous emission lifetime (black) and corresponding Purcell factor (red) for the dye molecule Rhodamine 6G on the nanopatterned Ag/Si multilayer of Fig. 2.23(a), as a function of the grating period. The solid lines are a guide to the eye. (d) Fluorescence intensity enhancement for Rhodamine 6G on the nanopatterned Ag/Si multilayer of Fig. 2.23(a), as a function of the grating period. Insets: optical images of the fluorescence intensity accumulated over 100 frames (grating periods: (i) a=80 nm; (ii) a=100 nm; (iii) a=200 nm). Error bars represent the fluctuations in fluorescence photo-counts. (a), (c) and (d) reproduced from Ref. [18], (b) from Ref. [19].

2.3.3 Thermal emission engineering

The power emission of a black body at thermal equilibrium is ruled by Planck's law. Although this limit cannot be overcome in the far-field, the same is not true in the near-field, where the high PDOS of HMM leads to super-Planckian thermal emission [159]. The potential applications of this phenomenon span from energy harvesting

and conversion to thermal coeherent sources and thermal sinks [53, 54]. In order to engineer heat transfer, researchers focussed their attention on SiC, a phonon-polaritonic metal where the real part of permittivity becomes negative in the infrared inside the Reststrahlen band, delimited by the transverse and the longitudinal optical phonon resonance frequencies [53]. HMM ML formed by stacks of SiC and SiO_2 layers exhibit three advantages. First, their high-k states can be thermally excited at moderate temperatures around 400-500 K, where the peak of the black body curve falls within the Reststrahlen band. Second, phonon-polaritonic metals have lower losses compared to plasmonic metals, and therefore the contribution of high-k modes dominates that of lossy surface waves. Third, as SiC/SiO_2 MLs operate in the wavelength interval 10-12 µm, the fabrication of subwavelength layers (period 50-100 nm) is relatively easy, and the effective medium theory is more accurate with respect to the optical range. For the same reason, the engineered near-field (distances $z \ll \lambda_0$) can be accessed experimentally with conventional detection systems.

The optical phase diagram of SiC/SiO_2 MLs is shown in Fig. 2.24(a). The emitted

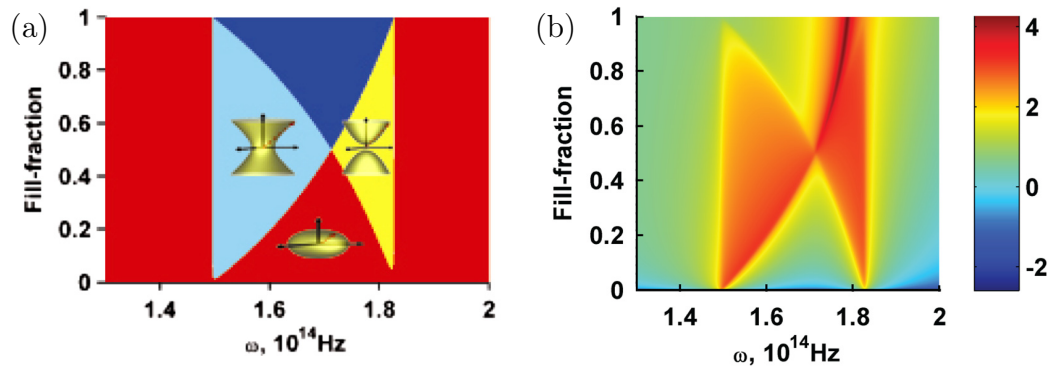

Figure 2.24: (a) Optical phase diagram of a SiC/SiO_2 multilayer HMM showing the different optical isofrequency surfaces achieved in different regions. The dark blue area denotes an anisotropic effective metal where propagating waves are not allowed. (b) Super-Planckian thermal emission in the near field of the HMM (normalized to the black body radiation into the upper half-space) calculated analytically. Reproduced from Ref. [53].

energy density of a HMM in equilibrium at temperature T, at distances z restricted to the near field and in the limit of low losses is given by [53]:

$$u(z,\omega,T)^{z\ll\lambda_0} \approx \frac{U_{BB}(\omega,T)}{8}\left[\frac{2\sqrt{|\varepsilon_{xx}\varepsilon_{zz}|}}{(k_0 z)^3(1+|\varepsilon_{xx}\varepsilon_{zz}|)} - \varepsilon''\frac{2(\varepsilon_{xx}+\varepsilon_{zz})}{(k_0 z)^3(1+|\varepsilon_{xx}\varepsilon_{zz}|)^2}\right], \quad (2.24)$$

where $U_{BB}(\omega,T)$ is the black body emission spectrum at temperature T, and ε_{xx}, ε_{zz} and ε'' are the real and imaginary parts of the permittivity components $\varepsilon_{\parallel} = \varepsilon_{xx} + i\varepsilon''$ and $\varepsilon_{\perp} = \varepsilon_{zz} + i\varepsilon''$ parallel and orthogonal to the layers. The first term represents the contribution of high-k modes, and greatly exceeds the second, related to lossy surface waves. Eq. (2.24) is plotted in Fig. 2.24(b) for a SiC/SiO_2 system; the comparison with the phase diagram of Fig. 2.24(a) highlights that emission enhancement is attained only in the hyperbolic regime, where the PDOS is larger.

Thanks to their capability of altering near-field thermal emission, HMMs can increase heat transfer from and to materials which support infrared surface polariton resonances. A lattice of Au NWs in vacuum was shown to enhance non-resonantly the heat flux from a SiC emitter [160]. Heat exchange through a tiny gap between two SiC/SiO_2 ML HMMs exceeds the performance of analogously arranged black bodies, and is mainly influenced by the surface modes of the topmost layers [161].

Thermophotovoltaic devices require heat transfer at high temperatures and near-infrared frequencies; to this end, the operating range of thermal hyperbolic MLs can be tuned to 1-3 μm by utilizing aluminum zinc oxide (AZO, plasmonic metal) and TiO_2 [54].

2.3.4 Active and tunable devices

Like in many other metamaterials designed for exhibiting extraordinary optical properties, the performance of hyperbolic media is limited by the ohmic damping associated with free charge carriers, which imposes a cut-off on the achievable wavenumber of the propagating modes [157]. High wavenumbers correspond to a stronger concentration of electric field inside metals: as a consequence, the associated modes experience larger ohmic losses which prevent long propagation. This proves detrimental especially for the detection of sub-wavelength objects. It was shown numerically that lossless HMMs can achieve much higher resolution than those with realistic ohmic damping [109]. In addition, gain-compensated hypergrating structures were predicted to produce narrower focal points than their passive counterparts [162]. It is therefore desirable to incorporate gain materials, such as dye molecules and semiconductors, in the HMM design.

Thanks to the non-resonant nature of HMMs, loss compensation can be achieved with lower gain coefficients than those required by resonance-based artificial media. Numerical investigations were carried out to eliminate the influence of losses in metal/dielectric MLs [162, 163, 164]. TM-polarized propagating modes can be over-compensated by a gain medium with an imaginary part of the permittivity as low as $\varepsilon'' = -0.04$. This corresponds to a gain coefficient of about $2000\,\mathrm{cm}^{-1}$. The above numerical studies only considered stimulated emission from the gain material. In addition, spontaneous emission can also be induced, which is undesirable for imaging and focusing purposes as it produces blurring background. The noise generated by spontaneously emitted light is amplified, eventually reaching the so-called convective instability as the gain material gets pumped harder [163]. Therefore, the point of total compensation should be avoided for all the propagating modes in the HMM. To the best of our knowledge, a rigorous treatment incorporating the nonlinear dynamics of the carriers, such as exciton saturation, in the gain material has not been carried out, nor has the experimental demonstration of

gain-assisted imaging or focusing been achieved.

Realistic candidates as gain media can be identified among the materials utilized in active plasmonics. Khurgin and Boltasseva [148] estimate that a gain of the order of $10^3 - 10^4$ cm^{-1} is required to compensate for the ohmic damping in metals. This value is attainable in semiconductors with an injected carrier density of $\sim 10^{18}$ cm^{-3}, although the pumping current density needed to maintain such concentration might be unpractical. Stimulated emission of SPs has been observed in the visible and near infrared in structures including, besides electrically pumped semiconductor gain media [143, 165], a dye solution [166, 167], a dye-doped polymer [168, 169, 170, 171], dye-doped SiO_2 shells [172], Er-doped SiO_2 [173], a quantum-dot-doped polymer [174], and CdS nanowires [175]. A direct measurement of gain in propagating SPs was reported by De Leon and Berini [167]. The analyzed structure consists in a symmetric Au-stripe waveguide, 20-nm thick and 1-μm wide, deposited on SiO_2 and covered with a gain layer of IR140 dye molecules in solution (1 mM concentration). When the latter are optically pumped, not only the losses are totally compensated, but the power of the probe beam coupled out of the structure is also 10% larger than the injected one. Several details govern the effectiveness and the repeatability of the active operation regime: 1) the gain anisotropy, determined by the relative polarization of the probe (cw Ti:sapphire laser) with respect to the pump (pulsed Nd:YAG laser); 2) the duration of the measurement, as the dye molecules - in the absence of recirculation of the solution - undergo photochemical modifications after 5 minutes of pump and probe illumination; 3) the thermal stability of the solution, that needs to be thermo-electrically cooled and enclosed in a dry environment to prevent thermo-optic modifications of its refractive index; 4) the local heating of the metal film during the pump pulse, resulting in a slight islandization of the film itself and therefore in a degraded performance; 5) the possible pulse-to-pulse energy variations of the pump signal, which can be taken into account by averaging the gain measurement

over multiple pump pulses. Another experiment demonstrated an active negative-index metamaterial based on a fishnet structure [170]. The gain medium is represented here by a 50-nm epoxy layer doped with Rh800 dye (20 mM concentration), sandwiched between two 50-nm Ag layers. The material gain, extracted by matching numerical simulations with the experimental measurements, results $2800\,\mathrm{cm}^{-1}$. Salient aspects of the device characterization are: 1) the use of the same source (pulsed Ti:sapphire laser) to generate both the pump and the probe pulses; 2) the optimization of the time delay between the pump and the probe pulses, to ensure that the dye offers the maximum gain; 3) the use of an average pump power of 1 mW, below the damage threshold for the sample but 5 times larger than the gain saturation power of the doped epoxy; 4) photobleaching of the dye molecules, observed after 5 minutes of illumination; 5) the good match between optical measurements without pump and with a detuned delay between pump and probe (i.e. the pump is turned on, but does not operate effectively), which excludes influences from the setup or local heating.

A tunable behavior can be achieved in ML HMMs by means of graphene, a material that supports plasmonic resonances in the THz frequency range [176, 126, 177]. Its attractive features include low loss, high confinement of electromagnetic energy and fast response time. The conductivity of graphene can be tuned by shifting the Fermi level with an external electric field. This suggests that a dramatic optical phase change from the elliptical to the hyperbolic regime through the ENZ point can be induced in graphene-based MLs by varying the electrical doping level [47, 49, 178]. The ultrathin graphene sheets, with their strong in-plane polarizability[2] [180], would play the role of the metal, with the further advantage of lower absorption and a reduced overall ML thickness.

The integration of graphene in ML hyperbolic structures was proposed and

[2] As already mentioned, graphite, naturally consisting of stacked graphene layers, exhibits indefinite permittivity tensors both in the ultraviolet and in the THz region [40, 179].

theoretically investigated in recent works [47, 49, 50]. A controllable elliptic-hyperbolic phase transition would imply sharp changes in reflection and transmission through the HMM, in the near-field absorption properties and in the Purcell effect.

2.3.5 Emerging topics

By virtue of the high k-vectors supported, ML HMMs can be shaped into deep sub-wavelength three-dimensional cavities (Fig. 2.25(a)), with sizes down to $\lambda/12$ [182, 65]. In addition to the extreme confinement, HMM resonators also exhibit anomalous scaling properties: cavities of different sizes resonate at the same frequency, and higher-order modes oscillate at lower frequencies. The radiative quality factors Q_{rad} were shown to

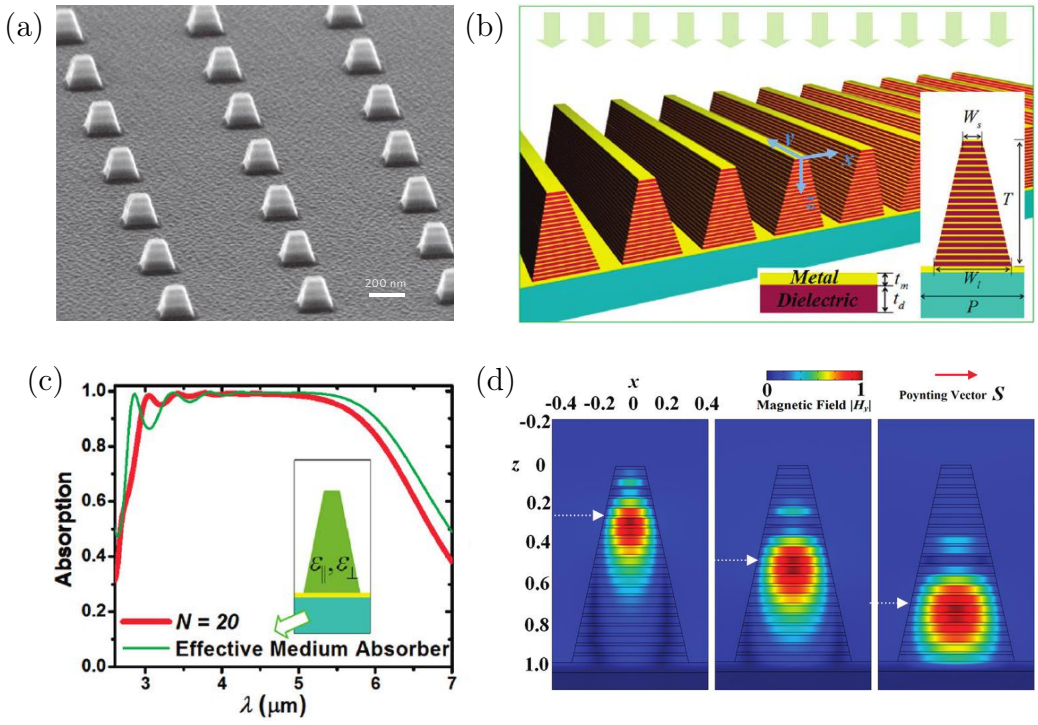

Figure 2.25: (a) SEM image of an indefinite optical cavity array composed of Ag/Ge multilayers. (b) Schematic of a broadband absorber based on tapered HMM waveguides. (c) and (d) show respectively the absorption spectrum of the structure (N=number of periods) and the distribution of magnetic field at increasing wavelengths (left to right: λ_0=3.5 μm, λ_0=4.5 μm, λ_0=5.5 μm). (a) reproduced from Ref. [65], (b), (c) and (d) from Ref. [181].

scale according to the universal power law $Q_{rad} \approx n_{eff}^4$, where $n_{eff} = k/k_0$ represents the effective refractive index of the resonator.

Rainbow trapping of electromagnetic fields in tapered HMM waveguides was discussed in [181, 183]. Broadband light trapping can be realized by slowing down radiation in stop bands corresponding to different frequency-dependent positions along the waveguide [184, 185, 186]. In the proposed HMM approach, ML waveguides are tapered along the direction orthogonal to the layers, allowing normally incident waves to be directly coupled and stored inside the structures (Fig. 2.25(b)). The absorption spectrum of a Au/Ge device [181] shows a broadband response in the near-infrared range (Fig. 2.25(c)), with light of different wavelengths being concentrated in different layers (Fig. 2.25(d)). The operating range of HMM waveguide absorbers can be extended to mid-infrared frequencies with a proper material choice. In addition to rainbow trapping, other light absorption schemes that benefit from the large PDOS of HMMs were investigated theoretically and experimentally [62, 153, 187, 188].

When two Ag/Ge ML hyperbolic waveguides are separated by a nanoscale air gap (Fig. 2.26(a)), an excitation beam directed along the slit causes the insurgence of giant optical forces up to $8\,\mathrm{nN\,\mu m^{-1}\,mW^{-1}}$ [189]. This phenomenon is induced by the large effective refractive indices $n_{eff,z} = k_z/k_0$ inside the two HMMs and their strong dependence on the slit size. The generated forces tend to attract the two HMM waveguides, and are transverse to the power flux of the beam. Thanks to the non-resonant nature of hyperbolic media, the described optical interaction can be triggered by a broadband excitation.

A dipole placed in a hyperbolic volume experiences a self-induced torque, originating from spatial anisotropy [190]. Spontaneously emitted photons exert reaction forces on the dipole that produces them. In an isotropic environment, two photons emitted into opposite directions generate forces that cancel each other. However, when the dipole

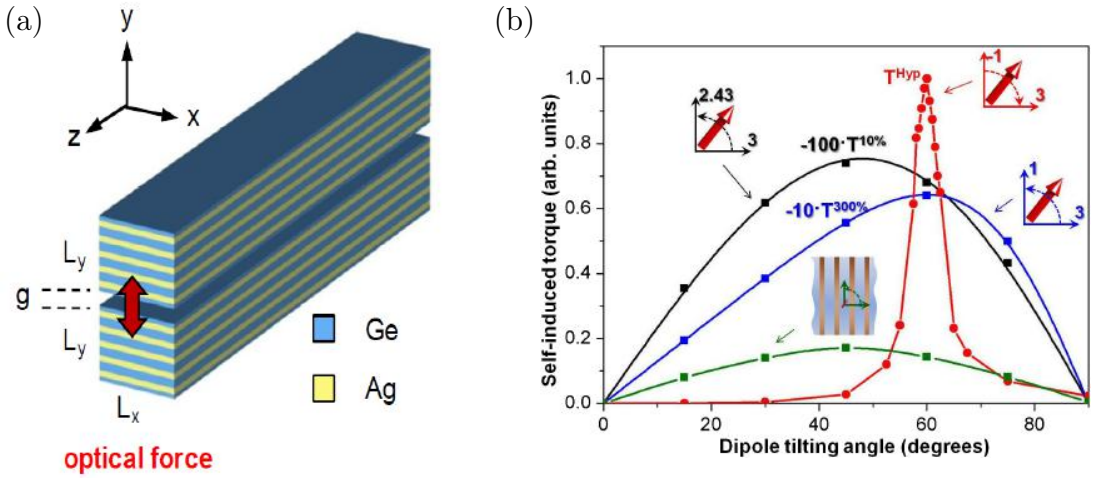

Figure 2.26: (a) Transverse optical force (red arrows) induced on two HMM waveguides by a driving beam directed along the slit. (b) Torque on a 2 nm size dipole situated in media with different anisotropy as a function of its tilting angle with respect to the extraordinary axis: $\varepsilon_\perp = 2.42$, $\varepsilon_\parallel = 3$ (black squares), $\varepsilon_\perp = 1$, $\varepsilon_\parallel = 3$ (blue squares), $\varepsilon_\perp = -1$, $\varepsilon_\parallel = 3$ (red circles), layered metamaterial with effective parameters $\varepsilon_\perp = -1 - 0.2i$, $\varepsilon_\parallel = 2.9$, not scaled (green squares). Black and blue lines are analytical fits, red and green lines are guides for the eye. The rotation directions are indicated in the insets. (a) reproduced from Ref. [189], (b) from Ref. [190].

is placed in an anisotropic medium and its orientation is misaligned with respect to the principal axis, its radiation pattern becomes asymmetric. As a consequence, a net restoring torque tends to align the dipole with the medium (Fig. 2.26(b)). The large PDOS enhances the emission rate, and therefore strengthens the phenomenon: the torque experienced by a dipole in a ML HMM is at least an order of magnitude higher than that in an anisotropic dielectric medium.

The Casimir force in a lattice of metallic nanowires embedded in three dielectric fluids was studied in [191]. Such effect originates from the quantum zero-point energy, and plays a significant role in micromechanical systems [192]. The two interfaces at distance d formed by the fluids induce a restoring Casimir torque on the nanowires if the latter are misaligned with respect to the equilibrium position (normal to the interfaces); this interaction scales as $1/d$, in contrast with the $1/d^3$ law predicted for two parallel

birefringent plates in vacuum [193].

2.4 Current challenges and future directions

2.4.1 Limitations of the effective medium description and quantum size effect

We have highlighted during our analysis of SE in HMM (Subsection 2.3.2) how, in addition to absorption, the finite period size, the internal structure of the emitter and the non-vanishing distance between the source and the HMM remove the PDOS divergence dictated by the EMT. The deviation from the effective medium description in finite-sized HMMs can be modeled as a nonlocal effect, so that the permittivity components become functions not only of the frequency, but also of the wavevector [67, 149]. A comparison between local (hyperbolic medium with effective parameters) and nonlocal (real layered structure) dispersion is shown in Figs. 2.27(a)–2.27(c). It was found that in finite-sized structures two propagating modes can occur simultaneously near the ENZ point [67, 194]. Such coexistence of both forward and backward propagating waves is not predicted by the EMT, and leads to an anomalous refraction behavior at the air-HMM interface (Figs. 2.27(d)–2.27(f)).

When approaching the limit of extremely small unit cells (of the order of few nanometers and less), the effect of electronic confinement in the metal constituents ("quantum size effect") needs to be considered. In a classical picture, where the charge carriers in metals move independently from each other, the electric displacement field D is described by means of a local response function,

$$D(\omega, \mathbf{r}) = \varepsilon(\omega, \mathbf{r})\varepsilon_0 E(\omega, \mathbf{r}), \tag{2.25}$$

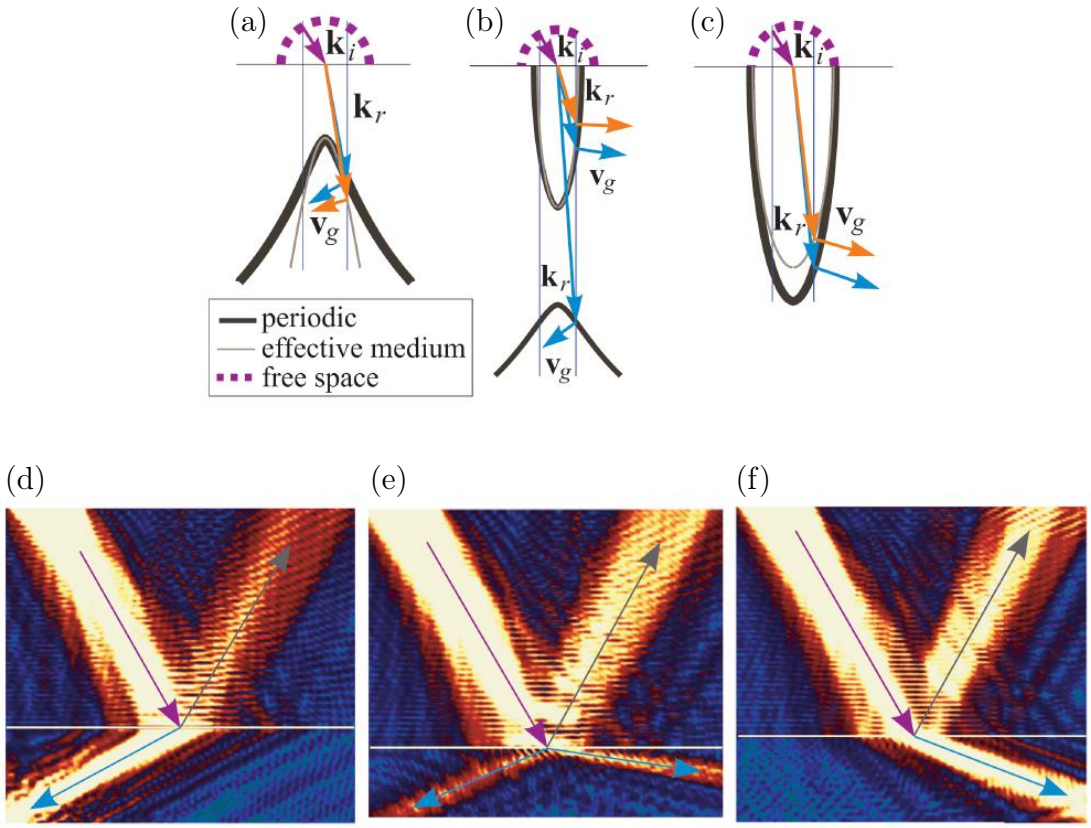

Figure 2.27: Diagrams of beam refraction at the interface between air and a ML HMM with period D at three different frequencies: (a) $D/\lambda = 0.085$, (b) $D/\lambda = 0.094$, and (c) $D/\lambda = 0.106$. The wavevectors $\mathbf{k}_i$, $\mathbf{k}_r$ of the incident and refracted waves and the group velocity $\mathbf{v}_g$ are plotted by means of the isofrequency contour method. The first Brillouin zone is rendered. (d-f) Numerical studies of the beam refraction in the three cases corresponding respectively to figures (a-c). Reproduced from Ref. [67].

where $\varepsilon(\omega, \mathbf{r})$ is the relative permittivity, ε_0 the vacuum permittivity, E the electric field, ω the angular frequency and $\mathbf{r}$ the position. As the metal size is progressively reduced, such approximation becomes inadequate, and a representation of light-matter interaction is required that includes the nonlocal response [195, 196, 197, 198]. In this case, the displacement field is given by

$$D(\omega, \mathbf{r}) = \int \varepsilon(\omega, \mathbf{r}, \mathbf{r}')\varepsilon_0 E(\omega, \mathbf{r}')d\mathbf{r}', \tag{2.26}$$

namely it depends on the neighboring E-field distribution rather than only on the local field. The nonlocal response cannot be neglected when the characteristic dimensions (such as particle size, nanowire width, or gap size) approach the Coulomb screening length: at this point the electron-electron interaction needs to be taken into account.

We remark that this kind of nonlocal effect is different from the one discussed at the beginning of the subsection, which originated from the finite size of HMMs homogenized with the EMT. Yan et al. showed in [70], by implementing a hydrodynamic model for the permittivity of metal, that the PDOS of a ML HMM in a quantum nonlocal framework does not diverge as $1/a^3$ (a being the ML period). Instead, it reaches the maximum value $(c/v_F)^3$, where c is the speed of light and v_F is the Fermi velocity of the metal. The same model also implies that the hyperbolic shape of the isofrequency contours is altered even if $a \ll \lambda_0$. The effects of nonlocal response on a hyperlens were analyzed in [72]. It was found that the optimal imaging frequency of the hyperlens is blueshifted with respect to analogous predictions based on the local response theory.

Ehsan et al. considered the propagation of quantum light states in a ML HMM with gain compensation [73]. They pointed out that the quantum noise or the quadrature variance of the E-field with a squeezed input state cannot be obtained using the conventional EMT, particularly in loss-compensated HMMs where it predicts vanishing quantum noise. Loss compensation in HMMs is not accompanied by quantum noise compensation, and quantum noise in ML HMMs is larger than in effective media. To formulate a quantum-optical EMT that successfully incorporated quantum noise in loss-compensated HMMs, Ehsan et al. introduced - besides effective permittivities - a new parameter, the effective noise distribution N_{eff}, that complements the description of photon propagation in HMMs.

2.4.2 Conclusions

The field of hyperbolic metamaterials originated from theoretical intuitions that found in plasmonics the key to be practically realized. A unique feature such as a tunable and broadband response makes of these media an exceptional tool of nanophotonics, and can speed up the transition from electronic to optical communications, both on a classical and on a quantum level.

Despite the increasing amount of theoretical works and proof-of-concept experiments, the leap towards the commercialization of the hyperbolic technology has been forbidden so far by a number of factors. Absorption losses, inherently connected to the use of plasmonic metals at optical frequencies, represent a significant problem, that can be mitigated by working at low filling ratios, implementing gain, or exploring alternative materials [199]. The PDOS mismatch between hyperbolic and free space makes it challenging to extract the information and the power carried by high-k states into the far field. Research in the incoming years should try to relax this bottleneck, by revisiting the geometry of hyperbolic structures or designing suitable outcoupling mechanisms (such as 1D or 2D gratings or nanoparticles with various sizes and shapes). A dynamic control of hyperbolic properties, extremely desirable in view of device production, has been proposed by means of graphene. Nonetheless, the extremely thin sheets of this material may be hard to integrate in a multilayer configuration, and graphene-based technology is currently limited to the THz range. No alternatives capable of operating in the visible or near-infrared range have emerged. Pushing the unit cells of MLs and NW arrays to sizes down to a few nanometers represents a further frontier that starts being approached. From the point of view of fundamental physics, the strong confinement of charge carriers and the scaling of material periodicity to the atomic level helps develop more accurate models of the radiation-matter interaction, including quantum effects, and can result in unprecedented phenomena. However, the experimental verification becomes challenging,

as it is extremely sensitive to thermal and electrical sources of noise, and requires a clever setup design. Furthermore, the time-consuming and expensive manufacturing processes, together with the low degree of tolerance to defects of fabrication, can severely curtail the integration of quantum HMMs in out-of-lab applications.

In conclusion, hyperbolic media are currently a hot and evolving research topic. Aspects such as nonlinear and quantum effects still need to find a proper theoretical frame. The frequency control of thermal properties can lead to extremely efficient photovoltaic devices, that optimize energy absorption and conversion. As scattering from HMMs can be strongly suppressed over large and tunable bands of frequency, these media may play a significant role for stealth technologies. Fluorescent tagging in the proximity of a hyperbolic environment can make faster and more efficient the detection of biomolecules. Finally, concepts already proven such as the hyperlens require further extensive studies, to conclusively assess - and overcome - their practical limitations. On the one side, given its thickness of hundreds of nm, a hyperlens can be integrated in an extremely thin smartphone or in a regular microscope, adding to them the capability of resolving the near field. On the other side, photolithography of nanoscale features by means of a hyperlens would represent a major breakthrough, as it would increase the density of data stored in optical devices, and of electrical components patterned on a chip.

In the following chapters, we narrow our focus on SE enhancement via HMMs. With the ultimate intent to fully integrate plasmonic and hyperbolic media into high-speed optical transmitters, we propose solutions to increase speed and efficiency of emitter-HMM systems, and to achieve large modulation bandwidth and effective light extraction from a blue plasmonic LED, at minimum cost for its proper diode behavior.

Chapter 2, in part, is a reprint of the material as it appears on Progress in Quantum Electronics 40, 1–40 (2015). L. Ferrari, C. Wu, D. Lepage, X. Zhang and Z. Liu,

"Hyperbolic metamaterials and their applications". The dissertation author is the first author of this paper.

Chapter 3

Enhancing spontaneous emission inside HMMs

3.1 Introduction

The enhancement of the recombination rates of point-source emitters represents a strategic objective for nanoplasmonics, given its high impact not only on light generation (single photon sources [200], light emitting diodes [134], and optical amplifiers [201]), but also on a host of other applications ranging from biosensing [202], fluorescence imaging [139] and DNA targeting [203] to the high speed modulation and detection of optical signals [136]. As discussed in Subsection 2.3.2, the rate of SE is proportional to the PDOS, which depends critically on the geometry of the near field. Such rate in engineered electromagnetic surroundings can greatly exceed that in a homogeneous dielectric environment, or "free space", and the ratio of the two constitutes a figure of merit known as Purcell factor. In contrast to resonant structures like cavities or single metallic/dielectric interfaces, HMMs exhibit a Purcell factor that is broadband and tunable in frequency. However, emitters dispersed on top of them experience a sharply

asymmetrical PDOS, which limits their coupling to the plasmonic modes, and hence the maximum Purcell factor attainable.

In this chapter we optimize the SE enhancement of a point source by including it inside a ML silver (Ag) / silicon (Si) HMM (Fig. 3.1(a)). We start in Section 3.2 by addressing the problem of a point dipole, representing the emitter, placed outside the Ag/Si ML; we calculate the Purcell factor with an analytical model, and use the latter to validate 3D full-wave simulations of the same configuration, obtaining coherent results. After fixing the ML filling ratio, in Section 3.3 we study the evolution of the Purcell factor as the dipole is embedded within the first five Si layers. Once the optimum configuration is determined, in Section 3.4 two different kinds of 1D grating, triangular and rectangular, are patterned in the ML (Figs. 3.1(b) and 3.1(c)) to outcouple the plasmonic SE components into the far field. In Section 3.5 we summarize the work done and make final remarks.

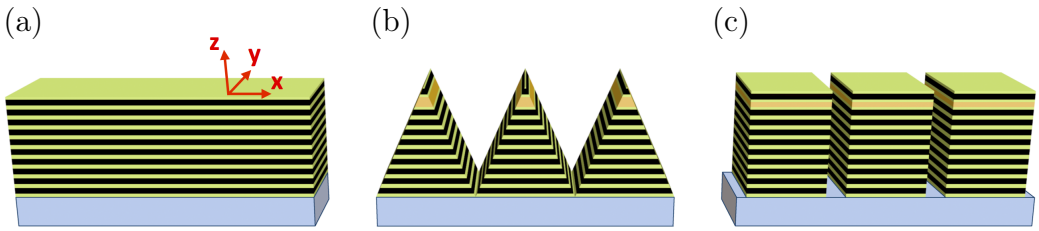

Figure 3.1: (a) Uniform Ag/Si ML, (b) triangular and (c) rectangular grating.

3.2 Emitter outside a uniform Si/Ag ML

We begin our analysis by introducing a model, based on the work of Ford and Weber [144], to compute the SE enhancement of a point source above a uniform (i.e. not patterned) ML. The Purcell factors $F_{\parallel}$ and $F_{\perp}$ of a dipole oriented respectively parallel ($\parallel$, "p-polarization") or orthogonal ($\perp$, "s-polarization") to the layers and located a distance

d above the surface are given by:

$$F_{\parallel} = 1 - \eta_0 \left(1 - \frac{3}{4}\,\mathrm{Re}\int_0^{\infty} dk_{\parallel}\, D_{\parallel}(k_{\parallel})\right), \tag{3.1}$$

$$F_{\perp} = 1 - \eta_0 \left(1 - \frac{3}{2}\,\mathrm{Re}\int_0^{\infty} dk_{\parallel}\, D_{\perp}(k_{\parallel})\right), \tag{3.2}$$

where the power density spectra $D_{\parallel}(k_{\parallel})$ and $D_{\perp}(k_{\parallel})$ are defined as:

$$D_{\parallel} = \frac{1}{k_z}\frac{k_{\parallel}}{\sqrt{\varepsilon_1}k_0}\left[1 + r_S\, e^{2ik_z d} + \left(\frac{k_z}{\sqrt{\varepsilon_1}k_0}\right)^2 \left(1 - r_P\, e^{2ik_z d}\right)\right], \tag{3.3}$$

$$D_{\perp} = \frac{1}{k_z}\left(\frac{k_{\parallel}}{\sqrt{\varepsilon_1}k_0}\right)^3 \left(1 + r_P\, e^{2ik_z d}\right). \tag{3.4}$$

In the formulae above, η_0 denotes the internal quantum efficiency of the dipole in a free space with real permittivity ε_1 (and is assumed to be unity in our calculations), $k_0 = 2\pi/\lambda_0$ is the magnitude of the wavevector in vacuum at wavelength λ_0, $k_{\parallel} = \sqrt{k_x^2 + k_y^2}$ and $k_z = \sqrt{\varepsilon_1 k_0^2 - k_{\parallel}^2}$ are the wavevector components along the in-plane and vertical directions respectively, and r_P, r_S represent the amplitude reflection coefficients of the ML for a P- (TM) or S- (TE) polarized plane wave (not to be confused with the dipole polarization), retrieved with a transfer matrix method (TMM) [204]. Dipoles occurring in nature are isotropic [24]; therefore a more appropriate Purcell factor F_{iso} is obtained through an average over $F_{\parallel}$ and $F_{\perp}$:

$$F_{iso} = \frac{1}{3}\left(F_{\perp} + 2F_{\parallel}\right), \tag{3.5}$$

where the factor 2 accounts for the two equivalent orthogonal in-plane orientations.

We consider a ML composed of 10 Ag/Si periods, each 20 nm thick; the uppermost Ag layer is capped by a 5 nm Si "matching layer", and the entire structure is sandwiched between two semi-infinite glass regions. A dipole with p- or s- polarization is placed 10 nm above the Si "matching layer", the purpose of which is to ensure the correct plasmonic coupling at the first interface (Si-Ag, and not glass-Ag). The permittivity of glass is taken to be $\varepsilon_1 = 2.25$, whereas those of Ag and Si are extracted respectively from [205] and [206]. Fig. 3.2(a) illustrates the tunability properties of the ML, computed with Matlab. When the metal filling ratio ρ of a period is decreased from 100%, the Purcell peak is broadened by the higher number of plasmonic modes made available to the emitter. Such modes originate from the hybridization of the resonances associated to individual Ag/Si interfaces, as the latter are brought together in a ML, very much like the case of electrons or phonons in solids, or dielectric slabs in photonic crystals. In the power density spectra of Figs. 3.2(b) – 3.2(d) we observe distinctly the transition between two limit behaviors: a single metallic interface (volume fraction $\rho = 1$) supports only one resonance (Fig. 3.2(b)); on the other hand, minimizing the percentage of metal in a period (Figs. 3.2(c) and 3.2(d)) reduces each Ag layer to a thin film sandwiched between two thick Si slabs. Accordingly, the modes tend to group and merge into the even and odd branches manifested by an insulator-metal-insulator (IMI) geometry [5, 207]. We also notice that, irrespective of the filling ratio, all the modes converge to the single interface resonance ($\lambda_0 = 360$ nm for Ag/glass, Fig. 3.2(b), and $\lambda_0 = 594$ nm for Ag/Si, Figs. 3.2(c) and 3.2(d)); as a consequence of the mode separation discussed above, the convergence is faster for large filling ratios, while it happens at higher wavevectors for the small ones.

In view of the extension of our study to the inside of the ML, we perform 3D full-

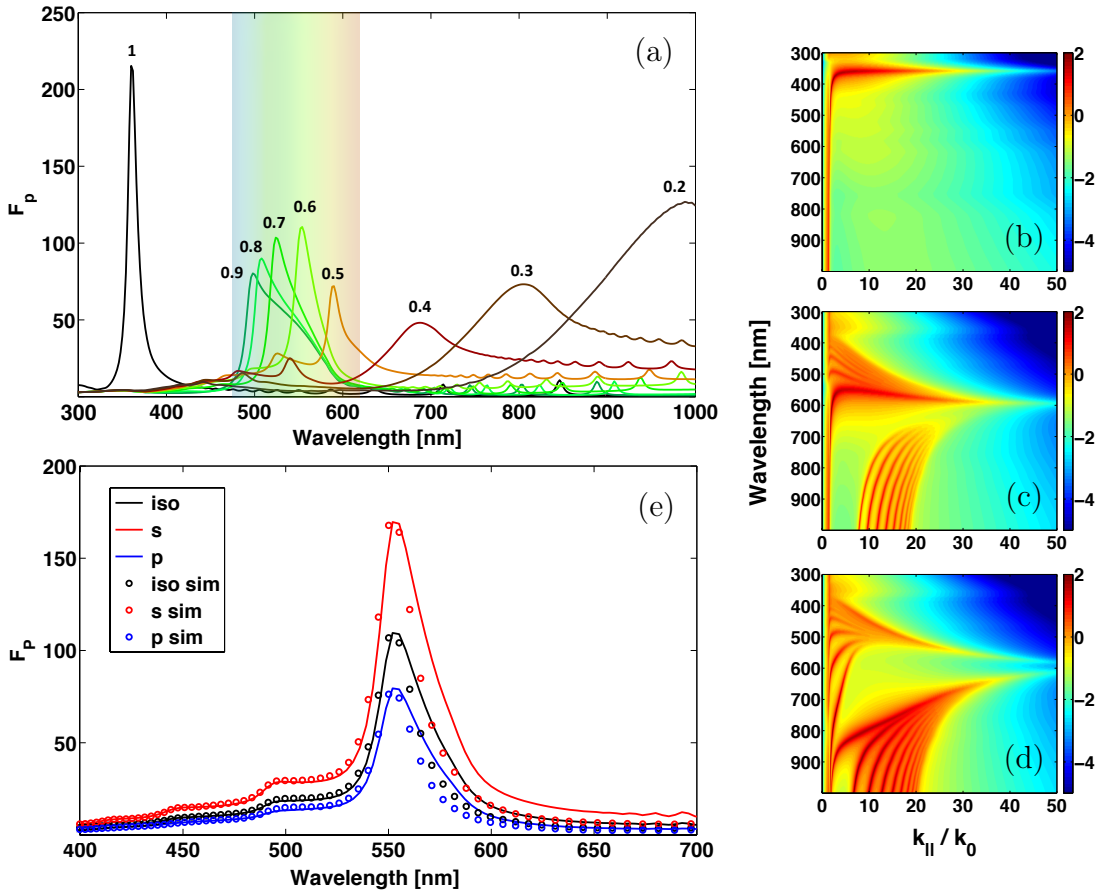

Figure 3.2: (a) Purcell factor F_P for an isotropic dipole in glass 10 nm above the Si/Ag uniform ML. The Ag volume fraction ρ is varied from 1 (in which case the Si capping layer is excluded) to 0.2, as indicated above each curve. The tunability is finer in the yellow-green region of the visible range, highlighted by the colored background. (b) Power density spectrum (logarithmic scale) of an s- dipole for $\rho = 1$, (c) 0.6 and (d) 0.3. (e) Comparison between the Purcell factors of an s-, p- and isotropic dipole with $\rho = 0.6$, obtained with analytical calculations (continuous curves) and FEM simulations (open circles).

wave FEM simulations on a cluster with the commercial software Comsol Multiphysics. We reproduce the configuration adopted in the analytical calculations using the same geometric and material parameters, and evaluate the Purcell factor as:

$$F_{\parallel,\perp} = \frac{P_{\parallel,\perp}{}^{ML}}{P^0} = \frac{P_{\parallel,\perp}{}^{r} + P_{\parallel,\perp}{}^{nr}}{P^0}, \tag{3.6}$$

where ${P_\parallel}^{ML}$ (${P_\perp}^{ML}$) is the total power emitted by a parallel (orthogonal) electric point dipole 10 nm above the ML, sum of the power ${P_\parallel}^{r}$ (${P_\perp}^{r}$) radiated into the far field and the power ${P_\parallel}^{nr}$ (${P_\perp}^{nr}$) dissipated into the structure; P^0 is the total power emitted by the dipole in free space. The isotropic source behavior is again mimicked as in Eq. (3.5).

We choose to focus on the $\rho = 0.6$ filling ratio, corresponding to 12 nm of Ag and 8 nm of Si, which yields the highest Purcell factor (110-fold enhancement at $\lambda_0 = 554$ nm) in the visible range. Fig. 3.2(e) shows a good agreement between analytical and FEM results, so that hereafter we will confidently carry out our investigation by means of 3D simulations.

3.3 Emitter inside a uniform Si/Ag ML

The transition of the source to the center of the Si layers, as depicted in Fig. 3.3(a), strengthens and enriches the spectral response of the ML, calculated for a parallel, orthogonal and isotropic dipole (Figs. 3.3(b) – 3.3(d)). First, the maximum Purcell factor is enhanced up to 3-fold (at $\lambda_0 = 554$ nm) with respect to its value outside the structure, since the emitter now interacts with two high-PDOS regions rather than just one. Including the source in the middle of the Si films makes the host medium coincide with the non-metallic constituent of the ML. This eliminates the need for the "matching layer" discussed in Section 3.2 and promotes a more efficient coupling, as the distance between the emitter and the first accessible Si/Ag interfaces is reduced. Second, the Purcell factors related to Position 1 in Figs. 3.3(b) and 3.3(c) do not discriminate the orientation of the dipole except for a different peak intensity [145], observed in proportion also in the other positions. The SE enhancement of an internal emitter manifests instead a polarization-dependent spectral signature, which can be explained with a simple symmetry argument.

When a p-dipole is embedded in the middle of a Si layer, its electric field com-

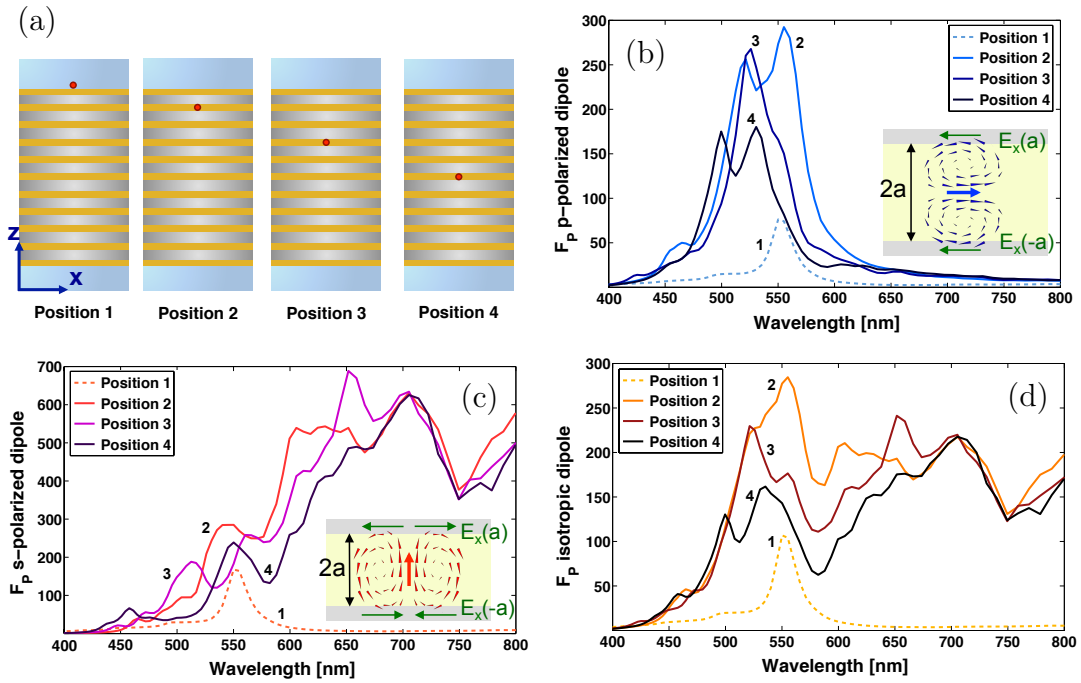

Figure 3.3: (a) Positioning of a dipole (indicated by a red dot) outside and inside selected Si layers (ochre stripes) of the uniform ML. (b) Purcell factor F_P of a parallel or (c) orthogonal dipole for the outer (dashed line) and inner positions (solid lines). The insets show the coupling of the dipole field, directed from the tail to the tip of the triangles and proportional in magnitude to their size, to the Ag (grey)/Si (yellow) interfaces. (d) Purcell factor of an isotropic emitter for the positions considered in (b) and (c).

ponents along the opposing Ag/Si interfaces (green arrows in the inset of Fig. 3.3(b)) possess inversion and mirror-image symmetry; an s-dipole still exhibits the former, but its mirror image is antisymmetric (inset of Fig. 3.3(c)). Therefore, a parallel polarization excites the odd modes lying at shorter wavelengths than the Ag/Si resonance, while a perpendicular polarization activates both the odd and the even ones, the latter resulting more pronounced. The isotropic response of Fig. 3.3(d) originates from the weighted overlap of these purely symmetric and hybrid contributions.

3.4 Emitter inside a 1D-nanopatterned Si/Ag ML

In order to scatter the plasmonic modes into the far field [5], we design a 1D grating, with either triangular or rectangular profile as sketched in Figs. 3.1(b) and 3.1(c). We quantify the far field radiative enhancement as:

$$RE(\theta) = \frac{P_{\uparrow}{}^{r}(\theta)}{P_{\uparrow}{}^{0}(\theta)}, \tag{3.7}$$

where $P_{\uparrow}{}^{r}(\theta)$ and $P_{\uparrow}{}^{0}(\theta)$ are the powers emitted by a dipole respectively inside the ML and in free space into a cone with vertex in the emitter, axis oriented as the positive z direction and half-angle θ. The presence of the grating breaks the in-plane symmetry of the uniform ML, so that both the Purcell factor and the radiative enhancement of an isotropic source are retrieved through an average over the three Cartesian polarizations:

$$F_{iso} = \frac{1}{3}\left(F_x + F_y + F_z\right), \qquad RE_{iso} = \frac{1}{3}\left(RE_x + RE_y + RE_z\right). \tag{3.8}$$

We fix the dipole in Position 2, and set the emitting layer and the outer region material to polymethyl methacrylate (PMMA). The first replacement introduces an alternative host to Si that is easier to dope with emitters active at the considered frequencies; the second makes optically homogeneous all the volume unoccupied by the ML, so that any changes in the directionality and intensity of radiation with respect to free space can be attributed exclusively to the outcoupling structures. Accordingly, we add above and below the emitting region two 5 nm Si "matching layers", in contact respectively with 1 and 9 periods with $\rho = 0.6$.

We implement a triangular grating with a pitch of 300 nm, and a rectangular grating with a pitch of 200 nm and a slit width of 40 nm. After optimizing the compu-

tational and geometric parameters, the emitting region thickness is set to 20 nm for the first structure, and to 10 nm for the second. A dipole centered in the emitting layer of an individual grating period experiences the Purcell factors displayed in Fig. 3.4(a). The response of the triangular grating with a 20 nm PMMA layer (blue curve) is similar to that of a uniform ML with an emitting region of identical thickness (red curve), which demonstrates the weak effect of nanopatterning on the SE enhancement. The radiative enhancements induced by the gratings (Figs. 3.4(b) and 3.4(c)) are both red-shifted, and extend over a slightly wider region than the Purcell peak of Fig. 3.4(a); we observe the highest displacement and spread in the rectangular structure. They also increase as the collection angle θ is decreased, with a gradient dictated by the grating geometry. The triangular nanopattern allows a maximum radiative enhancement of about 10 at $\lambda_0 = 576$ nm and $\theta = 35°$, while the rectangular one reaches almost a 6-fold enhancement at $\lambda_0 = 582$ nm and $\theta = 35°$.

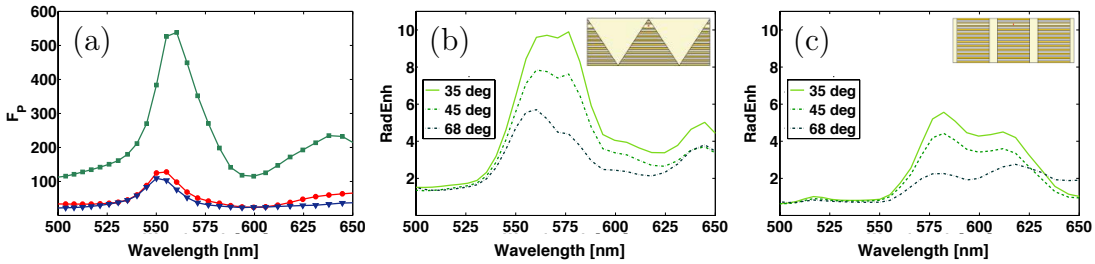

Figure 3.4: (a) Isotropic Purcell factor for the triangular grating (blue curve, triangular markers), the rectangular grating (green curve, square markers) and an unpatterned structure with an emitting layer of 20 nm (red curve, circular markers). (b) Radiative enhancement at different angles for an isotropic dipole, provided by the triangular grating, and (c) by the rectangular grating, sketched in the insets.

3.5 Conclusions

We investigated the SE enhancement of a point source as a function of its position inside a HMM, consisting of a 10 period Ag/Si ML. We first tuned via filling ratio the

Purcell factor over the visible spectrum, and explained how plasmonic modes arise from the hybridization of the individual Ag/Si interfaces. Next, we introduced the emitter in the inner semiconducting layers, and observed that the Purcell spectral response derives from the orientation-selective coupling of the dipole with the modes. The isotropic SE enhancement inside the ML reaches a maximum of almost 300-fold, 3 times larger than its peak value for an external emitter. Finally, we proposed two 1D gratings to extract into the far field the plasmonic components of the emission spectrum, obtaining a radiative enhancement as high as 10-fold.

The present work devised a novel method to enhance the Purcell factor in HMMs, utilizing a standard grating approach to extract into the far field the plasmonic SE components. In the following two chapters, our attention shifts from the Purcell factor to the radiative enhancement, with the goal of introducing new extraction mechanisms capable of directional control. The grating is replaced with a nanoantenna in Chapter 4, while a patternless approach is explored in Chapter 5.

Chapter 3, in part, is a reprint of the material as it appears on Optics Express 22, 4301–4306 (2014). L. Ferrari, D. Lu, D. Lepage, Z. Liu, “Enhanced spontaneous emission inside hyperbolic metamaterials”. The dissertation author is the first author of this paper.

Chapter 4

Light extraction from HMMs: shape engineering

4.1 Introduction

In the previous chapter we saw how moving a quantum emitter from the outside to the inside of a HMM increases the Purcell factor, since a larger PDOS becomes available. From a technology perspective, a larger Purcell factor corresponds to a larger modulation bandwidth: therefore, its enhancement is key for the implementation of fast hyperbolic transmitters into optical communication systems. The practical exploitation of such high-speed potential, however, faces two major challenges. Firstly, the discontinuous decrease in PDOS from HMMs to their surrounding environment implies that their interface with air suffers a remarkable impedance mismatch. As a consequence, large-k waves remain trapped inside hyperbolic media, unless a suitable mechanism is provided that mediates the HMM-to-air transition. The traditional solution described in the literature consists of milling through or depositing on top of the HMM a sub-wavelength grating, whose periodicity provides the matching k-vector required by momentum conservation

[18, 19, 154, 208, 209, 210]. Secondly, it is not trivial to shape the emission pattern of the light outcoupled from HMMs. Directional control of emission is beneficial for applications such as on-chip photonics, where light must be routed to different in-plane directions or switched in-plane and out-of-plane with respect to the chip surface, and fiber-optic communication, where the optical signal must be effectively channeled into the numerical aperture of a multi-mode or single-mode fiber.

An approach that addresses both challenges consists in replacing a grating with a nanoantenna, whose SE enhancement properties are well known and utilized in the world of plasmonics [22, 23, 24]. In contrast to gratings, which exploit periodicity to extract large-k waves, nanoantennas leverage resonant light-matter coupling. The strong localization of the electromagnetic field granted by antenna structures boosts their interaction with quantum emitters, and distributes the outcoupled radiation into defined emission patterns.

In this chapter we study the properties of a cylindrical hyperbolic nanoantenna, based on a Ag/Si ML HMM. We first discuss how the Purcell factor and the radiative enhancement of a dipolar emitter are affected by its coupling with the antenna. By means of spatial mapping, we determine the dipole positioning that maximizes either quantity for each Cartesian dipole orientation, and propose a combined figure of merit to evaluate the antenna performance. We then observe how directional emission from the antenna can be wavelength-tuned in a limited spectral range and for a determined dipole orientation. We finally demonstrate a feasible fabrication method for high quality ML cylindrical nanoantennas, and discuss how these structures can be experimentally coupled to quantum emitters.

4.2 Spatial mapping of Purcell factor and radiative enhancement

We observed in Chapter 3 how the peak Purcell factor of a dipole 10 nm above a flat Ag/Si ML could be tuned in wavelength by changing the filling ratio ρ. At $\rho = 0.5$, the Purcell factor of a dipole in air reaches its maximum at $\lambda_0 = 584$ nm. Among all filling ratios, $\rho = 0.5$ is the only one at which the Si/Ag ML effective medium retains a fully hyperbolic character over the entire visible spectrum, without undergoing any topological transitions [43] to effective elliptic, dielectric or metallic states (Fig. 4.1). The Purcell factor peak is achieved in the Type I region of the HMM dispersion, slightly before the transition to Type II at $\lambda_{trans} = 594$ nm.

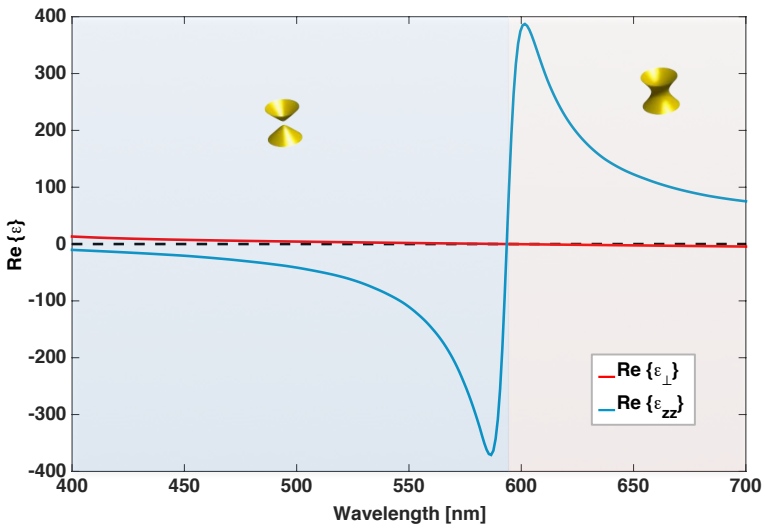

Figure 4.1: Effective permittivity components of a Si/Ag ML HMM with filling ratio $\rho = 0.5$. Across $\lambda_{trans} = 594$ nm, the effective medium dispersion turns from Type I (two-fold hyperboloid) into Type II (one-fold hyperboloid).

We now fix the wavelength to $\lambda_0 = 584$ nm, and study the spatial distribution of the Purcell factor and of the radiative enhancement of a cylindrical hyperbolic nanoantenna, made of Si/Ag ML effective medium with filling ratio $\rho = 0.5$ (Fig. 4.2). By means

of 3D FEM simulations (Comsol), we compute the Purcell factor for each Cartesian dipole orientation according to Eq. (3.6). Similarly to Eq. (3.7), we compute the radiative

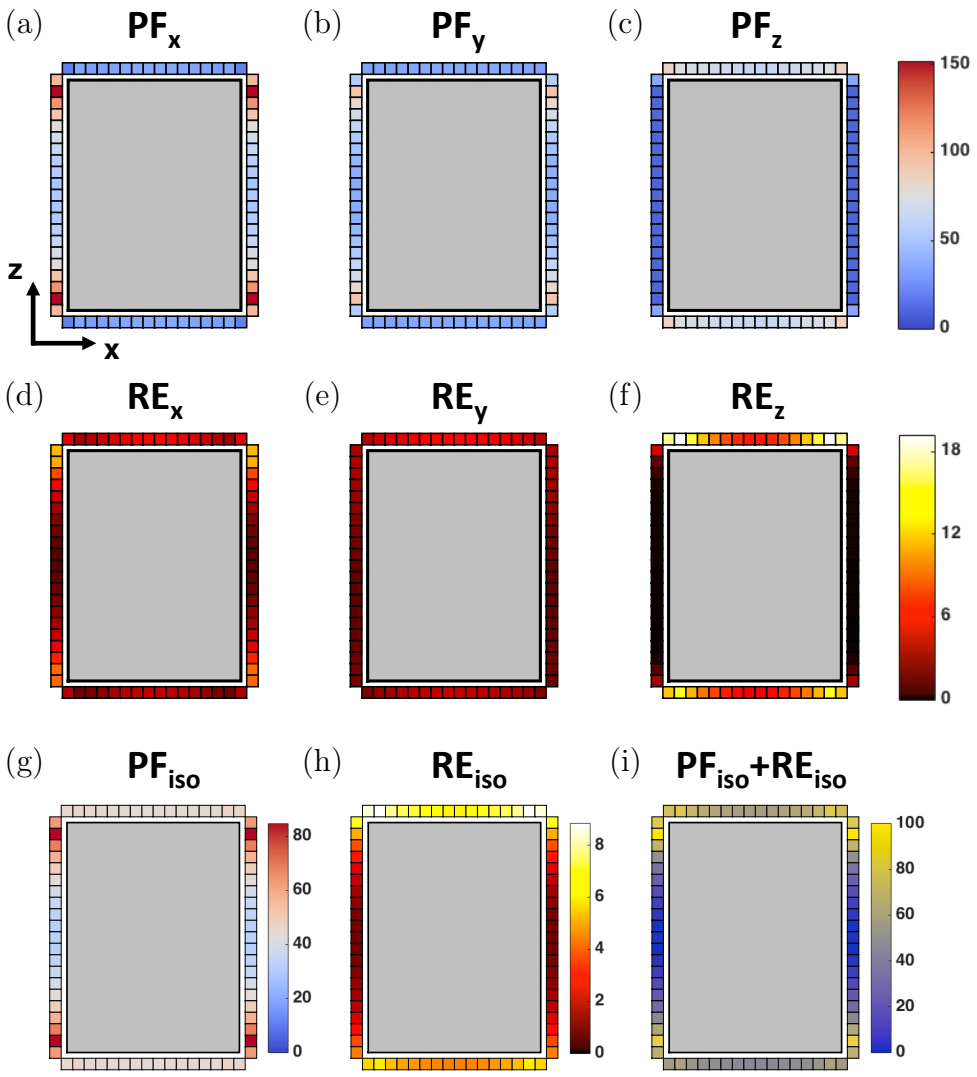

Figure 4.2: Spatial mapping at $\lambda_0 = 584$ nm of the Purcell factor and the radiative enhancement of the cylindrical hyperbolic nanoantenna. The effective parameters of the structure correspond to a Ag/Si ML HMM with filling ratio $\rho = 0.5$. The dipole position is varied in the *xz* plane, bisecting the antenna, keeping a distance of 10 nm from the structure. (a) Purcell factor of an X-, (b) Y- and (c) Z-dipole. (d) Radiative enhancement of an X-, (e) Y- and (f) Z-dipole. (g) Purcell factor and (h) radiative enhancement of an isotropic dipole. (i) Total SE enhancement, representing the balanced optimization of the nanoantenna performance, when Purcell factor and radiative enhancement are equally weighted.

enhancement as the ratio between the power emitted by a dipole respectively coupled to the antenna and in free space into the upper semispace. The isotropic quantities are retrieved with an average over the three Cartesian dipole orientations. The antenna height of 200 nm corresponds to the thickness of a Si/Ag ML with 10 periods of 20 nm, like the one considered in Chapter 3, that can be grown with high quality via sputtering [18]. The diameter of 150 nm generates, at $\lambda_0 = 584$ nm, a resonant mode (whose profile is shown in Fig. 4.3) that maximizes radiative outcoupling for dipoles located on top of or underneath the antenna (Figs. 4.2(d)–(f) and (h)). As opposed to emitter locations along the lateral walls, this positioning offers a better accessibility in terms of nanofabrication, as we will discuss in Section 4.4.

We perform a spatial mapping of the dipole-antenna coupling by varying the dipole position around the antenna in steps of 10 nm, and keeping a fixed dipole-antenna distance of 10 nm. The Purcell factor is maximized by a dipole orientation along the x axis ("X-dipole", Fig. 4.2(a)), while the largest radiative enhancement is achieved by a Z-dipole (Fig. 4.2(f)). The averaged response of an isotropic dipole (Figs. 4.2(g) and (h)) shows that, both for the Purcell factor and for the radiative enhancement, the maximum is localized close to the edges, and dipole locations above and below the antenna are favored over lateral locations. As discussed earlier, the simultaneous evaluation of Purcell factor and radiative enhancement is mandatory when optimizing a nanostructure for SE enhancement, because a speed increase alone does not guarantee effective large-k extraction. However, a point-to-point comparison of their spatial distribution is tedious, and fails to quickly identify the best dipole locations and global trends. To overcome this issue, we combine these two related quantities in the "Total SE enhancement" plotted in Fig. 4.2(i). This figure of merit is obtained for each spatial location by normalizing the Purcell factor and radiative enhancement values to their respective maxima, and then adding them up with an arbitrary weight factor, that depends on their significance for

the target application. If for instance speed plays a major role, the Purcell factor can be assigned a larger weight, whereas the opposite can be done if intensity is a more critical requirement. The obtained values are finally mapped to a scale from 0 to 100. In Fig. 4.2(i) we equally weighted speed and intensity; the spatial map suggests that the best dipole position is close to the top surface of the nanoantenna, along the lateral wall. The modal field distribution of the antenna resonance, excited by an X-dipole in such position, is plotted in Fig. 4.3.

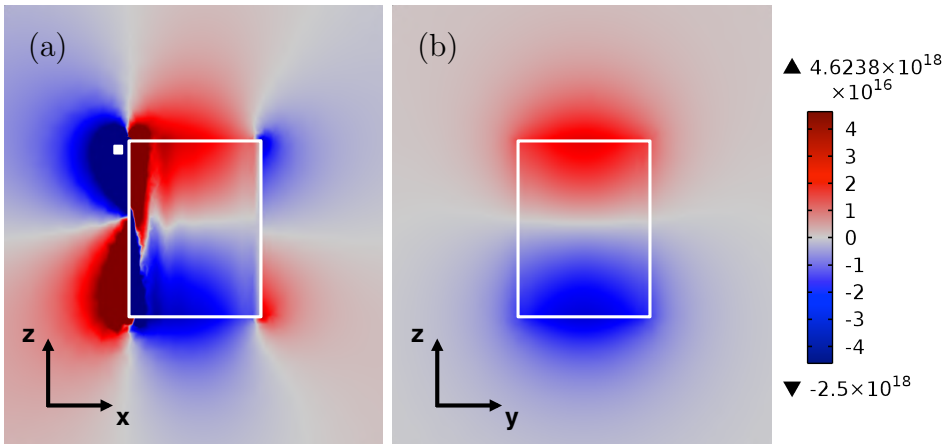

Figure 4.3: Electric field component E_x at $\lambda_0 = 584$ nm of an X-dipole (whose position is indicated by a white square) coupled to the hyperbolic nanoantenna (white bordered rectangle), (a) in the *xz* and (b) in the *yz* plane.

4.3 Directional properties

In addition to enhancing light-matter interaction by strongly localizing the electromagnetic field, antennas can also tailor the emission pattern, channeling radiation into preferential directions. With the intent to explore the directional properties of the hyperbolic nanoantenna, we fix an X-dipole in the position where the total SE enhancement at λ_0 is maximum, and we vary its emission wavelength in the 400-700 nm spectral region. The radiation pattern is in general a complex shape, which does not privilege

one angle over the others. At $\lambda_a = 490$ nm, however, the antenna produces in the xz plane a directional pattern pointing toward the lower semispace, about 20° off its axis (Fig. 4.4(a)). If the wavelength is continuously increased, the pattern preserves its unidirectional character, but rotates clockwise, until at $\lambda_c = 560$ nm it becomes almost perpendicular to the antenna axis. This angular chromatic dispersion, which distributes a 70 nm bandwidth over a $\sim 70°$ angular range, is preserved if the effective medium is replaced with a Ag/Si ML, aside for a slight anticlockwise shift of the angular interval (Fig. 4.4(b)). The origin of such color-switched directionality can be traced to the hybridization of broadband multipolar electric and magnetic resonances within the antenna [211]. A design based on a generalized Kerker condition [212] can harness the rich morphology of the hyperbolic modes [213] and their unique scaling law [182, 65], yielding directionally controlled hyperbolic nanoantennas with applications not only in high-speed light emission and detection, but also in wavelength-selective demultiplexing [211, 214] and higher harmonics generation and manipulation [215, 216].

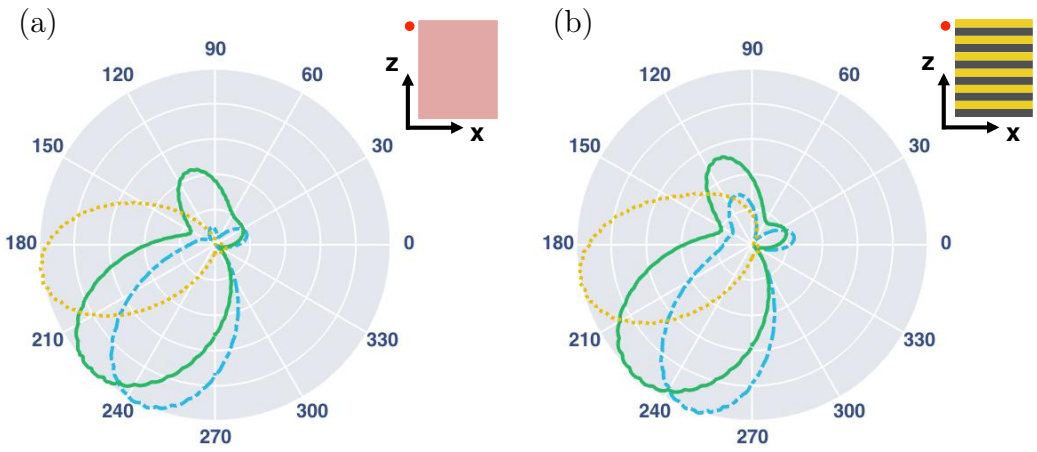

Figure 4.4: (a) Emission pattern (Poynting vector) in the xz plane for an X-dipole coupled with an antenna of effective medium (red dot and pink rectangle in the inset, respectively) at the wavelengths $\lambda_a = 490$ nm (blue dash-dotted line), $\lambda_b = 520$ nm (green solid line) and $\lambda_c = 560$ nm (yellow dotted line). (b) Same patterns as in (a) for an X-dipole coupled with a ML antenna, consisting of 10 Ag/Si periods of 20 nm with filling ratio $\rho = 0.5$. All the curves are normalized to their maxima.

4.4 Hyperbolic nanoantenna fabrication

As discussed in the previous sections, a cylindrical nanoantenna based on a ML hyperbolic medium is a powerful tool to manipulate light-matter interaction. Its fabrication, however, is not straightforward, for two fundamental reasons. First, the different nature of the two ML components, respectively dielectric/semiconducting and metallic, requires the development of an etching process that affects both in equal manner, to ensure a satisfactory wall quality. It is for instance problematic to pattern cylinders on a ML film with a process based on etching mask definition, via e-beam lithography, followed by reactive ion etching: for a given etching gas, the metal:dielectric selectivity is usually different than 1, resulting in dishomogeneous etching of the walls and damage at the interface of the layers. Alternatively, the ML can be grown inside a mask previously defined with e-beam lithography [65]: in this case, the antenna quality is limited by the quality of liftoff. Another inherent fabrication challenge comes from the maximum number of periods achievable. On the one hand, the more periods a ML features, the closer it gets to an ideal hyperbolic medium; but the thicker the ML grows, the harder it is to shape it with aspect ratios larger than 1:1. Cylindrical hyperbolic nanoantenna designs have been evoked [213, 217], but never demonstrated experimentally. A square hyperbolic cavity of 20 nm Ag/30 nm Ge was demonstrated in [65], but with only 3 periods and with a taper angle of 25°.

To fabricate the nanoantenna described in this chapter, we first grow via sputtering deposition (AJA Orion; Ag rate = 0.76 Å / s at 50 W DC and 2 mTorr, Si rate = 0.16 Å / s at 100 W RF and 2 mTorr) a 200 nm Ag/Si ML, consisting of 10 periods with filling ratio $\rho = 0.5$ and thickness 20 nm, on a Si substrate. We then pattern a cylinder of diameter 150 nm with a two-step focused ion beam process. A fast, rough cut (voltage=30 kV, current=50 pA) defines a diameter of 500 nm; a slow, fine cut (voltage=30 kV, current=1.5

pA) delicately thins the diameter to the target value. The use of the rough cut alone severely damages the ML, by removing some of the topmost periods; the fine cut alone takes an excessively long time to complete. Fig. 4.5 shows the fabricated nanoantenna. The inevitable tapering of the structure can be minimized by optimizing the dwell time: the 10° taper of the reported antenna was obtained with a dwell time of 200 µs. Shrinking the antenna diameter yields an increased taper.

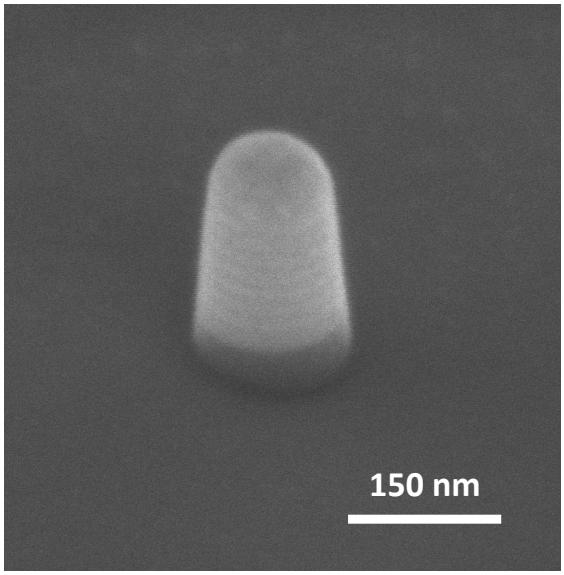

Figure 4.5: SEM image of a HMM cylindrical nanoantenna. The structure consists of 10 periods of 10 nm Ag (bright layers) / 10 nm Si (dark layers) and has a diameter at the base of 150 nm. The FIB cut etched partly through the Si substrate (dark post below the antenna), and caused a 10° taper of the antenna walls.

The positioning of emitters in the near field of the antenna represents a significant nanofabrication challenge. The study of Section 4.2 suggests that, at $\lambda_0 =$ 584 nm, quantum sources on top of the antenna exhibit the largest Purcell factor and radiative enhancement. To test this prediction, we synthesize trioctylphosphine (TOP)-capped (CdSe)ZnS core/shell colloidal quantum dots with peak emission $\lambda_{QD} =$ 580 nm. The topmost Si layer of the as-grown Si/Ag ML is functionalized with (3-mercaptopropyl)trimethoxysilane (MPTMS), to promote QD adhesion. After incubation for 12 hours in a QD solution, the ML results coated by few (1 to 3) monolayers of

QDs. Once the emitters are bound to the ML surface, we define the nanoantenna with the two-step FIB process described above. While a good photoluminescence (PL) signal is observed from the unpatterned QD-ML system, a PL raster scan in the antenna area yields no detectable signal. We infer that the FIB cut somehow ablated or damaged the thin QD layers on the cylinder tip, quenching their emission. Therefore, the proposed antenna fabrication strategy requires a safer emitter integration. An option consists in growing the ML on top of a semiconductor quantum well tuned to the desired emission wavelength. The QW-ML distance can be controlled down to few tens of nm, ensuring a proper hyperbolic coupling; the FIB cut does not affect the integrity of the emitting area, protected by the antenna. In addition, in this study we only considered emitter locations external to the hyperbolic structure. The inclusion within the ML of 1D (QDs, fluorescent metallic clusters) or 2D (metallic QWs) emitters can preserve their integrity during the FIB cut.

4.5 Conclusions

In this chapter we explored the use of a cylindrical nanoantenna as a means to enhance light extraction from hyperbolic media. We first analyzed the spatial distribution at $\lambda_0 = 584$ nm of the Purcell factor and the radiative enhancement of a point dipole coupled to the antenna, represented by a cylinder of effective medium with thickness 200 nm and diameter 150 nm. The effective parameters of the antenna correspond to a Ag/Si ML with filling ratio $\rho = 0.5$. By means of a new figure of merit, introduced to combine the speed and intensity behavior into a single parameter, we determined the best dipole positioning, and observed that dipole locations above and underneath the antenna outperform lateral ones. An analysis of the radiation patterns revealed that the emission of an X-dipole coupled to the antenna can be channeled into a preferential direction in the

wavelength range 490-560 nm. As the wavelength is continuously increased within such interval, the angle of maximum emission accordingly increases, covering a corresponding angular range of $\sim 70^{\circ}$. We finally fabricated the antenna with a two-step FIB process, and discussed its effective coupling with different categories of quantum emitters.

Future work will explore the emitter implementations proposed in Section 4.4, alternative to QDs. Besides, the nanoantenna properties discussed in the present chapter can only be tuned at the fabrication stage by changing the HMM filling ratio. The introduction inside a ML of one or more ferromagnetic layers (e.g. of iron oxide) will enable a dynamic control of the antenna, mediated by magnetoplasmonic interactions [218], by means of an externally applied magnetic field.

Chapter 4, in part, has been submitted for publication. L. Ferrari, J. S. T. Smalley, Y. Fainman and Z. Liu, “Hyperbolic metamaterials for dispersion-assisted directional light emission”. The dissertation author is the first author of this paper.

Chapter 5

Light extraction from HMMs: dispersion engineering

5.1 Introduction

The SE enhancement provided by HMMs can be fully leveraged in optical communications only if the large-k waves that prompt it are suitably outcoupled into the far field. We have seen that this goal can be achieved by means of either a grating (Chapter 3) or a nanoantenna (Chapter 4). In comparison to the former, the latter provides directional radiation control in addition to large wavevector extraction. Both nanostructures however present a critical challenge from a manufacturing standpoint. Adding a sub-wavelength feature typically means extra time and cost in fabrication: gratings and nanoantennas are defined via focused ion-beam [18] or electron-beam lithography [208, 209], which are not economically sustainable for mass production because of their limited throughput. Furthermore, the optimum nanostructure geometry determined via analytical or numerical simulations is often hardly achievable in practice with the above-mentioned techniques. 1D gratings with rectangular cross-section have

not shown good directional control properties [18]; bullseye gratings extract radiation into a conical pattern [209], but it is not clearly understood how to control and shape the emission pattern arbitrarily via design parameters. A common issue to all grating and nanoantenna types is that the extraction efficiency and the directional control depend on the relative emitter-grating position: for instance, a quantum light source contained in a horizontal plane below the grating displays a different behavior whether it is located adjacent to a crest or to a trough [18]. As a consequence, the outcoupling performance of the grating and the antenna is not univocally determined, but results from an average over the spatial distribution of the emitters.

In this chapter we propose a novel paradigm based on dispersion engineering to outcouple large-k waves from HMMs. With a suitable selection of the HMM filling ratio, we extract high k-vectors into the far field by compressing their component parallel or perpendicular to the HMM optical axis, thereby enhancing the overall power routed along the corresponding Cartesian direction (Fig. 5.1). By lifting the requirement for a grating, our approach makes the fabrication of fast optical transmitters based on quantum emitter-HMM coupling more practical and versatile. The extraction mechanism relies on the bulk properties of the HMM, rather than on spatially varying features of a superimposed structure: as such, it affects equally all the emitters contained in the same plane parallel or orthogonal to the optical axis. This enables the effective channeling of emission from a QW, which for practical purposes can be thought of as a plane of quantum sources (electron-hole pairs). We first discuss the theory of dispersion-assisted directional outcoupling in the ideal case of zero optical losses, analyzing the four HMM configurations that induce this phenomenon. We then assess two metal/dielectric material systems for ML HMMs in the visible range, and observe how their loss restricts the practically achievable configurations and the band of outcoupled k-vectors. The developed model is finally applied to the study of a colloidal QD-HMM system: by

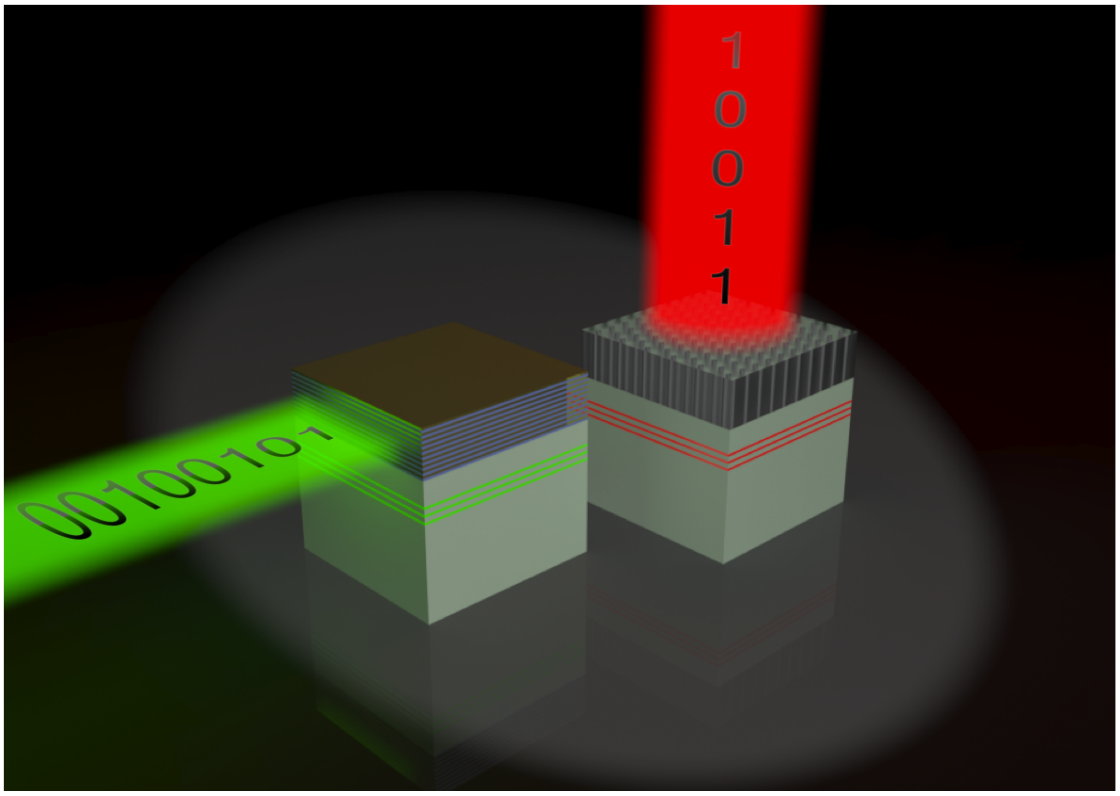

Figure 5.1: Artistic representation of high-speed optical transmission via unpatterned HMMs. Light emitted from a multiple quantum well, depicted by 3 green (left) and red (right) luminescent layers, couples to a ML (left) and a NW (right) HMM block. The hyperbolic dispersions are designed to extract radiation respectively from the side or from the top interface.

means of finite element electromagnetic simulations, we determine how the light emitted from a point dipole (representing the QD) into a block of HMM is outcoupled by the latter into directional far-field radiation, polarized along the optical axis independently of the dipole orientation. HMMs capable of extracting large-k waves by impedance-matching the surrounding dielectric were considered in a recent work by West et al. [219], but for a very specific material system and with minimal mention of dipole-HMM coupling. After evaluating the performance of the QD-HMM system, we conclude our study by suggesting guidelines for its practical implementation and future development.

5.2 Theory of dispersion-assisted directional outcoupling from HMMs

In this section we explain how large-k waves can be directionally extracted from lossless HMMs via a filling ratio optimization procedure. The results presented hold true for any medium with hyperbolic dispersion regardless of how its effective parameters are retrieved, and therefore indistinctly apply to ML and to NW configurations. Since ML HMMs offer a wider constituent materials choice and are more versatile from a fabrication standpoint, we will focus on this category in the subsequent analysis.

5.2.1 Principle of large-k waves outcoupling via dispersion engineering

Recalling Subsection 2.2.1, a hyperbolic medium is described by a uniaxial permittivity tensor of the form:

$$\bar{\bar{\varepsilon}} = \begin{bmatrix} \varepsilon_{\perp} & 0 & 0 \\ 0 & \varepsilon_{\perp} & 0 \\ 0 & 0 & \varepsilon_{zz} \end{bmatrix}, \tag{5.1}$$

in a Cartesian frame of reference $\{\hat{\mathbf{x}},\hat{\mathbf{y}},\hat{\mathbf{z}}\}$ where the unit vector $\hat{\mathbf{z}}$ is parallel to the optical axis. For a periodic ML HMM with layer interfaces orthogonal to $\hat{\mathbf{z}}$, the effective parameters $\varepsilon_{\perp}$ and ε_{zz} are obtained through the homogenization formulae (Subsection 2.2.2):

$$\varepsilon_{\perp}(\omega,\rho) = \rho\varepsilon_m(\omega) + (1-\rho)\varepsilon_d(\omega), \tag{5.2}$$

$$\varepsilon_{zz}(\omega,\rho) = \left(\frac{\rho}{\varepsilon_m(\omega)} + \frac{1-\rho}{\varepsilon_d(\omega)}\right)^{-1}. \tag{5.3}$$

$\varepsilon_m(\omega)$ and $\varepsilon_d(\omega)$ are respectively the permittivities of the metallic and the dielectric layers, which in the absence of spatial dispersion and optical loss depend solely on the angular frequency ω and are real quantities, and $0 < \rho < 1$ is the volumetric filling ratio of metal. The dispersion of the effective medium is hyperbolic only at those frequencies and at those filling ratios at which $\varepsilon_\perp \varepsilon_{zz} < 0$. This requirement classifies the behavior of HMMs into two distinct types:

Type I. When $\varepsilon_\perp(\omega,\rho) > 0$ and $\varepsilon_{zz}(\omega,\rho) < 0$;

Type II. When $\varepsilon_\perp(\omega,\rho) < 0$ and $\varepsilon_{zz}(\omega,\rho) > 0$.

Let us consider the interface, contained in the *xy* plane of the real space, between a nonmagnetic HMM in the $z < 0$ region and a lossless isotropic dielectric medium in the $z > 0$ region. A plane wave with wavevector $\mathbf{k}_{HMM}$ of arbitrary magnitude is subject inside the hyperbolic medium to the dispersion:

$$\left(\frac{k_{HMM,\perp}}{k_0}\right)^2 \frac{1}{\varepsilon_{zz}} + \left(\frac{k_{HMM,z}}{k_0}\right)^2 \frac{1}{\varepsilon_\perp} = 1, \tag{5.4}$$

where, by virtue of the cylindrical symmetry of the permittivity, we introduced the cylindrical coordinate $k_{HMM,\perp} = \sqrt{k_{HMM,x}^2 + k_{HMM,y}^2}$, and $k_0 = \omega/c$ (c = speed of light in vacuum). In the dielectric medium, dispersion takes instead the form

$$\left(\frac{k_{diel,\perp}}{k_0}\right)^2 + \left(\frac{k_{diel,z}}{k_0}\right)^2 = n^2, \tag{5.5}$$

where $k_{diel,\perp} = \sqrt{k_{diel,x}^2 + k_{diel,y}^2}$ and n is the refractive index, and the magnitude of the wavevector $\mathbf{k}_{diel}$ is equal to $k_0 n$. Eq. (5.4) and Eq. (5.5) define respectively a hyperboloid and a sphere in the space of k-vectors at a given frequency $\bar{\omega}$. Their cross-section in the $k_x k_z$ plane is represented in Fig. 5.2(a) for the case of a Type II HMM and air. To simplify the notation and make the discussion clearer, we restrict the following analysis to the $(k_x > 0, k_z > 0)$ quadrant; analogous considerations can be extended by symmetry to the remaining 3 quadrants. We define "large-k waves" those plane waves with k-vector $|\mathbf{k}_{HMM}| > |\mathbf{k}_{air}|$, and "short-$k$ waves" those with k-vector $|\mathbf{k}_{HMM}| \leq |\mathbf{k}_{air}|$. The HMM supports the propagation of large-k waves of components $k_{HMM,x} > k_0 n_{air} = k_0$ and

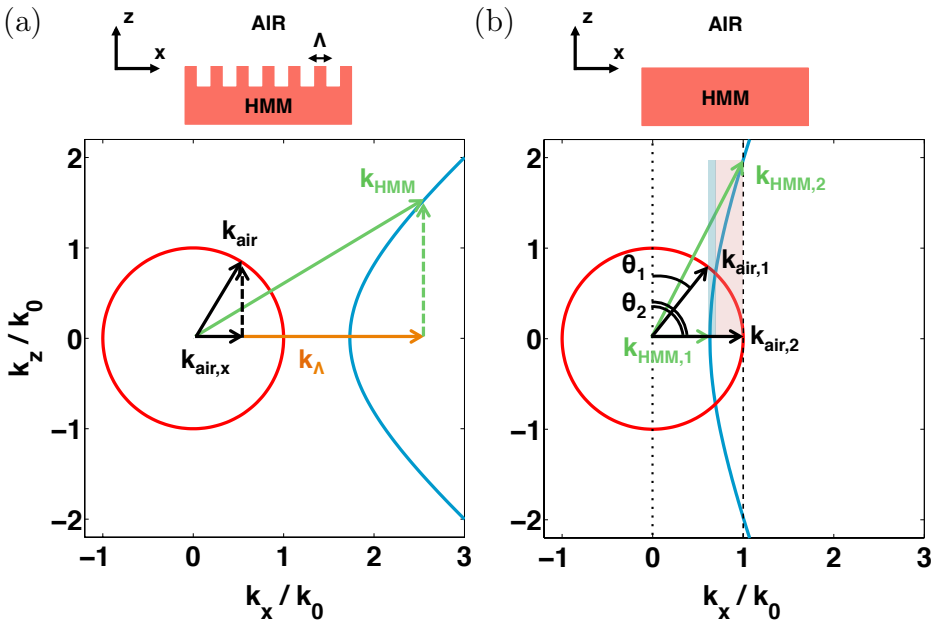

Figure 5.2: Dispersion of Type II HMM (blue hyperbola) showing large k-vector outcoupling upwards into air (red circle) via (a) grating and (b) dispersion engineering. The two configurations are schematically represented above the plots (Λ = grating pitch). For clarity, only the right branch of the HMM dispersion curve is shown, and the normalization by k_0 is omitted in the vector nomenclature. In (b), the portion of outcoupled k-vector band falling within the $(k_x > 0, k_z > 0)$ quadrant is highlighted in light blue (short-k waves) and pink (large-k waves).

$k_{HMM,z} \lessgtr k_0$. When such waves reach the HMM-air boundary, the conservation of the k-vector component parallel to the interface mandates that $k_{air,x} = k_{HMM,x}$. Since $k_{HMM,x} > k_0$, $k_{air,z} = \sqrt{k_0^2 - k_{HMM,x}^2}$ is a purely imaginary number. This turns a propagating wave in the HMM into an evanescent wave in air, preventing its successful outcoupling into the far-field.

Impedance mismatch is traditionally bridged by patterning a grating onto the HMM (inset of Fig. 5.2(a)). A 1D grating with pitch Λ and periodicity along $\hat{\mathbf{x}}$ provides an extra k-vector $\mathbf{k}_\Lambda = k_\Lambda \hat{\mathbf{x}} = (2\pi/\Lambda)\hat{\mathbf{x}}$ [5], outcoupling into air the band of k-vectors with components $k_{HMM,x} > k_0$ such that $k_{HMM,x} = k_\Lambda + k_{air,x}$ is verified for some real $k_{air,x} \leq k_0$. At that point indeed the plane wave becomes propagating in air, as Eq. (5.5) forces its component $k_{air,z}$ to be a real quantity $\leq k_0$.

The same goal can be achieved with the alternative approach schematized in Fig. 5.2(b). If the filling ratio ρ of the HMM is properly designed, the hyperbolic dispersion curve gets "straightened" along the z direction and "squeezed" along the x direction within the circular dispersion of air. In this case, there exists in the HMM a band of k-vectors which possess a conserved component $k_{HMM,x} \leq k_0$, and therefore retain their propagating nature across the HMM-air boundary. The band is delimited by two extremes $\mathbf{k}_{HMM,1}$ and $\mathbf{k}_{HMM,2}$, and contains both short- and large-k waves, separated by a vector $\mathbf{k}_{HMM,sep}$ (not drawn in the figure). $\mathbf{k}_{HMM,1}$, $\mathbf{k}_{HMM,sep}$ and $\mathbf{k}_{HMM,2}$ are defined as the intersections of the hyperbolic dispersion respectively with the x axis, the circular dispersion of air and the straight line $k_x \equiv k_0$. The relative contribution of large-k waves, $(k_{HMM,2\,x} - k_{HMM,sep\,x})/(k_{HMM,2\,x} - k_{HMM,1\,x})$, increases as the hyperbolic dispersion gets more squeezed; the z-bandwidth $k_{HMM,2\,z} - k_{HMM,sep\,z}$ and the z-density $dk_{HMM\,z}/dk_{HMM\,x}$ of large-k waves increase as the hyperbolic dispersion gets straighter. Refraction into air occurs within an angular range $\theta_1 \leq \theta \leq \theta_2$, where θ is the angle between the refracted k-vector and the optical axis z, $\theta_1 = \arctan(k_{HMM,1\,x}/\sqrt{k_0^2 - k_{HMM,1\,x}^2})$ and $\theta_2 = 90°$. The

limit case of infinite z-bandwidth and refraction normal to the interface ($\theta_1 = \theta_2 = 0°$) is reached when the hyperbola branches become straight lines and collapse onto the optical axis, as mathematically detailed in Appendix A.1. Although such situation appears ideal for applications, before drawing conclusions we must include energy propagation in our analysis. We recall that the power flux within a medium is perpendicular to the isofrequency surfaces (Subsection 2.2.1). When the two branches of the hyperbola become parallel to the z axis, namely the curvature at vertices becomes minimal, energy within the HMM flows parallel to the HMM-air interface and never reaches it, making outcoupling impossible. Therefore a tradeoff is required: the curvature of the hyperbola at vertices must be small enough to allow a sufficient z-bandwidth, but large enough to avoid that energy travels too long within the HMM – with the risk of being dissipated by loss – before touching the boundary with air.

5.2.2 Design guidelines and outcoupling configurations

We now derive comprehensive guidelines to optimize large-k wave extraction from a Type II HMM into air through a flat interface contained in the xy plane (top outcoupling). Our considerations are again restricted for simplicity to a cross-section of the dispersion curves in the $(k_x > 0, k_z > 0)$ quadrant. As concluded in the previous section, the target dispersion will be the one that enables infinite bandwidth and normal emission; once the optimum ε_{zz} and $\varepsilon_{\perp}$ are obtained, we will have to arbitrarily (the tradeoff depends on the application) relax the infinite bandwidth condition to achieve successful outcoupling.

The target dispersion corresponds to a limit hyperbolic curve with maximal straightening and maximal squeezing; these simultaneous requests are formalized in System (A.6) of Appendix A. When optimization is performed at a given emission frequency $\bar{\omega}$, we have two equations, involving two functions $\varepsilon_{\perp}(\bar{\omega}, \rho)$ and $\varepsilon_{zz}(\bar{\omega}, \rho)$, and

only one variable ρ. The resulting overdetermined system admits a solution $\bar{\rho}$ such that $\varepsilon_{zz}(\rho) \to 0^+$ as $\rho \to \bar{\rho}$, provided that $|\varepsilon_\perp(\rho)|$ approaches a finite value or approaches 0 less quickly than $\varepsilon_{zz}(\rho)$ does. Therefore, we optimize dispersion as follows: we choose $\bar{\rho}$ such that $\varepsilon_{zz}(\bar{\rho}) \sim 0^+$ (but not exactly $\varepsilon_{zz}(\bar{\rho}) = 0$, to avoid the energy propagation issue discussed above), making sure that the related condition on $\varepsilon_\perp(\bar{\rho})$ is verified. Fig. 5.3(c) shows a dispersion where ε_{zz} does not take the limit value 0, but is small enough to possess a band of outcoupled k-vectors, highlighted in light blue (short-k waves) and pink (large-k waves).

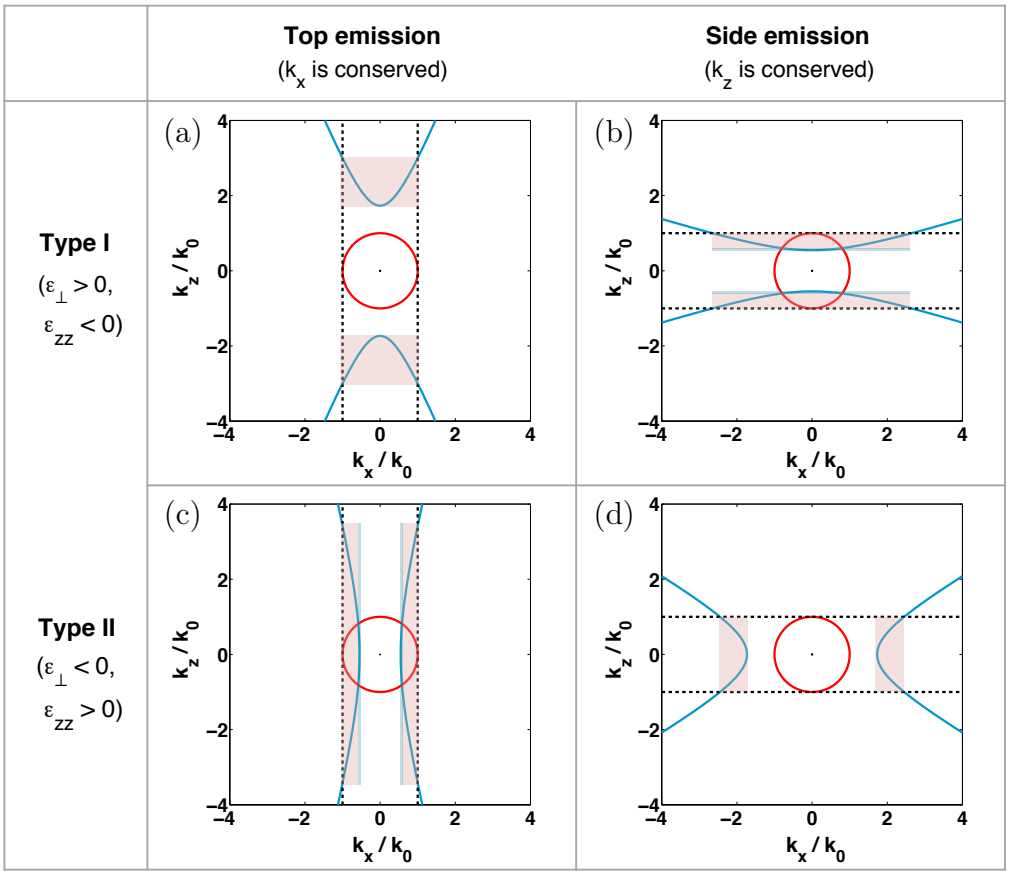

Figure 5.3: Cases of dispersion-assisted directional outcoupling from HMMs (blue hyperbola) into air (red circle). The effective parameters of the hyperbolic dispersions are: (a) $\varepsilon_\perp = 3$, $\varepsilon_{zz} = -0.5$; (b) $\varepsilon_\perp = 0.3$, $\varepsilon_{zz} = -3$; (c) $\varepsilon_\perp = -5$, $\varepsilon_{zz} = 0.3$; (d) $\varepsilon_\perp = -1$, $\varepsilon_{zz} = 3$. The band of outcoupled k-vectors is highlighted in light blue (short-k waves, only present in (b) and (c)) and in pink (large-k waves).

Large wavevectors can also be extracted when the HMM-air interface lies in the yz plane (side outcoupling). In this case, one equation suffices to request both maximal straightening and maximal squeezing (Appendix A.1). Its solution $\bar{\rho}$ satisfies $|\varepsilon_\perp(\rho)| \to 0^+$ as $\rho \to \bar{\rho}$, provided that $\varepsilon_{zz}(\rho)$ approaches a finite value or approaches 0 less quickly than $|\varepsilon_\perp(\rho)|$ does. In analogy to the previous reasoning, we do not select $\bar{\rho}$ such that $|\varepsilon_\perp(\bar{\rho})| = 0$, but rather $|\varepsilon_\perp(\bar{\rho})| \sim 0^+$; a situation where $\varepsilon_\perp$ is small enough to possess an outcoupled band, but not yet approaching the limit value 0, is represented in Fig. 5.3(d). While in the case of top extraction the outcoupled band always contains both short- and large-k waves, in the case of side extraction only the latter are present if the condition $\varepsilon_{zz}(\bar{\rho}) > 1$ is verified (like in Fig. 5.3(d)).

Type I dispersion is mathematically a 90° rotation of the Type II one (Appendix A.1). With arguments and caveats similar to those hitherto discussed, top outcoupling is achieved at $\bar{\rho}$ such that $|\varepsilon_{zz}(\rho)| \sim 0^+$ (a dispersion with small ε_{zz} is shown in Fig. 5.3(a)), while side outcoupling requires $\varepsilon_\perp(\rho) \sim 0^+$ (a dispersion with small $\varepsilon_\perp$ is shown in Fig. 5.3(b)). Both short- and large-k waves are always present in a side-outcoupled band, while a top-outcoupled one features exclusively large-k components if the condition $\varepsilon_\perp(\bar{\rho}) > 1$ is verified (Fig. 5.3(a)).

The design guidelines traced in the present subsection are summarized in Table 5.1.

Table 5.1: Design guidelines for dispersion-assisted outcoupling in HMMs. The notation $f(x) = o(g(x))$ as $x \to \bar{x}$, read "f is little-o of g as x approaches $\bar{x}$ ", means that $\lim_{x\to\bar{x}} f(x)/g(x) = 0$.

HMM Type	Outcoupling	Guideline (pick ρ such that..)	Caveat (verify that..)
Type I	Top	$\lvert\varepsilon_{zz}(\rho)\rvert \sim 0^+$	$\lvert\varepsilon_{zz}(\rho)\rvert = o(\varepsilon_\perp(\rho))$
	Side	$\varepsilon_\perp(\rho) \sim 0^+$	$\varepsilon_\perp(\rho) = o(\lvert\varepsilon_{zz}(\rho)\rvert)$
Type II	Top	$\varepsilon_{zz}(\rho) \sim 0^+$	$\varepsilon_{zz}(\rho) = o(\lvert\varepsilon_\perp(\rho)\rvert)$
	Side	$\lvert\varepsilon_\perp(\rho)\rvert \sim 0^+$	$\lvert\varepsilon_\perp(\rho)\rvert = o(\varepsilon_{zz}(\rho))$

5.3 Influence of loss on dispersion

Thus far we have assumed that the constituent materials of the ML or the NW are lossless. This implies that their permittivities ε_m and ε_d, and therefore the effective permittivity components $\varepsilon_\perp$, ε_{zz}, are real quantities. Loss in actual materials, mathematically represented by a nonzero imaginary part of permittivity, distorts the dispersion curve. In Eq. (5.4), the k-vector component conserved at the HMM-dielectric interface is the independent variable and takes only real values. Since now $\varepsilon_\perp$ and ε_{zz} are complex quantities, the k-vector component orthogonal to the interface becomes complex, and it is its real part that appears in the dispersion curve.

Effective permittivities with a small imaginary part do not alter excessively dispersion, compared with the lossless case. Our analysis showed that top outcoupling is achieved for $\mathrm{Re}\{\varepsilon_{zz}\}$-near-zero ($\mathrm{Re}\{\varepsilon_{zz}\}\sim 0^-$ for Type I, $\mathrm{Re}\{\varepsilon_{zz}\}\sim 0^+$ for Type II), and side outcoupling for $\mathrm{Re}\{\varepsilon_\perp\}$-near-zero ($\mathrm{Re}\{\varepsilon_\perp\}\sim 0^+$ for Type I, $\mathrm{Re}\{\varepsilon_\perp\}\sim 0^-$ for Type II). We subsequently investigate whether any coupling behavior is associated with a resonance, and therefore incurs a penalty for large losses (a large imaginary permittivity).

In ML HMMs, Eq. (5.2) prescribes that $\mathrm{Re}\{\varepsilon_\perp\}$ as a function of ω have a zero

induced by the zero of $\mathrm{Re}\{\varepsilon_m\}$; $\mathrm{Re}\{\varepsilon_{zz}\}$, according to Eq. (5.3), can have a zero as well, but also crosses zero in correspondence of a resonant pole [220]. The zero of $\mathrm{Re}\{\varepsilon_\perp\}$ and the pole of $\mathrm{Re}\{\varepsilon_{zz}\}$ can be continuously tuned with ρ: and since $\mathrm{Im}\{\varepsilon_\perp\}$ may be low, but $\mathrm{Im}\{\varepsilon_{zz}\}$ is always large, we conclude that for ML HMMs side outcoupling is more viable than top outcoupling. The situation is reversed for NW HMMs: in that geometry, the direction of free electron motion (parallel to the wires) is orthogonal to the one in MLs (parallel to the layers), so the role of the $\varepsilon_\perp$ and ε_{zz} components is exchanged. NW HMMs are therefore a better choice for top outcoupling, and a poor one for side outcoupling.

We now consider a hyperbolic medium with effective parameters $\varepsilon_\perp$, ε_{zz} calculated for a ML geometry, and optimize the side extraction of large-k waves at the wavelengths $\lambda_1 = 530$ nm and $\lambda_2 = 470$ nm relevant for optical communication. We achieve this goal by determining for a selected material system (Ag/Si for λ_1, Ag/SiO_2 for λ_2) the filling ratio that maximizes the bandwidth of outcoupled k-vectors. The SiO_2 permittivity is assumed to be 2.25, while the Ag and the Si permittivities are taken respectively from [205] and [206]. At λ_1, a Ag/Si effective medium displays a Type I behavior with $\mathrm{Re}\{\varepsilon_\perp\}\sim 0^+$ at $\rho = 0.58$ (the exact $\mathrm{Re}\{\varepsilon_\perp\}\rightarrow 0^+$ condition is achieved at decimal digits of ρ that are meaningless from a fabrication standpoint)(Figs. A.3(a) and (c) of Appendix A.3). The material permittivities $\varepsilon_{Ag} = -11.66 - 0.36i$ and $\varepsilon_{Si} = 17.23 - 0.44i$ result in effective parameters $\varepsilon_\perp = 0.5 - 0.4i$ and $\varepsilon_{zz} = -39.03 - 3.34i$. Restricting our considerations to the $(k_x > 0, k_z > 0)$ quadrant, we obtain a band including both short-k ($0 < k_z/k_0 \leq 0.53$, $0 < |\mathrm{Re}\{k_x/k_0\}| \leq 0.84$) and large-$k$ waves ($0.53 < k_z/k_0 \leq 1$, $0.84 < |\mathrm{Re}\{k_x/k_0\}| \leq 4.72$). The total outcoupled band, including the remaining 3 quadrants, is showed in Fig. 5.4(a). At λ_2 instead, a Ag/SiO_2 effective medium achieves a Type II regime with $\mathrm{Re}\{\varepsilon_\perp\}\sim 0^-$ at $\rho = 0.22$ (Figs. A.3(b) and (d) of Appendix A.3)). The material permittivities $\varepsilon_{Ag} = -8.15 - 0.28i$ and $\varepsilon_{SiO2} = 2.25$ generate effective pa-

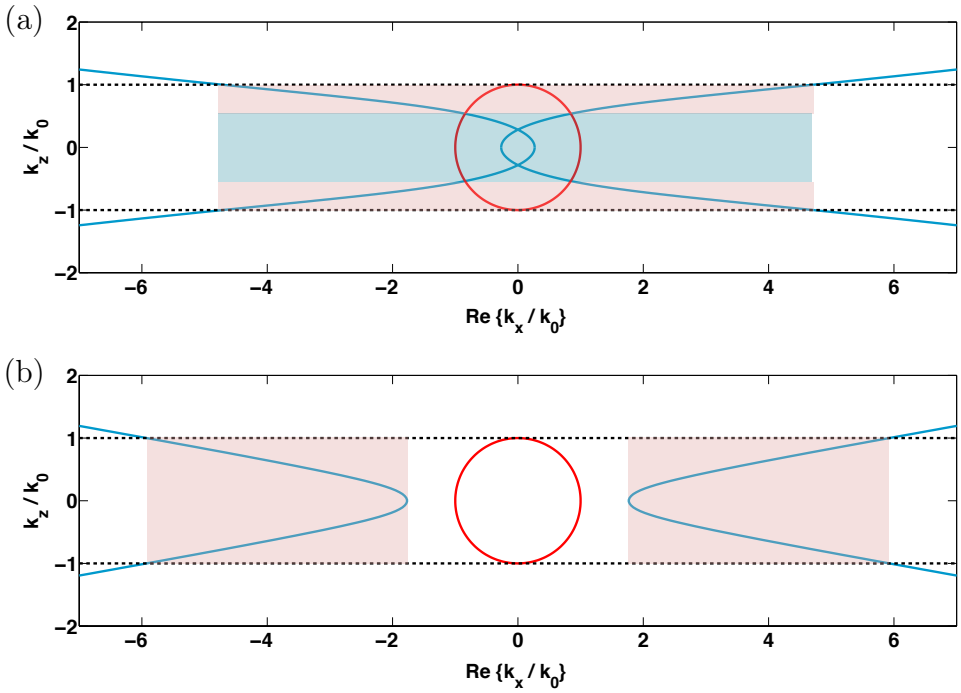

Figure 5.4: Dispersion of Type I and Type II effective media (blue curve) for lateral outcoupling into air (red curve), taking into account the actual loss of the constituent materials: (a) Ag/Si effective medium at $\lambda_1 = 530$ nm and filling ratio $\rho = 0.58$ (Type I), (b) Ag/SiO_2 effective medium at $\lambda_2 = 470$ nm and filling ratio $\rho = 0.22$ (Type II). The band of outcoupled k-vectors is highlighted in light blue (short-k waves, only present in (a)) and in pink (large-k waves).

rameters $\varepsilon_\perp = -0.04 - 0.06i$ and $\varepsilon_{zz} = 3.13 - 0.01i$. Again restricting our considerations to the $(k_x > 0, k_z > 0)$ quadrant, we obtain a band entirely composed of large-k waves ($0 < k_z/k_0 \leq 1$, $1.77 < |\mathrm{Re}\{k_x/k_0\}| \leq 5.98$). The total outcoupled band, including the remaining 3 quadrants, is showed in Fig. 5.4(b). Compared to the ideal behavior of lossless HMMs for side outcoupling (Figs. 5.3(b) and (d)), the Ag/SiO_2 dispersion does not present major alterations, whereas the Ag/Si dispersion exhibits distortion for values of $\mathrm{Re}\{k_x/k_0\}$ close to 0. While $\mathrm{Im}\{\varepsilon_\perp\}$ and $\mathrm{Im}\{\varepsilon_{zz}\}$ for the Ag/SiO_2 system are low enough to preserve the hyperbolicity of the dispersion, the correspondent parameters for the Ag/Si system, respectively one and two orders of magnitude larger, alter the dispersion by conferring it a hybrid hyperbolic-elliptical character.

5.4 Influence of finite periodicity on dispersion

Effective medium theory, leading to Eqs. (5.2) and (5.3), assumes that the length of the ML period is much smaller than the effective wavelength of light within the medium. As the momentum k_x increases, the effective wavelength $\lambda_{eff} = 2\pi/k_x$ decreases. The accuracy of EMT is thus circumscribed to a finite range of supported large-k waves. Bloch's theorem [221, 222], unlike EMT, explicitly incorporates the thickness of the ML components, and lets us estimate the maximum of the large-k range as $\max[\mathrm{Re}\{k_x/k_0\}] = \lambda_0/(2L)$. In this formula, $\lambda_0/(2L)$ is the normalized Brillouin zone boundary, L is the period length and λ_0 the vacuum wavelength. If, for instance, a practically achievable period length $L = 20$ nm is assumed for both the Ag/Si and the Ag/SiO_2 MLs, the first supports a maximum $\mathrm{Re}\{k_x/k_0\} = 13.25$ at the vacuum wavelength λ_1, while the second supports a maximum $\mathrm{Re}\{k_x/k_0\} = 11.75$ at the vacuum wavelength λ_2. The upper extremes of the respective outcoupled bands, determined in Section 5.3, fall below these maxima: therefore, our results based on the effective medium are consistent for real structures with the above-mentioned period length.

To further assess the accuracy of EMT in a quantitative fashion, we compute by means of Bloch's theorem the isofrequency surfaces of the Ag/Si and the Ag/SiO_2 systems. To simplify the notation we restrict our considerations to the $k_x k_z$ plane. Assuming a ML of infinite lateral and vertical extent, finite periodicity L, and with layers orthogonal to the z axis, the dispersion for TM waves is governed by [223]

$$k_{B,z} = L^{-1} \cos^{-1}\left(\frac{A+D}{2}\right), \tag{5.6}$$

where

$$A, D = \exp(\pm i k_{m,z} d_m) \left[\cos(k_{d,z} d_d) \pm i \frac{1}{2} \left(\frac{\varepsilon_d k_{m,z}}{\varepsilon_m k_{d,z}} + \frac{\varepsilon_m k_{d,z}}{\varepsilon_d k_{m,z}} \right) \sin(k_{d,z} d_d) \right]. \quad (5.7)$$

Eq. (5.6) expresses the effective k_z component for the entire ML, $k_{B,z}$, as a function of the conserved component k_x, treated as an independent variable and implicitly contained in Eq. (5.7): here, the $+$ and $-$ signs correspond respectively to A and D, d_m (d_d) is the thickness of the metallic (dielectric) layers, and $k_{m,z} = \sqrt{\varepsilon_m k_0^2 - k_x^2}$ $\left(k_{d,z} = \sqrt{\varepsilon_d k_0^2 - k_x^2}\right)$ is the z component of the wavevector in the metallic (dielectric) layers.

Fig. 5.5(a) shows the Bloch dispersion of TM-polarized waves in a periodic Ag/Si system at λ_1, with $L = 20$ nm and $\rho = 0.58$ (corresponding to $d_{Ag} = 11.6$ nm and $d_{Si} = 8.4$ nm), and compares it with the EMT dispersion of Fig. 5.4(a). The maximum outcoupled component $\mathrm{Re}\{k_x/k_0\} = 2.93$ is 38% lower than the corresponding value obtained with EMT. An analogous comparison is shown in Fig. 5.5(b) for a periodic Ag/SiO_2 system at λ_2, with $L = 20$ nm and $\rho = 0.22$ (corresponding to $d_{Ag} = 4.4$ nm and $d_{SiO2} = 15.6$ nm). The maximum outcoupled component $\mathrm{Re}\{k_x/k_0\} = 4.66$ is 22% lower than the corresponding value obtained with EMT. This analysis shows that, although reduced, the outcoupled bandwidth remains significant when accounting for finite periodicity. Therefore, the general method we propose retains its validity beyond EMT.

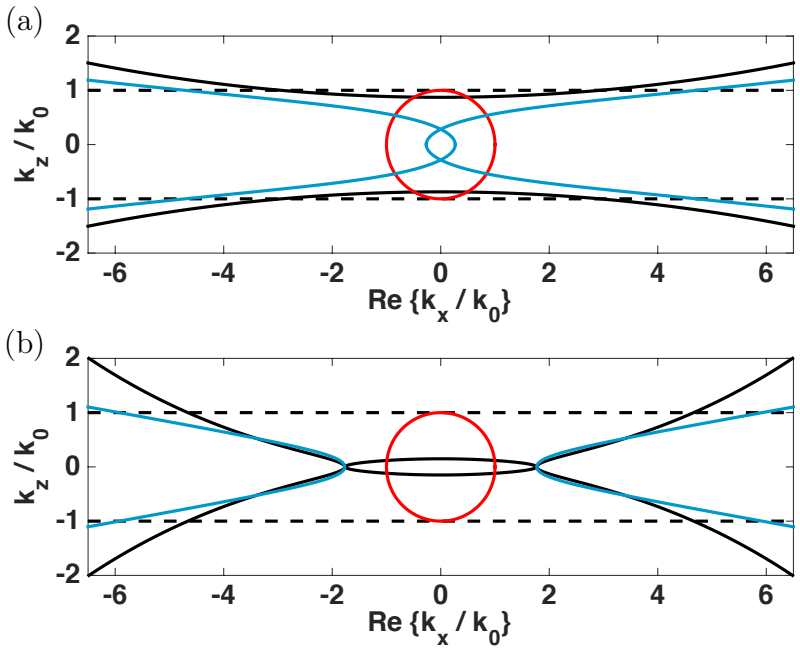

Figure 5.5: Influence of finite periodicity on outcoupling. Black curve: Bloch dispersion; blue curve: EMT dispersion; red curve: dispersion of air. (a) Ag/Si ML with period $L = 20$ nm and filling ratio $\rho = 0.58$ at $\lambda_1 = 530$ nm. (b) Ag/SiO_2 ML with period $L = 20$ nm and filling ratio $\rho = 0.22$ at $\lambda_2 = 470$ nm.

5.5 Quantum dot-HMM coupling

We apply the results of Section 5.3 to an elemental light-emitting system, composed of a quantum dot and a block of HMM in air. The system is designed to operate at $\lambda_1 = 530$ nm, and to be implemented in a ML geometry: the effective parameters $\varepsilon_\perp$, ε_{zz} are thus obtained from a Ag/Si ML HMM with $\rho = 0.58$, and enable large-k extraction from the lateral faces of the block. By means of full wave 2D COMSOL simulations, we study a HMM block infinitely extended along the y direction, and with rectangular cross-section $l_x l_z$. The height $l_z = 200$ nm corresponds to a ML of 10 periods of length $L = 20$ nm; a well-controlled structure of this kind has been grown via sputtering by our group in the past [18]. The width $l_x = 3$ μm is easily achievable with standard photolithographic techniques. We model the QD with a point dipole emitting at λ_1, located 5 nm below the bottom surface and 150 nm left of the right face of the HMM block (Fig. 5.6). Such

asymmetric positioning allows a simultaneous evaluation of the extraction efficiency from the HMM lateral faces when the emitter-face distance is either within (150 nm) or outside of (2850 nm) the near-field.

The large-k waves contained in the spectrum of the dipole are coupled into the HMM block, through which they travel until they reach the lateral boundary with air. To quantify how dispersion inhibits or favors their extraction into the far-field, we compare the performance of an unoptimized filling ratio, $\rho_A = 0.54$, with that of the optimized one, $\rho_B = 0.58$. The respective isofrequency contours in the $k_x k_z$ plane are

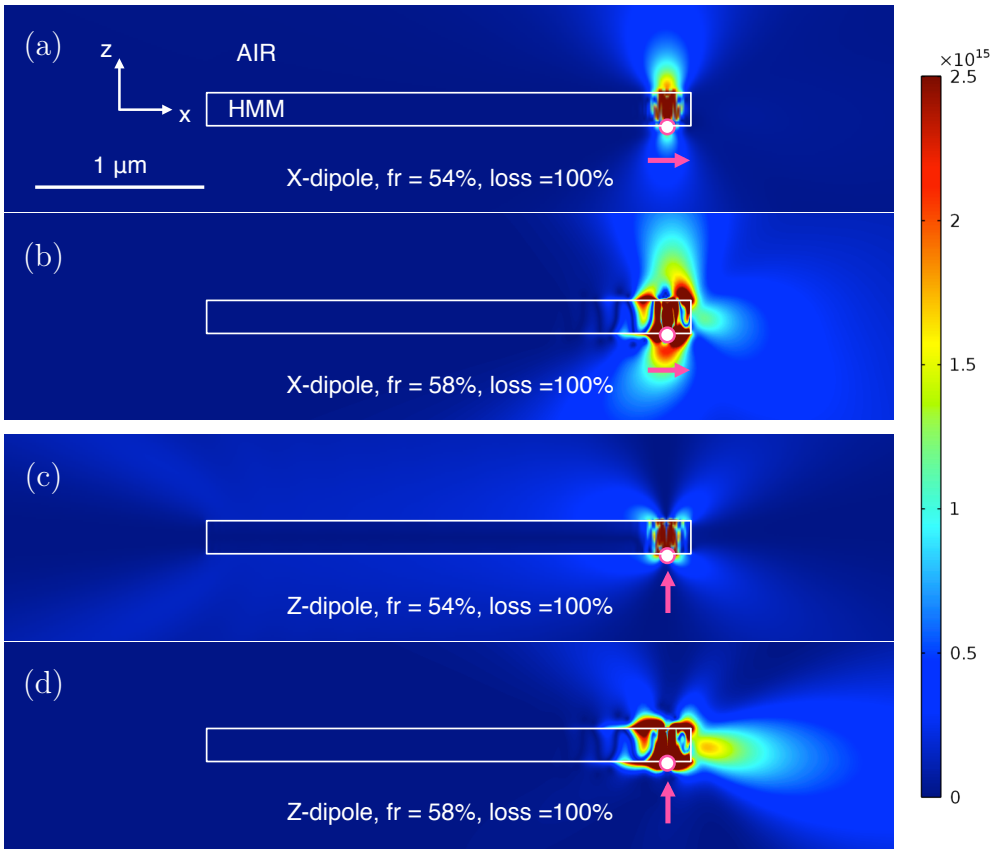

Figure 5.6: Spatial power distribution (magnitude of the Poynting vector) at $\lambda_1 = 530$ nm of a dipole 5 nm below a block of Ag/Si effective medium in air. The dipole location and orientation are respectively indicated by a pink-bordered white dot and a pink arrow below it. The material loss of the HMM corresponds to 100% of its original value. (a) X-dipole, filling ratio $\rho_A = 0.54$; (b) X-dipole, filling ratio $\rho_B = 0.58$; (c) Z-dipole, filling ratio $\rho_A = 0.54$; (d) Z-dipole, filling ratio $\rho_B = 0.58$.

shown in Fig. A.4 of Appendix A.3 At ρ_A, the HMM exhibits Type I behavior, and only an extremely narrow band of dispersion-outcoupled large-k waves is supported; as ρ is increased, the HMM still retains Type I nature, but the bandwidth of the extracted large-k waves grows, assuming its largest value at ρ_B (cfr. Section 5.3). The effectiveness of outcoupling through the lateral faces is determined by the amount of power emitted into a circular arc coaxial with $\hat{\mathbf{x}}$, with vertex in the center of the face and aperture $\theta = 30°$. Fig. 5.6 illustrates the different response of the two filling ratios to a dipole oriented along $\hat{\mathbf{x}}$ ("X-dipole") and to one oriented along $\hat{\mathbf{z}}$ ("Z-dipole"). For an X-dipole, the power outcoupled through the right face of the HMM block at ρ_B results in 7 times larger than that outcoupled at ρ_A, while for a dipole oriented along $\hat{\mathbf{z}}$ ("Z-dipole"), the power extracted at ρ_B exceeds by 39 times that extracted at ρ_A. The dipole-HMM interaction is stronger for a Z-dipole, which outcouples at ρ_B almost twice as much power as an X-dipole. Due to the material loss of the hyperbolic medium, large-k extraction efficiency decreases as the emitter-face distance is increased: the power outcoupled at ρ_B through the left face is 3 orders of magnitude lower than that outcoupled through the right one, both for an X- and for a Z-dipole. We notice that at ρ_A some radiation, guided by the HMM-air interface, reaches the left side of the HMM and gets scattered by the edges; but power propagation through the bulk of the HMM, which is what our outcoupling mechanism leverages, is again prevented by loss.

The radiation extracted into the far-field through the right face is polarized parallel to the optical axis $\hat{\mathbf{z}}$, regardless of the dipole orientation (Fig. 5.7). Such behavior has been experimentally observed in a luminescent hyperbolic metasurface, composed of alternating Ag layers and InGaAsP multiple QWs (MQWs), where both parallel- and perpendicular-polarized pumping of the MQWs with respect to the optical axis result in parallel-polarized emission [224]. It is attributed to the fact that only modes with an electric field component parallel to the optical axis are allowed to propagate in a

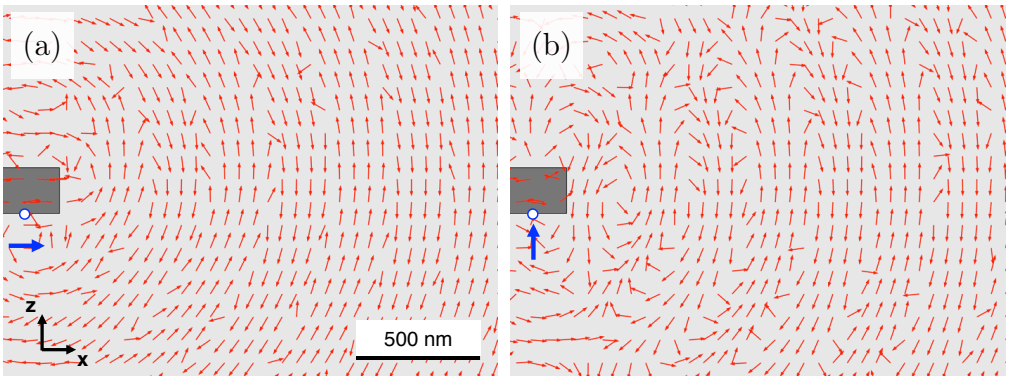

Figure 5.7: Electric field polarization of the dipole radiation outcoupled through the right face of the HMM block (whose rightmost portion is shown in grey on the left of the image) at the optimized filling ratio $\rho_B = 0.58$. The dipole location and orientation are respectively indicated by a white dot and a blue arrow below it. Whether the dipole is polarized along $\hat{\mathbf{x}}$ (a) or along $\hat{\mathbf{z}}$ (b), the radiation leaving the HMM face is predominantly polarized along $\hat{\mathbf{z}}$.

hyperbolic medium [225].

The potential of dispersion-assisted outcoupling becomes apparent if we artificially reduce the imaginary parts $\mathrm{Im}\{\varepsilon_\perp\}$ and $\mathrm{Im}\{\varepsilon_{zz}\}$, representing loss, to 1% of their original value (Fig. 5.8). In this ideal case, power propagates inside the hyperbolic medium along the characteristic resonance cones, reflected off the top and bottom surfaces of the HMM, until it reaches the left and right boundaries with air. Here, large-k waves are efficiently extracted only when the filling ratio is optimized: the power outcoupled through the right face at ρ_B is 3 orders of magnitude larger than the one outcoupled at ρ_A, both for an X- and for a Z-dipole. The strong imbalance between the left and the right face is also removed, as for an X-dipole the power outcoupled at ρ_B through either boundary is almost the same, while for a Z-dipole the left face outcouples at ρ_B 1.7 times as much power as the right one. Which face outcouples the largest power depends on its distance from the dipole. The radiation reaching one face is the superposition of the waves directly traveling to said face and those reflected off the other, whose propagation is not any longer suppressed by loss. For certain dipole locations, the contribution of

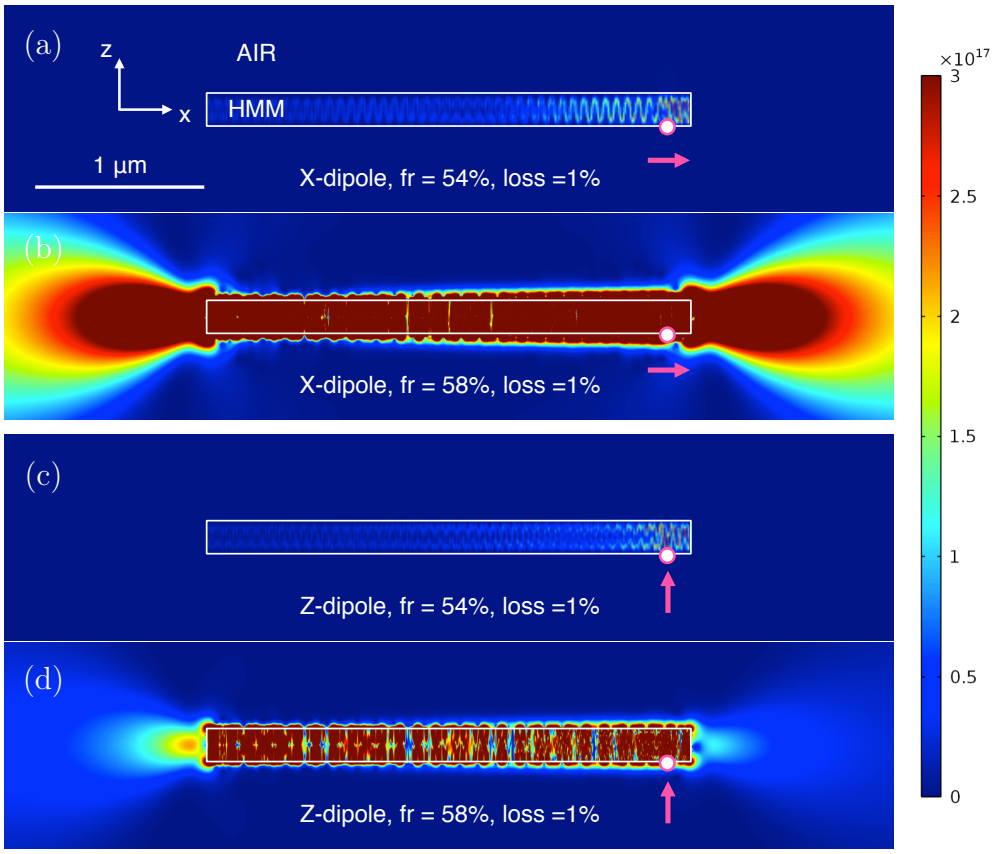

Figure 5.8: Spatial power distibution (magnitude of the Poynting vector) at $\lambda_1 = 530$ nm of a dipole 5 nm below a block of Ag/Si effective medium in air. The dipole location and orientation are respectively indicated by a pink-bordered white dot and a pink arrow below it. The material loss of the HMM has been reduced to 1% of its original value. (a) X-dipole, filling ratio $\rho_A = 0.54$; (b) X-dipole, filling ratio $\rho_B = 0.58$; (c) Z-dipole, filling ratio $\rho_A = 0.54$; (d) Z-dipole, filling ratio $\rho_B = 0.58$.

interference selects the face farther from the dipole as the main outcoupling gateway. Radiation polarized along the optical axis $\hat{\mathbf{z}}$ irrespective of the dipole orientation is emitted into the far-field through both of the lateral faces.

The simultaneous approximation of a ML HMM with an effective medium description and of the 3D space with a 2D environment enables the study of extended structures (size $\geq$ few μm) with an accurate mesh (mesh element size of the order of 1 nm) and in a reasonable computational time (not exceeding few hours). To test the

predictions of our outcoupling method in the absence of approximations, in Appendix A.2 we perform a 3D analysis of the coupling between a quantum dot (point dipole) and a block of HMM of reduced size (base 300 nm x 300 nm, height 200 nm). The Si/Ag ML HMM is first modeled as an effective medium, and then as a periodically layered structure. The results obtained are consistent with the general findings described here.

5.6 Discussion

With the due distinctions in terms of light coherence, a system formed by a suitably designed HMM block coupled to solid-state quantum emitters (QWs, QDs) can become the equivalent of an edge-emitting laser or a vertical-cavity surface-emitting laser (VCSEL), based on spontaneous rather than stimulated emission. "Hyperbolically-enhanced" LEDs with a modulation speed comparable to that of lasers could replace the latter in very-short-haul optical interconnects (on-chip or chip-to-chip communications), where their limitations related to pulse broadening and dispersion do not outweigh their advantages in energy budget, thermal management, reliability and manufacturing cost [20].

Our analysis showed that ML HMMs naturally support side emission, but are not suited for top emission. In addition, as observed in the previous section, the intrinsic loss of constituent materials restricts efficient outcoupling to those emitters in the near field of the side interface. These two constraints can be relaxed simultaneously by fabricating the ML into vertical lamellae, where the non-metallic constituent is a gain medium such as a semiconductor MQW. A configuration of this kind was recently demonstrated with a Ag/InGaAsP system [226, 227, 228, 229, 224]. Operating in the 1200 nm – 1600 nm spectral range, the structure exhibits narrow bands of large-k waves that outcouple to air without the need for a grating, for the reasons theoretically explained in the present

work. Another design that meets the top emission and efficient outcoupling requirements exploits a hyperlens-like geometry: the layers here are arranged in a concentric semi-spherical or semi-cylindrical stack, contained in the $z < 0$ region and comprised between the external and internal radii r_{ext} and r_{int}, and the surface of the innermost layer is coated with QDs. Provided that r_{ext} is within the near field of the emitters, radiation from the QDs couples to the HMM, shortly travels along the direction tangential to the layers without experiencing excessive attenuation and gets extracted along the z axis. An alternative approach to achieve top emission consists in growing the ML on the side walls of a vertical nanowire light-emitting structure that incorporates one or more MQWs; the geometry of the nanowires and of the MQWs can be adjusted, as shown in [230] for blue/green-emitting III-nitride semiconductor nanowires, to boost the emitter-ML interaction and optimize the outcoupling efficiency. Top emission is convenient from a manufacturing standpoint: while edge-emitting devices grown on a wafer must be first diced in sub-units and then tested individually, surface-emitting ones can be tested all at once on the wafer where they are fabricated. Side emission however is desirable for on-chip or chip-to-chip communication, and enables direct light coupling into waveguide-like planar devices. In order to maintain a HMM feature size compatible with photolithography, without limiting efficient outcoupling to the emitters closer to the side faces, the imaginary component of the constituent permittivities can be minimized with low-loss materials [231, 232] or compensated for with gain. Van der Waals heterostructures, built with single-atomic layer materials ("2D crystals") including graphene, hexagonal boron nitride (hBN) and 2D oxides [233], can incorporate atomic monolayers of transition metal dichalcogenides such as tungsten diselenide (WSe_2) and tungsten disulfide (WS_2) as active media [234, 235]. Heterostructures based on hBN, a natural HMM [236], or on ultra-thin MLs with 2D active layers, can greatly reduce loss and fully leverage our light extraction method, since their size forbids grating inscription

as a practical option. Finally, hybrid ML-NW geometries, or MLs with atomically thin metallic films subject to quantum confinement, might elude with their dispersion the guidelines traced in Subsection 5.2.2.

The feasibility of our approach relies on the exact control of the filling ratio. In the visible range, the ML period must not exceed few tens of nanometers in order to be sub-wavelength (and therefore justify the effective medium approximation). Metallic films for operations at visible wavelengths are typically grown by DC sputtering or e-beam evaporation. In either case, at thicknesses of 10 nm or less, the metal forms islands, rather than a uniform layer. While the size and shape of the grains can be controlled to some extent by tuning the deposition parameters, the resulting morphology intrinsically yields a space-dependent filling ratio. Therefore, the effective HMM parameters need to have a good tolerance with ρ variations, to preserve the applicability of our model. This represents less of a concern for HMMs in the infrared (IR) range: NW and ML systems can be grown with sub-nanometer accuracy via atomic layer deposition (ALD) and chemical vapor deposition (CVD) [232, 237], and periods of several tens of nm are already well sub-wavelength. IR HMMs hence constitute a promising candidate for early experimental testing. A dynamic fine-tuning of the filling ratio from non-outcoupling to outcoupling, detectable as an enhanced directionality of the emission pattern, can be performed in voltage-controlled HMMs [236, 238, 239].

An emitter-HMM system suitable for optical communication should simultaneously maximize, at a given wavelength, the far-field power extracted into a preferential direction and the Purcell factor, which determines the modulation bandwidth enhancement. However, the filling ratios that optimize both quantities in general do not coincide. A recent work suggests tapering a hyperbolic ML block to adiabatically outcouple large-k waves from its side [219]. According to that approach, we could design a HMM with filling ratio varying from ρ_1 (in the proximity of the emitter) to ρ_2 (away from the

emitter), to first maximize the Purcell factor and then the outcoupling. Such transition however must happen over a space scale of few microns, which imposes a constraint on the device size. In addition, power extraction is limited to the tapering direction, making the mechanism inefficient. Finally, the shadowed deposition technique utilized seems impractical in an industrial context. We propose instead to keep a single-ρ design, that achieves a balanced performance between outcoupling and Purcell factor. Optimization methods can be developed to tune this trade-off, which we believe is the most viable solution in a mass production perspective.

5.7 Conclusions

The present chapter introduced a systematic approach to extract large-k waves from HMMs without the use of a grating. This novel method relies on dispersion engineering, and is applicable to any medium, natural or artificial, described by a hyperbolic permittivity tensor. Extraction of a large-k wave band from the top or from the side faces of the HMM is achieved in the epsilon-near-zero regime of either permittivity component. Loss in the effective medium, dictated both by the loss and the ML or NW arrangement of its constituent materials, selects the preferential outcoupling configuration: side outcoupling for ML HMMs, top outcoupling for NW HMMs. We provided guidelines to maximize the extent of the large-k wave band extracted through the top or side faces, and we applied them to the optimization of a Ag/Si and a Ag/SiO_2 ML HMM, respectively at $\lambda_1 = 530$ nm and $\lambda_2 = 470$ nm. We further discussed how the effective medium description moderately overestimates the outcoupled bandwidth, when the finite periodicity of practical HMM realizations is taken into account. We finally studied a QD-Ag/Si ML HMM system at λ_1, observing an almost 40-fold increase in lateral power extraction at an optimized filling ratio compared to an unoptimized one.

When the HMM losses are artificially decreased to 1% of their original value, not only the optimized filling ratio outperforms the unoptimized one by 3 orders of magnitude, but power effectively outcouples also through the lateral face farther from its location.

To exemplify the application of our paradigm, we considered the particular case of ML HMMs operating at visible wavelengths. Future research will explore IR material combinations, with the goal of optimizing lateral extraction in MLs for fiber-optic communication. In parallel, NW HMMs will be studied in view of designing an emitter-HMM system for top outcoupling.

Chapter 5, in part, has been submitted for publication. L. Ferrari, J. S. T. Smalley, Y. Fainman and Z. Liu, “Hyperbolic metamaterials for dispersion-assisted directional light emission”. The dissertation author is the first author of this paper.

Chapter 6

Design of blue InGaN/GaN high-speed plasmonic LED

6.1 Introduction

The widespread adoption of visible light communication (VLC) systems based on LED transmitters requires the simultaneous increase in efficiency and speed of the optical source [240, 241]. Efficiency is measured by the external quantum efficiency (EQE) η_{EQE} [242], while speed is quantified by the 3dB modulation bandwidth f_{3dB} [243]. Most research on the indium gallium nitride (InGaN) system, suited for blue and green emission, has focused on improving EQE because this metric, and its dependence on the injection current density J_{inj}, is one of the most important factors for the growth of LEDs as an illumination source for general lighting purposes [242]. While the market for lighting exceeds many billions of dollars and general illumination accounts for 20% of U.S. electrical energy consumption [242], the modulation rate of LEDs is poised to grow in importance due to the need to couple information processing with illumination [240, 241]. Therefore, strategies that advance efficiency and speed simultaneously are

much sought after.

Plasmonic and hyperbolic metamaterials (MMs) have gained much attention over the past decade because of their ability to dramatically enhance light-matter interaction [26]. The increased photonic density of states provided by metals, which can be further enhanced and wavelength-tuned with hyperbolic media [43], enables the controlled reduction of the spontaneous emission lifetime τ_{sp} of a quantum light source (fluorescent molecule, quantum dot, quantum well, nitrogen-vacancy center in nanodiamonds [57]), essential for high-speed devices. Lifetime reductions of 10 to 100 times relative to the vacuum have been reported using various realizations of plasmonic and hyperbolic MMs [18, 208, 209, 244]. In most cases, however, unpatterned structures demonstrated to increase the emission speed suffer from low radiative efficiency, and the mechanisms leveraged to overcome such limitations, including surface texturing [224] or the use of nanoparticles in lieu of patterned films [22], hinder their integrability with electronics. Therefore, in order to yield feasible electrically-driven light sources for fast optical transmitters, a design which enhances modulation speed while preserving a good radiative efficiency must carefully optimize the integration between the light source and the plasmonic/hyperbolic nanostructured medium.

The recent demonstration of a light-emitting hyperbolic metasurface, based on nanostructured silver (Ag) and indium gallium arsenide phosphide (InGaAsP) QWs [224], shows that III-V compound semiconductors are a promising candidate for simultaneously efficient and fast LEDs. Moreover, the anisotropic polarization response observed in the metasurface can boost the transmission rate of LEDs used in VLC by introducing an additional channel (light polarization) for information encoding. However, VLC requires translation of this technology to visible frequencies. Designs that simultaneously yield improved speed and light output at blue wavelengths have been evoked, but they remain the subject of theoretical studies [245].

In this chapter we experimentally demonstrate a novel plasmonic LED (PLED) configuration, incorporating a Ag nanohole grating within an InGaN/GaN LED. The PLED exhibits a simultaneous increase in efficiency and speed, compared to conventional LEDs with and without unpatterned plasmonic inclusions, respectively. Through spatio-temporally resolved photoluminescence measurements, we determine a 40-fold decrease in spontaneous emission lifetime, which sets an upper bound to the modulation bandwidth in the GHz regime. Additionally, through careful optimization of the plasmonic nanohole grating, we demonstrate a 10-fold increase in outcoupling efficiency relative to a flat plasmonic film. Our work bridges the plasmonic metamaterial and III-nitride semiconductor communities, laying the groundwork for high-speed, high-efficiency blue LEDs for VLC applications. The chapter is organized as follows. In Section 6.2 we present the theoretical background for understanding the fundamental tradeoff between high efficiency and high speed LEDs. Next, in Section 6.3, we provide the design of the PLED structure. In Section 6.4 we present our results of static and spatio-temporally resolved photoluminescence (PL) measurements. A detailed analysis of these results follows in Section 6.5. The discussion of our findings is presented in Section 6.6, followed by our conclusions in Section 6.7.

6.2 Theoretical background

The EQE of an LED is conveniently understood as a product of the injection, internal, and collection efficiencies, η_{Inj}, η_{IQE} and η_{Col}, respectively [246]:

$$\eta_{EQE} = \eta_{Inj}\eta_{IQE}\eta_{Col}. \tag{6.1}$$

The injection efficiency may be defined as

$$\eta_{Inj} = \frac{\Gamma_{act}}{\Gamma_{act} + \Gamma_{n-act}}, \tag{6.2}$$

where Γ_{act} and Γ_{n-act} are the rates at which electron-hole pairs are injected into the active and non-active regions, respectively. The active region is the quantum well volume, while the non-active region comprises the quantum barriers and the cladding regions (p- and n-doped), containing defect or trap states.

The internal quantum efficiency may be defined as

$$\eta_{IQE} = \frac{\Gamma_{rad}}{\Gamma_{rad} + \Gamma_{n-rad}}, \tag{6.3}$$

where Γ_{rad} and Γ_{n-rad} are the rates at which electron-hole pairs that do enter the active region recombine radiatively and non-radiatively, respectively. The radiative recombination rate may be increased by emission into surface plasmons, which are large-wavevector surface waves at the interface between a metal and a dielectric (here the semiconductor heterostructure) [247]. Non-radiative recombination occurs due to defect and surface states, and to Auger recombination [246].

The collection efficiency may be defined as

$$\eta_{Col} = \frac{\Gamma_{det}}{\Gamma_{det} + \Gamma_{n-det}}, \tag{6.4}$$

where Γ_{det} and Γ_{n-det} are the rates at which the generated photons are detected and not detected, respectively. The detected photon rate can be increased if the radiative recombination rate is increased through plasmonic coupling, and the plasmon is later

scattered into the far-field [247]. In the absence of an outscattering mechanism, the plasmon remains bound to the near-field of the metal-dielectric interface, eventually dying off due to material loss. Therefore, in order for collection efficiency to benefit from plasmon generation, an extraction mechanism such as a grating or a nanostructure needs to be incorporated [18, 19].

The 3dB direct modulation bandwidth of the LED is defined as the frequency of direct modulation at which the output power drops to one half its peak value. In the limit discussed in Appendix B, the maximum 3dB bandwidth f'_{3dB} is determined by the effective carrier lifetime τ_{eff}:

$$f'_{3dB} = \frac{1}{2\pi\tau_{eff}} = \Gamma_{eff} = \Gamma_{rad} + \Gamma_{n-rad}. \tag{6.5}$$

Hence, increasing Γ_{rad} increases both η_{IQE} and f'_{3dB}. On the other hand, an increase in Γ_{n-rad} increases f'_{3dB} at the expense of η_{IQE}.

6.3 Plasmonic LED design

We consider a PLED system formed by an InGaN/GaN LED and a nanostructured Ag plasmonic film. The LED consists of an nGaN layer grown on a sapphire substrate, followed by an InGaN/undoped GaN multiple quantum well heterostructure and a pGaN layer (see Subsection 6.8.1). A PLED design simultaneously capable of high-speed and efficient operation must synthesize a fundamental dichotomy between plasmonic and electronic requirements. On the one hand, the near-field coupling between the MQW emitting region and the pGaN/Ag interface, resulting in the generation of SPs, is maximized as their distance is minimized. Such distance, coinciding with the pGaN layer thickness t_{pGaN}, must be shorter than the SP penetration depth in GaN, given

by $Z = \lambda/2\pi[(\varepsilon'_{GaN} - \varepsilon'_{Ag})/\varepsilon'^2_{GaN}]^{1/2} \approx 37$ nm [134], where ε'_{GaN} and ε'_{Ag} are the real parts of the permittivity in the pGaN and Ag layers, respectively [248, 205]. On the other hand, to maintain proper electronic transport, the pGaN layer must be thicker than the p-side depletion width of the diode, given by $x_{p0} = \{(2\varepsilon'_{GaN} V_{bi} n)/[qp(n + p)]\}^{1/2} \approx 44$ nm [249], where V_{bi} is the built-in voltage, $n \approx 6 \times 10^{18}$ cm^{-3} and $p \approx 5 \times 10^{17}$ cm^{-3} are the carrier concentrations in the nGaN and the pGaN, respectively (see Subsection 6.8.1), and $q = 1.6 \times 10^{-19}$ C is the fundamental charge. The built-in voltage is given by $V_{bi} = (k_B T/q) \ln[(np)/n_i^2]$, where $k_B T = 0.026$ eV at room-temperature and $n_i \approx 1 \times 10^{10}$ cm^{-3} is the intrinsic carrier concentration [250].

To circumvent this inherent conflict, past authors have experimentally explored a design with Ag nanoparticles embedded in undoped GaN [249], or theoretically envisioned a device based on side-emitting microtubules [245]. We instead propose to pattern a grating of nanoholes through the pGaN layer, down to the MQW, and then coat it with a plasmonic Ag film (Fig. 6.1(a)). Our solution leverages the nanostructured nature of the Ag film, necessary to outcouple SPs into the far field, to divide the PLED in two vertical volumes: a "plasmonic" one, occupied by the nanoholes, where the MQW-Ag film distance can be arbitrarily controlled, and an "electronic" one, free from nanoholes, where the diode behavior is preserved. While such general approach conveniently enables a plasmonic-electronic tradeoff, a geometric optimization of the nanoholes is still required, to find the MQW-nanopatterned Ag film relative positioning which maximizes SP generation and outcoupling. To this end, we fabricate on an InGaN/GaN LED chip with pGaN thickness $t_{pGaN} = 130 - 140$ nm (Fig. 6.1(b)) six 6 µm x 6 µm gratings (labeled "II" to "VII", since a preliminarily patterned "grating I" was utilized for etching depth calibration), all with identical hole diameter $d_h = 120$ nm and pitch $p_h = 300$ nm. The hole depth d_{etch} of the gratings is increased by a constant step from a value smaller (grating II) to a value larger (grating VII) than t_{pGaN}, in the approximate range

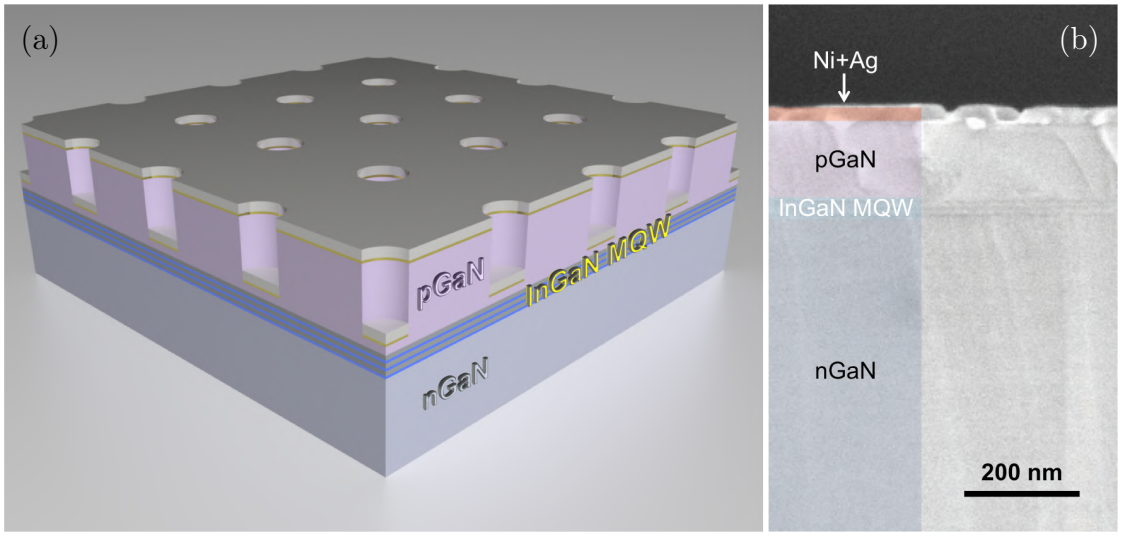

Figure 6.1: (a) Schematic of the LED + nanopatterned plasmonic film. Bottom to top: nGaN layer (grey), three InGaN QW (blue) - InGaN QB (dark grey) pairs, pGaN (violet). The thin bilayer deposited above the pGaN surface and inside the holes is made of Ni (ochre) and Ag (silver gray). (b) Ultra-high resolution scanning electron microscope (UHR SEM) cross section of the cleaved sample, in a region without gratings. The different components of the structure are highlighted in false color on the left.

100-200 nm. After nanohole milling, accomplished via focused ion beam, a 2 nm Ni adhesion layer followed by a 20 nm Ag layer is deposited everywhere on the sample (Subsection 6.8.2). In the next sections we show through experimental characterization and numerical verification that a non-obvious hole depth exists, which allows efficient generation and far-field scattering of SPs. This feature, in addition to the high-speed capability and sufficient pGaN thickness for diode behavior, makes our PLED design a viable one for practical VLC applications.

6.4 Static and spatio-temporally resolved photoluminescence

The static PL spectrum of the PLED is collected with the standard micro-PL setup detailed in Subsection 6.8.3. Compared to a control LED, with identical semiconductor

heterostructure but without flat nor nanostructured metal, the PLED emission from an area where only a flat Ag film is present exhibits a slight red-shift and a decrease in intensity (Fig. 6.2(a)). The first may be attributed to local heating, while the second can be traced to quenching effects. Since the PL peak of the PLED occurs at $\lambda_0 = 450$ nm, this is the chosen detection wavelength for the following spatio-temporally resolved PL characterization. By means of the setup described in Subsection 6.8.4, we perform a sub-micrometric raster scan of the PLED area occupied by the gratings, detecting at each step the PL lifetime and intensity. The lifetime values measured in the grating regions are comparable for all gratings, regardless of their hole depth. The hole pitch, identical for all gratings, plays indeed a dominant role in controlling the lifetime reduction [18], while the depth mainly impacts the efficient outcoupling of SPs into the far field, as we show later in this section. A representative decay curve of the PLED, measured on grating II, is compared in Fig. 6.2(b) with the one of the control LED: the respective lifetimes are $\tau_{PLED} = 0.08$ ns and $\tau_{cont} = 3$ ns, corresponding to an almost 40-fold shortening. By means of Eq. (6.5), we predict for the PLED an upper modulation bandwidth of about 2 GHz. The calculated frequency responses of the control LED and of the PLED are

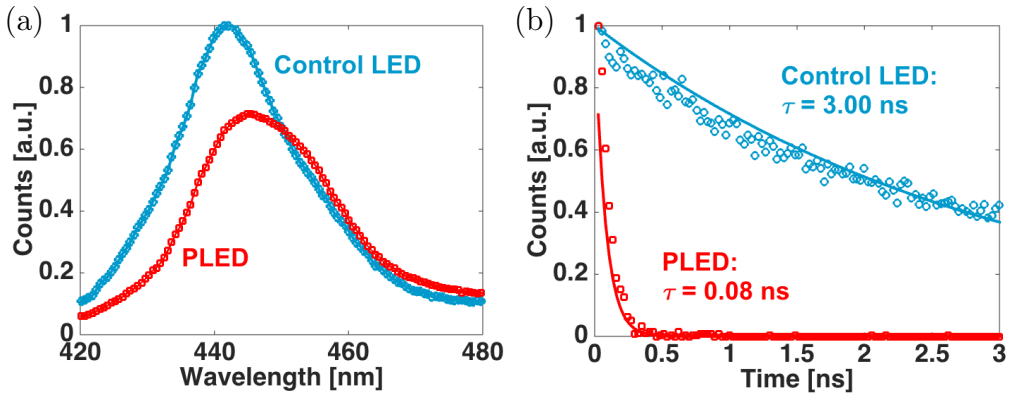

Figure 6.2: Comparison between control LED and PLED. (a) Photoluminescence intensity spectra and (b) time resolved photoluminescence at the vacuum wavelength $\lambda_0 = 450$ nm. In (b), the circles and squares represent experimental data points, while the solid curves are mono-exponential fits to the data.

shown in Fig. B.1 of Appendix B.

The impact of the hole depth on PL intensity is shown in Fig. 6.3, which presents the spatial mapping of PL across the six nanohole gratings. As can be inferred from the color contrast, all the nanostructures provide an enhanced outcoupling compared with the neighboring unpatterned areas. However, the monotonic increase in d_{etch} from the first (grating II) to the last (grating VII) grating results in a non-monotonic PL trend. The intensity is comparable for gratings II, III, and IV, reaches a maximum at grating V, then becomes smaller for gratings VI and VII. The maximum signal detected at

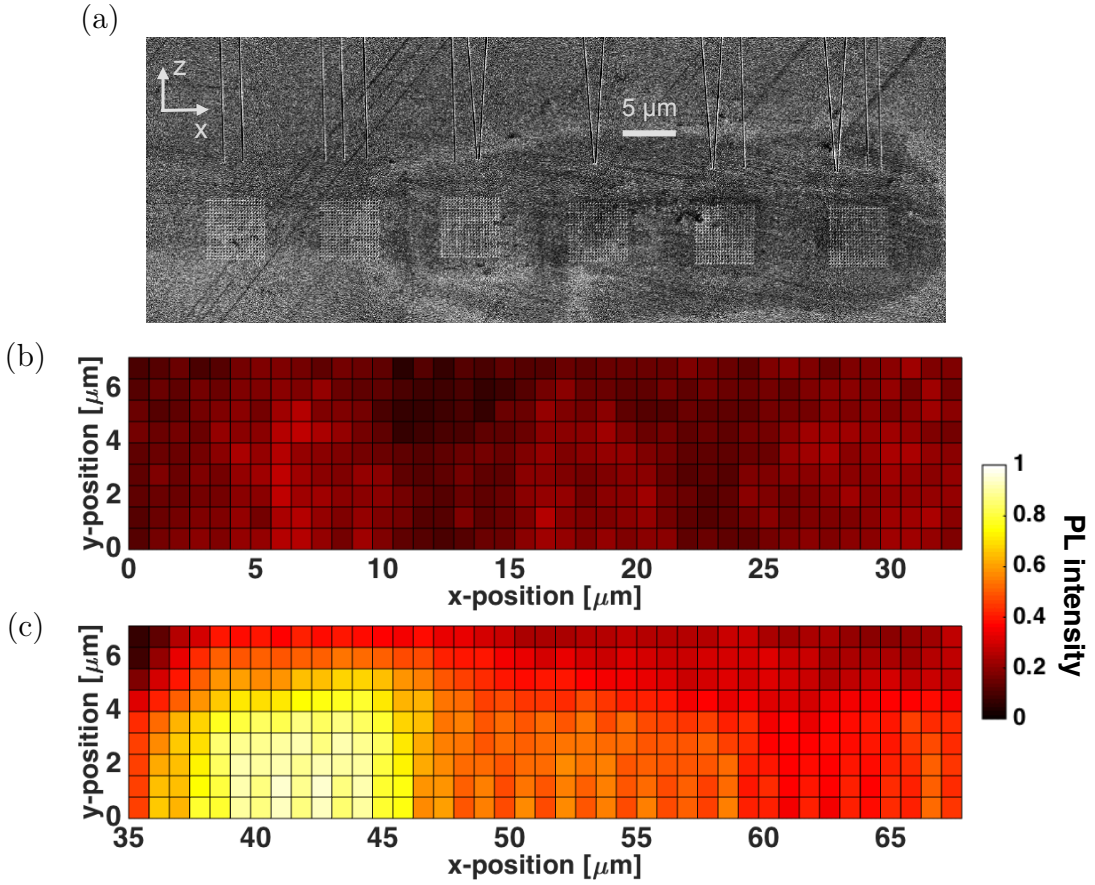

Figure 6.3: PL intensity mapping at $\lambda_0 = 450$ nm of different PLED geometries. (a) SEM image of the six nanohole gratings, milled with increasing hole depth from left to right. (b) Spatially resolved PL intensity of gratings II through IV, and (c) of gratings V through VII. PL intensity is plotted on a logarithmic scale and is normalized to the minimum, which occurs between gratings II and III.

grating V is about 10 times the signal detected away from the gratings on the flat Ag film. To understand the origin of this behavior, and explain how the MQW-nanostructure interaction is controlled by the hole depth, we perform in the next section a structural analysis of the PLED.

6.5 Structural analysis of the plasmonic LED

In order to investigate the correlation between PL intensity and hole depth, we conduct a cross-sectional analysis of the best performing grating (grating V), and of the two gratings with depths immediately smaller and larger (grating IV and VI, respectively). After completing the PL characterization, and repeating it to confirm its result, we deposit a thick (several hundreds of nm) Pt layer on a portion of the grating via the electron-assisted chemical vapor deposition capability of our FIB tool. The function of this coating is twofold: to protect the grating surface during the cut, and to ensure optical contrast with the InGaN/GaN heterostructure by filling the nanoholes. We then define by means of FIB a vertical cross section along the hole diameter. Fig. 6.4(a) shows a back-scattered electrons (BSE) SEM image of the cut portion of grating V, including its surroundings. We observe that, despite a preliminary optimization of the electron deposition current, the larger than 1:1 aspect ratio of the nanoholes forbids Pt from filling them completely. This however does not prevent the identification of their bottom with sufficient accuracy for depth measuring purposes. We also notice that the repeated raster-scanning of the grating area with the two-photon excitation beam caused a progressive damage to the Ag film, manifest both outside of the patterned region, where the Ag film results thinned, and inside such region, where the film has almost completely disappeared. The detail of two cross-sectioned nanoholes of grating V, highlighted by a blue frame in Fig. 6.4(a), is presented in Fig. 6.4(c), sided with an analogous image from grating

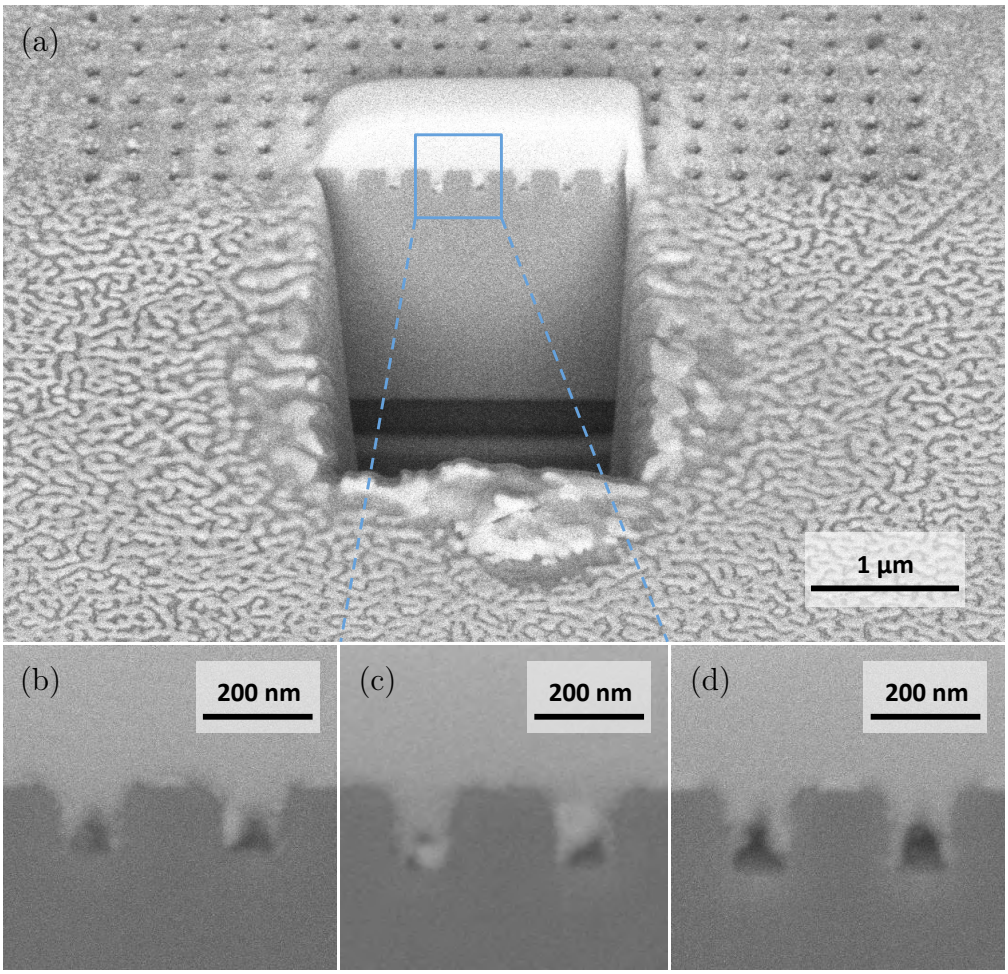

Figure 6.4: (a) BSE SEM image (52° tilt) of a portion of grating V, cross-sectioned via FIB to measure the hole depth. The cut area and its surroundings show the damage caused to the grating region by the PL mapping. A Pt film (bright volume on the grating) was deposited via electron-assisted CVD prior to the cut, to protect the grating surface and ensure optical contrast for the hole cross-section. (b) BSE SEM detail (52° tilt) of the hole cross-section of grating IV, (c) grating V and (d) grating VI. Due to the aspect ratio larger than 1:1, the Pt coating only partially fills the holes, leaving interstices at the bottom.

IV (Fig. 6.4(b)) and one from grating VI (Fig. 6.4(d)). By effect of photoablation, not only on the top surface, but also at the bottom of the nanoholes has Ag either sublimated of melted and reaggregated in small inclusions, as the brightest features in Figs. 6.4(b) and 6.4(c) indicate. For each of the three gratings, we image at 240,000x magnification the cross-sectioned nanoholes, and measure the separation between their bottom and the

pGaN surface. Within the limits imposed by image resolution and contrast, we determine the hole depths of gratings IV, V and VI to be in the range 145-155 nm, 165-175 nm and 180-185 nm, respectively. It is impossible to discern in the BSE SEM pictures the pGaN, MQW and nGaN regions; however, we know that the pGaN thickness is $t_{pGaN} = 130 - 140$ nm, and the MQW thickness is 36 nm (Subsection 6.8.1). Recalling that the Ag film thickness is 20 nm, we conclude that the PL intensity is maximized when so is the overlap between the Ag nanodisk inclusions at the bottom of the holes and the MQW volume.

To gain further insight in our result, we study the MQW-nanostructured plasmonic film coupling by means of 3D FEM simulations (Comsol). The periodicity of the grating is mimicked with periodic boundary conditions. The unit cell of the grating, with side $p_h = 300$ nm, contains a GaN block, patterned with a nanohole with fixed diameter $d_h = 120$ nm and variable depth d_{etch}. The GaN surface and the bottom of the hole are coated with a 20 nm Ag film; the permittivities of GaN and Ag are taken from [248] and [205]. The MQW emission is modeled with an electric dipole, fixed at a vertical distance $d_{es} = 140$ nm from the GaN surface, and at a horizontal distance $d_{eh} = 10$ nm from the hole. To reproduce our experimental study, we progressively vary d_{etch} from a smaller value than d_{es} to a larger one, leaving all the other geometrical parameters unaltered, and collect the power emitted by the dipole-nanostructure system through the bottom of the simulation domain. In analogy with the PL intensity plots of Fig. 6.3, we define radiative enhancement (*RE*) as the collected power normalized to the power detected in the absence of nanostructures, namely for a dipole embedded in a bulk GaN block with a flat Ag film on top. In Fig. 6.5(a), the radiative enhancement is plotted as a function of the hole etching depth d_{etch}. Each data point is obtained from an equally weighted average over the three Cartesian dipole orientations, to account for the isotropic nature of real dipoles [24]. The trend resembles our experimental findings: the largest *RE* is observed at the

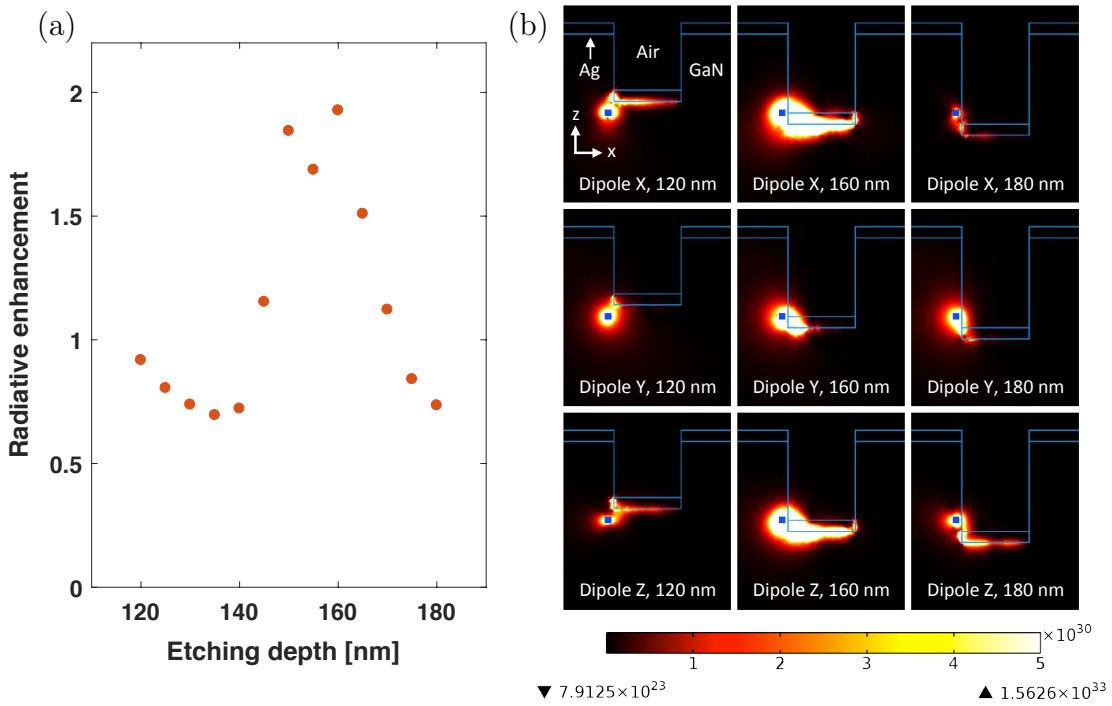

Figure 6.5: Simulated interaction between a quantum emitter (point dipole) and a Ag plasmonic grating in GaN. The hole diameter and pitch ($d_h = 120$ nm, $p_h = 300$ nm), the plasmonic film thickness ($t_{Ag} = 20$ nm) and the emitter position (emitter-GaN surface vertical distance $d_{es} = 140$ nm, emitter-hole horizontal distance $d_{eh} = 10$ nm) are fixed, while the etching depth d_{etch} of the holes is varied across a range of values smaller, equal to and larger than d_{es}. (a) Radiative enhancement as a function of the etching depth of the holes. The values are representative of an isotropic dipole (average over the three Cartesian dipole orientations). (b) Magnitude of the Poynting vector in the xz cross-sectional plane bisecting the unit cell of the grating, for the three Cartesian dipole orientations at selected hole depths ($d_{etch} = 120$, 160, 180 nm). The dipole position is indicated by a blue square.

depths $d_{etch} = 150$, 155 and 160 nm, which maximize the horizontal overlap between the dipole and the Ag nanodisk inclusion. We notice that the magnitude of the enhancement is smaller than the one experimentally detected. This quantitative discrepancy originates from our modeling of the PLED, based on material (permittivity values taken from literature rather than experimentally determined), structural (replacement of the exciton distribution within the entire MQW volume with an individual 1D dipole, and of the LED layers with a homogeneous GaN volume, neglecting the effects of stress and strain and the

perturbation of crystalline order induced by ion milling) and operational (power detection angle limited by the use of a unit cell) approximations. Nonetheless, the qualitative picture confirms and strengthens our result interpretation. Fig. 6.5(b) compares the power distribution of the simulated dipole-nanostructure system at three different etching depths and for the three Cartesian dipole orientations. At $d_{etch} = 120$ nm and $d_{etch} = 180$ nm, when the etching depth is respectively shorter and larger than d_{es}, the emitter-Ag nanodisk coupling is limited. At $d_{etch} = 160$ nm instead, when the nanodisk is next to the dipole, the gain-mode overlap is maximized, resulting in increased emission.

6.6 Discussion

By sorting the device volume in "plasmonic" and "electronic" domains, our PLED design enables a simultaneous increase in modulation speed and output intensity, while still preserving an effective diode structure. Spontaneous emission lifetime, which sets the optical limit for the direct modulation bandwidth (Section 6.2), can be tuned via the hole grating geometry. A shorter lifetime can be achieved with a shorter grating pitch [18]; the diameter does not play a significant role for shallow holes, while for deep ones a larger radius implies a reduced lifetime [251]. Interdependence exists, however, between the grating geometry and the pGaN layer thickness. As we saw in Section 6.3, t_{pGaN} needs to be at least larger than the depletion width of the LED, in order to grant a satisfactory carrier injection into the MQW. On the other hand, despite our design decouples the "plasmonic" and "electronic" volumes, an arbitrary increase in t_{pGaN} faces nanofabrication limitations. We demonstrated indeed that, to maximize light extraction, the nanoholes need to reach down to the MQW and etch slightly through it, so that the nanostructured plasmonic film spatially overlaps with the emitting region. By constraining the hole depth, t_{pGaN} imposes a practical limit also on the hole diameter

and pitch. Depth:diameter aspect ratios larger than 1.5:1 make it progressively harder to ensure the structural integrity of the grating (i.e. to define straight hole walls and sharp edges, which becomes critical as the pitch is decreased since nearest neighbor holes can collapse into each other) and the filling of the nanoholes with plasmonic inclusions. Therefore, the balance between modulation bandwidth, internal quantum efficiency and injection efficiency of the PLED can be controlled with the above-discussed parameters, keeping in mind their strong interplay.

In order to enable direct current modulation, electrical contacts with a ground-signal-ground (GSG) topology, supporting high-speed operation through the minimization of capacitive effects, need to be integrated in the PLED. Our choice of a transparent sapphire substrate (Subsection 6.8.1) allows light emission from the bottom of the PLED chip: therefore, a Au pGaN contact can be deposited on top of the plasmonic grating, and further increase radiation extraction by acting as a mirror. Alternatively, a transparent indium tin oxide (ITO) contact can be adopted if top emission is preferred. Whatever the case, a concern negligible for optical MQW pumping but not for the electrical one must be addressed. If a contact is deposited directly on the plasmonic grating, the filled holes volume becomes a preferential path for current, due to its larger conductivity compared to pGaN. The poor injection efficiency of the "electronic" regions and the shorting of the "plasmonic" ones hamper the functioning of the PLED. A remedy consists in coating a thin (few nm) oxide insulation layer inside the nanoholes prior to the plasmonic film deposition. In this way, the Ag inclusions still overlap horizontally with the MQW volume, but the current flow is confined to the "electronic" regions with a proper diode structure. To obtain a conformal protection of the bottom and the internal walls of the nanoholes, a SiO_2 or Al_2O_3 layer can be grown by atomic layer deposition. This step however needs to be followed by directional dry etching of the surface of the PLED, to remove the oxide coating from the top of the "electronic" regions which otherwise cannot

be effectively contacted.

An alternative approach to the integration of plasmonic nanostructures in InGaN/GaN LEDs, experimentally explored in [249], consists in inserting Ag nanoparticles into the LED structure. The inconvenience of this method is that it requires breaking the vacuum in the growth chamber to e-beam evaporate the metallic particles, which can result in the incorporation of impurities within the heterostructure. In addition, the roughness induced by the particles propagates to the upper layers grown on top of them, with obvious consequences for the lattice cristallinity both in the MQW and in the pGaN. Our design instead preserves the planarity of the LED structure, and utilizes a plasmonic grating whose geometry can be accurately and reproducibly controlled. In view of mass producing the PLED, low throughput techniques such as FIB (which can also cause ion implantation in the LED crystal lattice) or e-beam lithography are not a convenient choice to inscribe a nanohole grating. Large-scale, large-area alternatives, such as nanoimprint lithography (NIL) or direct laser writing lithography [252] are to be preferred.

The PLED design detailed in this work enables the implementation of blue LED transmitters in VLC systems. To increase the number of wavelength channels, it is either possible to engineer the InGaN emission (limitedly to the UV-blue-green spectral region) or to resort to a different semiconductor platform (for the red-infrared region). However, owing to its fixed plasmonic properties, Ag effectively enhances the modulation bandwidth only at blue frequencies. Substitution of the Ag thin film with a multilayer hyperbolic MM allows tuning the wavelength of maximum lifetime reduction across the rest of the light spectrum. For example, a Ag/Si multilayer red-shifts the plasmonic resonance monotonically with the amount of Si, allowing peak bandwidth enhancements at green and red frequencies [18, 19].

6.7 Conclusions

The present work introduced a novel plasmonic LED design that combines a blue InGaN/GaN LED with a nanostructured film, consisting of a nanohole grating coated with a thin Ag layer. By decoupling the device volume into "plasmonic" and "electronic" regions, the PLED is simultaneously capable of increased modulation speed, compared to a conventional LED, and increased light output, compared to a plasmonic LED with a flat Ag film, while preserving an effective p-n junction structure. In order to optimize light extraction, we fabricated six plasmonic gratings with identical pitch and hole diameter, and variable hole depth. Time-resolved photoluminescence measurements at the peak emission wavelength $\lambda_0 = 450$ nm predicted an almost 40-fold enhancement in the limit 3dB bandwidth for all the gratings. A spatial mapping of the PL intensity at $\lambda_0 = 450$ nm, combined with a cross-sectional analysis of the fabricated structures, revealed that light extraction is maximized when the Ag nanodisk inclusions inside the holes overlap with the MQW volume, rather than sitting above or below it. This finding is corroborated by 3D numerical simulations, showing an identical trend for a dipole-plasmonic nanohole system. We discussed the mutual influence between the pGaN thickness and the grating geometrical parameters, and how the introduction of an insulation layer inside the nanoholes is required to enable effective electrooptical performance. Our study paves the way for a practical implementation of plasmonically-enhanced high-speed, high-efficiency incoherent sources in VLC systems. Future work will include the design, optimization and testing of electrical contacts suitable for high-speed modulation. We will also extend the PLED design to green and red wavelengths by replacing the Ag film with a properly chosen multilayer hyperbolic MM.

6.8 Methods

6.8.1 LED growth

The GaN LED was grown on a double side polished (DSP) c-sapphire wafer, of diameter 2 in and thickness 300 μm, with a 3 x 2-in Thomas Swan/Axitron close-coupled showerhead (CCS) metal-organic chemical vapor deposition (MOCVD) system. The LED structure, from the substrate upwards, consists of a 1 μm undoped GaN buffer layer and a 600 nm Si-doped nGaN layer ($n \approx 6 \times 10^{18}$ cm^{-3}), followed by 3 InGaN/undoped GaN (2 nm / 10 nm) quantum well/quantum barrier (QB) layers. The MQW active region is capped with a Mg-doped pGaN layer ($p \approx 5 \times 10^{17}$ cm^{-3}), whose thickness varies between 130 and 140 nm. The growth temperature of the InGaN layer was adjusted to 730°C to tune the emission wavelength to about 450 nm. The sample was annealed inside the MOCVD chamber at 750°C under N_2 flow to activate the pGaN.

6.8.2 Patterning of plasmonic grating

After a 10 nm Ni sacrificial mask was coated by e-beam evaporation (Temescal BJD 1800, rate = 2 Å / s) to protect the LED surface, six 6 μm x 6 μm gratings were patterned on the LED with a focused ion beam system (FEI Scios DualBeam FIB/SEM). Each grating consists of a 20 x 20 array of holes, with pitch 300 nm and hole diameter 120 nm, etched with a Ga ion beam at a voltage of 30 kV and a current of 1.5 pA. What differentiates the gratings is the hole etching depth, varied from values smaller to larger than the pGaN layer thickness. Once the patterning was complete, the Ni mask was wet etched in Ni etchant, and a Ni adhesion layer (2 nm, rate = 0.2 Å / s) followed by a Ag plasmonic film (20 nm, rate = 0.5 Å / s) was deposited on the gratings by e-beam evaporation.

6.8.3 Static photoluminescence

The PL spectra of Fig. 6.2(a) were measured with a micro-PL system. The excitation light, generated by a mercury lamp (X-cite 120 Q), was filtered at 405 nm (405/10 nm bandpass filter, Semrock Brightline) and focused on the sample. The emitted light was collected with a 50x, 0.55 NA objective (Zeiss Epiplan Neofluar) and spectrally analyzed by a Czerny-Turner spectrograph (Andor Shamrock 303i): after entering a 20 μm aperture, radiation was spatially separated by a blazed diffraction grating (150 lines/mm, blaze wavelength $\lambda_b = 500$ nm), and detected with a charge-coupled device (CCD) camera (Andor Newton). A dichroic beam splitter (405 nm, Semrock Brightline) and a long-pass filter (409 nm, Semrock Brightline) ensured that the portion of the excitation light reflected off the sample was removed from the analyzed signal.

6.8.4 Spatio-temporally resolved photoluminescence

Spatially and temporally-resolved PL was measured by first illuminating the sample with a femtosecond Ti:sapphire laser (Spectra Physics Mai Tai) of 800 nm wavelength, 80 MHz repetition rate, and 100 fs pulse width. Due to two-photon absorption, the sample fluoresced at wavelengths between 400 and 500 nm. Fluorescence at the emission wavelength of 450 nm was collected through the bottom of the sample with a 20x, 0.45 NA objective, then sent to a monochromator (Horiba) and finally detected with an electrically cooled photo-multiplier tube (PMT). The Ti:sapphire laser was synched (TB-01 Pulse Converter Module) with a time-correlated single-photon detector (Horiba High Throughput TCSPC controller) providing 27 ps timing resolution. The beam position relative to the sample was controlled by moving the sample stage with a two-axis piezo-electric motor (Mad City Labs NanoDrive) with an 800 nm step size. Alignment of the pump beam and sample was achieved with a microscope (Olympus 1X81) and a

complementary metal-oxide-semiconductor (CMOS) camera (μEye).

Chapter 6, in part, is being prepared for submission for publication. L. Ferrari, J. S. T. Smalley, H. Qian, A. Tanaka, D. Lu, S. Dayeh, Y. Fainman and Z. Liu, "Design and analysis of blue InGaN/GaN plasmonic LED for high-speed, high-efficiency optical communications". The dissertation author is the co-first author of this paper.

Chapter 7

Summary and future directions

7.1 Thesis summary

The present thesis discussed theoretical and experimental avenues to enhance light-matter interaction in hyperbolic metamaterials, with the ultimate goal to ease the integration of such artificial media into high-speed optical communication systems.

We first framed our study into a comprehensive background, where the unique properties of HMMs, derived from their anisotropic optical dispersion, were detailed. We saw how the ability of HMMs to support large wavevectors and manipulate the near-field enables several applications, including high-resolution imaging and lithography, broadband absorption engineering, thermal emission engineering and spontaneous emission engineering. We then narrowed our focus on the latter, in light of its relevance for optical communications, and addressed key challenges for the inclusion of hyperbolic media into optical transmitters.

Firstly, we observed that the Purcell factor of ML HMMs, which quantifies emission speed enhancement, is smaller compared to the plasmonic one. To compensate for this gap, we proposed to move the emitter inside the hyperbolic medium, therefore

maximizing the accessible photonic density of states. By means of numerical simulations, previously validated with an analytical model, we determined the evolution of Purcell enhancement when a dipole emitter is gradually moved from the outside to the inside of a Ag/Si ML HMM. We found that, for an emitter inside the ML, the Purcell factor reaches a maximum of almost 300 at $\lambda_0 = 554$ nm. This value is 3 times larger than the peak value for an outer emitter, and about 1.4 times larger than the Purcell factor of a plasmonic Ag film. Large wavevector extraction in the far-field was achieved by means of a rectangular and a triangular 1D grating, obtaining a peak radiative enhancement of about 6-fold and 10-fold, respectively.

Secondly, we highlighted how gratings do not allow an efficient outcoupling of large-*k* waves from HMMs, due to their scarce directional control. In addition, we pointed out that the low throughput of standard grating nanofabrication techniques, such as e-beam lithography and focused ion beam milling, hampers the scalability of hyperbolic technology to commercial volumes. We mitigated the first inconvenience by shaping the hyperbolic medium into a nanoantenna. We studied the spatial dependence of the Purcell factor and the radiative enhancement of a point emitter coupled with a Ag/Si ML cylindrical antenna, and observed that a wavelength-dependent directional emission is achieved for a fixed emitter position. We then adopted an even more radical approach, and achieved large wavevector outcoupling through a new method that exclusively leverages dispersion engineering. Design guidelines were provided to extract radiation from the top or from the side of unpatterned hyperbolic media, either with Type I or Type II dispersion. Accounting for loss resulted in preferential side extraction for ML HMMs, and top extraction for NW HMMs. We determined the outcoupled large-*k* bands for effective media based on Ag/Si and Ag/SiO_2 MLs, respectively at $\lambda_1 = 530$ nm and $\lambda_2 = 470$ nm. By means of numerical simulations, we compared the performance of an optimized and an unoptimized HMM block coupled with a point emitter, observing an

almost 40-fold increase in lateral power extraction. When loss was artificially reduced to 1% of its value, the increase reached 3 orders of magnitude.

Finally, the design of an electrically controlled plasmonic optical transmitter was experimentally studied. We proposed a novel plasmonic LED architecture, integrating a Ag nanostructured film into an InGaN/GaN LED, which enables simultaneous high-speed modulation and efficient light emission, while preserving effective electrical excitation. We fabricated different PLED structures operating at $\lambda_0 = 450$ nm, and characterized them with spatio-temporally resolved photoluminescence. A limit 2 GHz modulation bandwidth was predicted based on lifetime measurements. Through careful optimization of the plasmonic nanostructure, we demonstrated a 10-fold increase in outcoupling efficiency relative to a flat plasmonic film. A cross-sectional analysis clearly related the measured enhancement to a specific nanostructure geometry; the experimental result was further consolidated by numerical simulations. By bridging the plasmonic metamaterial and the III-nitride semiconductor communities, this study laid the groundwork for high-speed, high-efficiency plasmonic LEDs for applications in visible light communication.

7.2 Future directions

The material presented in this dissertation offers several opportunities for further research, both by itself and in combination with other topics. We discussed in Chapter 3 how moving an emitter from the outside to the inside of a ML hyperbolic medium can significantly enhance the Purcell factor. Experimental verification of this theoretical study is relatively immediate at telecommunication wavelengths, by incorporating inside a ML stack an active layer of doped glass or ceramics [253, 254]. The situation is more complex at visible frequencies, due to the lack of emitters easily integrable within a ML. The introduction of spherical luminescent nanoparticles, such as metallic clusters [255]

or quantum dots [209, 256], affects the quality of the layers deposited on top of them, as evidenced by transmission electron microscope (TEM) images [256]. A better alternative consists in growing a metallic quantum well. Besides preserving the integrity of the ML, this approach synthesizes in a single nanofabrication step (e.g. sputtering) both the ML and the emitter, without breaking the vacuum and introducing impurities between layers. If, in addition, the ML dispersion was designed following the prescriptions of Chapter 5, the maximized Purcell enhancement would be combined to lateral large-k extraction without the need of a grating.

In Chapter 5, we emphasized how our novel outcoupling paradigm based on dispersion engineering applies to any medium with hyperbolic permittivity components. Originating from the traditional ML and NW configurations, new structures are appearing or will appear in the incoming years that still display hyperbolic dispersion, but with characteristics that can alter or enrich the classification of Table 5.1, and therefore increase the versatility of our model. Hybrid ML-NW composites, generically termed "photonic hypercrystals"[14, 256], might be homogenized with novel effective parameters, with a different poles and zeroes distribution from pure MLs or NWs. Quantum hyperbolic metamaterials with atomic-thin layers might display reduced loss, and their permittivity will depend not only on filling ratio and temporal frequency, but also on spatial frequency.

In demonstrating the use of dispersion outcoupling for emitter-HMM systems, we focused on a ML HMM for lateral extraction. Analogous analysis can be extendedly performed for a NW HMM, which is predicted to enable top outcoupling. This feature is optimal for the optical transmission of information, but has also another attractive implication. HMMs naturally enable a superior control of near-field radiative heat transfer, known to exceed Planck's blackbody limit by orders of magnitude [53, 257]. The normal extraction of large-k waves from a thermal NW film, made for instance of ITO nanowires in air [258] or W nanowires in an Al_2O_3 template [259], can enhance the conversion

efficiency of thermophotovoltaic (TPV) cells [259], and boost the performance of energy systems, radiative coolers, thermal switches and rectifiers [258].

The study completed in Chapter 6 provides a clear guideline for the geometric optimization of the plasmonic LED. Since the ideal hole depth for power extraction is now known, future analysis should fix this parameter and systematically elucidate the dependence of lifetime - i.e. of limit 3dB modulation bandwidth - on hole diameter and pitch. In view of the direct electrical modulation of the PLED, three interdependent aspects of the device architecture need to be addressed. First, electrical contacts for high-speed RF signals must be designed to maximize the current injection in the plasmonically enhanced region, while simultaneously minimizing parasitic capacitance effects, which curb the modulation bandwidth. Second, a heat sink must be integrated. Heat build-up degrades the PLED performance by quenching internal quantum efficiency [260] or by causing permanent damages to the plasmonic nanostructure, similar to those observed in our analysis (Fig. 6.4). Third, a device lifetime longer than few months must be ensured by conveniently packaging the PLED, thereby insulating its semiconducting crystalline lattice and its metallic nanostructure from moisture and oxygen. The static and dynamic performance of the PLED should be quantified by measuring its light-current-voltage characteristic (L-I-V curve) and its frequency response.

The density of information of a monochromatic PLED channel can be increased by encoding in the emitted light two different polarizations. To this end, the plasmonic grating can be replaced with chiral plasmonic metasurfaces, patterned with spiral features that induce a right-handed or a left-handed circular polarization [261, 262, 263]. Compared with linear polarization, circular polarization exhibits a higher degree of persistence in scattering environments [264], and is therefore more suited for visible light communication. Not only spin angular momentum (right- or left-handedness) can be encoded with plasmonic metasurfaces, but also and most importantly orbital angular

momentum (OAM), related to the helicoidal shaping of the emitted wavefront [265]. OAM is associated with a quantum number which can assume any integer value from 0 to infinity, providing for a given light frequency a number of information channels in principle unlimited.

The use of a Ag nanostructure limits the applicability of our PLED design to blue light emission. A similar "hyperbolic LED" (HLED) architecture, employing ML or NW hyperbolic media in place of plasmonic films, will extend the concept of plasmonically enhanced LED to the rest of the visible range and to the infrared. While emission at visible frequencies finds application in Li-Fi local and extended networks, smart cities based on the Internet of Things (IoT), underwater optical communications and wireless medical devices, HLEDs at telecommunication wavelengths are poised to significantly impact the data center infrastructure. In a data center environment, on-chip connectivity is ensured by Si photonics, which routes optical signals between transceivers by means of waveguides; rack-to-rack and longer distances are instead covered by fiber-optics technology. There exists however a bottleneck at the intermediate chip-to-chip connectivity scale, that cannot be addressed by neither of the previous approaches. Chip-to-chip communications cannot be implemented with waveguides, too inefficient to cover distances of the order of millimeters/centimeters; the use of optical fibers is equally impractical, because it severely limits the escape bandwidth density. Infrared HLEDs are promising candidates to bridge this gap between connectivity scales, although they face the competition of alternative solutions [266].

We finally predict that major efforts will be invested in the incoming years to achieve and control stimulated emission from HMMs. Compared with the narrow bandwidth of resonance of plasmonic lasers, hyperbolic lasing exhibits a broadband character, which facilitates coupling with a wide variety of active media. Recent experimental demonstrations, based on a MgF_2/Ag ML [267] or on Au NW [268] coated with laser

dyes, also suggest that HMMs allow a lower threshold than plasmonic films [267] or elliptic metamamaterials [268], but the relative contribution of the surface and the bulk of the hyperbolic medium to lasing still needs to be clearly identified. Further experimental study in conjunction with theoretical modeling is to be expected.

Appendix A

Hyperbolic dispersion optimization for directional light extraction

The present appendix provides the theoretical foundation of the model presented in Chapter 5, together with a 3D study of the QD-HMM system therein discussed. In addition, it contains the effective parameters plot of the Ag/Si and Ag/SiO_2 MLs, and the dispersion of the Ag/Si effective medium at $\lambda_1 = 530$ nm, plotted for both the optimized and the unoptimized filling ratios.

A.1 Limit cases of hyperbolic dispersion

A hyperbola in the *xz* plane with center in the origin and vertices on the x axis is described by the equation

$$\frac{x^2}{a^2} - \frac{z^2}{b^2} = 1, \tag{A.1}$$

where *a* (semi-major axis) is the distance between a vertex and the origin, and *b* (semi-

minor axis) is the distance between a vertex and the asymptote above (or below) it. While a alone determines the separation of the hyperbola branches from the z axis, by defining the coordinates of the vertices $(x,z) = (\pm a, 0)$, the ratio of b to a controls the curvature of the branches at the vertices. The latter is expressed in terms of the eccentricity

$$e = \sqrt{1 + \left(\frac{b}{a}\right)^2}, \tag{A.2}$$

a positive quantity with limiting values of 1 to $+\infty$. These extreme values are reached by

$$\lim_{\frac{b}{a}\to 0^+} e = 1, \qquad \lim_{\frac{b}{a}\to +\infty} e = +\infty, \tag{A.3, A.4}$$

corresponding to cases of maximal and minimal curvature, respectively.

Let us consider a lossless HMM of Type II ($\varepsilon_{zz} > 0$ and $\varepsilon_{\perp} < 0$). Its dispersion is described by Eq. (A.1), provided that the following substitutions are made:

$$\begin{aligned} x &\to k_x/k_0 \qquad & a^2 &\to \varepsilon_{zz} \\ z &\to k_z/k_0 \qquad & b^2 &\to |\varepsilon_{\perp}|, \end{aligned} \tag{A.5}$$

For top outcoupling, k_x is conserved, and large $k_{HMM,z}$ components can be extracted (Fig. 5.3(c) of Chapter 5). Following Chapter 5, we restrict our analysis to the $(k_x > 0, k_z > 0)$ quadrant. The limit case in which an infinite band of waves propagating within the HMM is converted to propagating waves in air occurs when two conditions are simultaneously verified: the branches of the hyperbola must be "straightened" until their curvature at the vertices vanishes and they align with the z axis, and "squeezed" along the x axis, until the vertex coordinate a becomes < 1. The first requirement ensures the infinite extension of the band, the second forces all the k_x components of the band to

be identical to a certain $\bar{k}_x < k_0$. This, by virtue of Eq. (5.5), preserves the propagating nature of all the k-vectors in the band across the HMM-air interface. It also implies a vanishing angular spread in the emission, as all the waves in the HMM are refracted into air only at one specific angle with the z axis, $\bar{\theta}_{air} = \arctan(\bar{k}_x/\sqrt{k_0^2 - \bar{k}_x{}^2})$. Squeezing is maximized when $\bar{k}_x = 0$: in that case, the two straight branches collapse onto the z axis, $\bar{\theta}_{air} = 0$ and the emission is orthogonal to the interface. The band edges $\mathbf{k}_{HMM,1}$ and $\mathbf{k}_{HMM,2}$ and the vector $\mathbf{k}_{HMM,sep}$ separating the short- and large-k constituents of the band (cfr. main text) have zero x components, and z components $k_{HMM,1\,z} = 0$, $k_{HMM,2\,z} = +\infty$ and $k_{HMM,sep\,z} = k_0$.

The simultaneous requests of infinite bandwidth (i.e. maximal straightening, or vanishing curvature at vertices) and normal emission (i.e. maximal squeezing, or vertices coinciding with the origin), are formulated by means of Eq. (A.2) and (A.4) as follows:

$$\begin{cases} \frac{b}{a} \to +\infty \\ a \to 0^+ \end{cases} \quad \underset{\text{(A.5)}}{\Longleftrightarrow} \quad \begin{cases} \sqrt{\frac{|\varepsilon_\perp|}{\varepsilon_{zz}}} \to +\infty \\ \sqrt{\varepsilon_{zz}} \to 0^+. \end{cases} \tag{A.6}$$

We look for physical solutions of the system, namely finite or vanishing values of $|\varepsilon_\perp|$ and ε_{zz}. The second equation demands that, at a fixed frequency $\bar{\omega}$, the filling ratio ρ take a value $\bar{\rho}$ such that $\varepsilon_{zz}(\rho) \to 0^+$ as $\rho \to \bar{\rho}$. The first equation is simultaneously satisfied if, as $\rho \to \bar{\rho}$, $|\varepsilon_\perp(\rho)|$ either approaches a finite value $|\varepsilon_\perp(\bar{\rho})|$ or approaches 0 less quickly than $\varepsilon_{zz}(\rho)$ does: in mathematical terms, $\varepsilon_{zz}(\rho) = o(|\varepsilon_\perp(\rho)|)$ as $\rho \to \bar{\rho}$.

For side outcoupling, k_z is conserved, and large $k_{HMM,x}$ components can be extracted (Fig. 5.3(d) of Chapter 5). Restricting our analysis to the $(k_x < 0, k_z > 0)$ quadrant, the band edges $\mathbf{k}_{HMM,1}$ and $\mathbf{k}_{HMM,2}$ and the separation vector $\mathbf{k}_{HMM,sep}$ are redefined as the intersections of the hyperbolic dispersion respectively with the x axis, the straight line $k_z \equiv k_0$ and the circular dispersion of air. In the considered configuration, both

maximal straightening and maximal squeezing are accomplished by solely requesting that the curvature at vertices be infinity: by means of Eq. (A.2) and (A.3), this reads

$$\frac{b}{a} \to 0^+ \qquad \underset{\text{(A.5)}}{\Longleftrightarrow} \qquad \sqrt{\frac{|\varepsilon_\perp|}{\varepsilon_{zz}}} \to 0^+. \tag{A.7}$$

Eq. (A.7) is satisfied when, at a fixed frequency $\bar{\omega}$, the filling ratio ρ takes a value $\bar{\rho}$ such that $|\varepsilon_\perp(\rho)| \to 0^+$ and $|\varepsilon_\perp(\rho)| = o(\varepsilon_{zz}(\rho))$ as $\rho \to \bar{\rho}$ (we discarded the unphysical solution $\varepsilon_{zz}(\rho) \to +\infty$, and $|\varepsilon_\perp(\rho)| \to |\varepsilon_\perp(\bar{\rho})|$ finite or $|\varepsilon_\perp(\rho)| \to +\infty$ slower than $\varepsilon_{zz}(\rho)$). The latter condition implies that $\varepsilon_{zz}(\rho)$ either approaches 0 less quickly than $|\varepsilon_\perp(\rho)|$ does, or approaches a finite value $\varepsilon_{zz}(\bar{\rho})$. In the first case, $\mathbf{k}_{HMM,1}$, $\mathbf{k}_{HMM,sep}$ and $\mathbf{k}_{HMM,2}$ have zero z components, and x components $k_{HMM,1\,x} = 0$, $k_{HMM,sep\,x} = k_0$ and $k_{HMM,2\,x} = +\infty$. In the second case, all the z components remain zero and it is still $k_{HMM,2\,x} = +\infty$, but $k_{HMM,1\,x} = \sqrt{\varepsilon_{zz}(\bar{\rho})}k_0$ and $k_{HMM,sep\,x}$ depends on $\varepsilon_{zz}(\bar{\rho})$: if $\varepsilon_{zz}(\bar{\rho}) \leq 1$, $k_{HMM,sep\,x} = k_0$, while if $\varepsilon_{zz}(\bar{\rho}) > 1$ $k_{HMM,sep\,x}$ and therefore $\mathbf{k}_{HMM,sep}$ do not exist, as the hyperbolic and circular dispersions do not intersect (outcoupled band exclusively composed of large-k waves).

Let us now consider a lossless HMM of Type I ($\varepsilon_{zz} < 0$ and $\varepsilon_\perp > 0$). By means of the substitutions

$$\begin{aligned} x &\to k_x/k_0 \qquad & a^2 &\to -|\varepsilon_{zz}| \\ z &\to k_z/k_0 \qquad & b^2 &\to -\varepsilon_\perp, \end{aligned} \tag{A.8}$$

we can rewrite Eq. (A.1) as

$$-\frac{x^2}{a'^2} + \frac{z^2}{b'^2} = 1, \tag{A.9}$$

where we renamed

$$|\varepsilon_{zz}| \to a'^2 \qquad \varepsilon_\perp \to b'^2. \tag{A.10}$$

Eqs. (A.8), (A.9) and (A.10) describe a dispersion of Type I. The change of signs in the left side of Eq. (A.9) corresponds to a 90° rotation of the hyperbola, whose vertices now lie on the z axis. Identical considerations to those just discussed for Type II therefore apply to Type I, keeping in mind that the behavior of top and side outcoupling is now swapped by cause of the rotation. For top outcoupling, an infinite bandwidth of k-vectors is orthogonally extracted through the top HMM-air boundary when, at fixed $\bar{\omega}$, the filling ratio ρ takes a value $\bar{\rho}$ such that $|\varepsilon_{zz}(\rho)| \to 0^+$ and $|\varepsilon_{zz}(\rho)| = o(\varepsilon_\perp(\rho))$ as $\rho \to \bar{\rho}$. For side outcoupling, an infinite bandwidth of k-vectors is orthogonally extracted through the side HMM-air interface, for a given $\bar{\omega}$, at $\bar{\rho}$ such that $\varepsilon_\perp(\rho) \to 0^+$ and $\varepsilon_\perp(\rho) = o(|\varepsilon_{zz}(\rho)|)$ as $\rho \to \bar{\rho}$.

A.2 Quantum dot-HMM coupling: 3D study

In the present appendix we extend the analysis of the QD-HMM system performed in Section 5.5 to a full 3D simulation environment. As the dimensionality increases, so do memory requirements, imposing a concomitant decrease of the domain size if the computational time is to remain finite. We therefore consider a block of HMM with identical height to the 2D structure ($l_z = 200$ nm), but with shortened width coincident with the length $l_x = l_y = 300$ nm. To maximize the analogy with the 2D case, we locate a point dipole emitting at λ_1 5 nm below the center of the bottom surface, so that its distance from each lateral surface is 150 nm. The power emitted through a lateral face is collected into a spherical cap coaxial with $\hat{\mathbf{x}}$ (for the faces parallel to the yz plane) or $\hat{\mathbf{y}}$ (for the faces parallel to the xz plane), with vertex in the center of the face and aperture

$\theta = 30°$. Symmetry reduces all the dipole-lateral face permutations to 3 geometries: X-dipole, power outcoupled through face yz ($P_{X,yz}$); X-dipole, power outcoupled through face xz ($P_{X,xz}$); and Z-dipole, power outcoupled through any of the lateral faces (P_Z).

We first model the Si/Ag HMM as an effective medium. The powers $P_{X,yz}$ and P_Z at the optimized filling ratio ρ_B are respectively 4 and 31 times larger than at the unoptimized filling ratio ρ_A, a proportion close to that of the correspondent 2D enhancements (Section 5.5). The power $P_{X,xz}$, which lacks of a 2D counterpart, results comparable for the two filling ratios. The lateral power extraction for a Z-dipole coupled to an EMT block with filling ratio ρ_B is visualized in Fig. A.1.

In order to further investigate the dipole-HMM interaction for practical HMM realizations, we replace the effective medium with a ML structure. The layered stack contains 10 Ag/Si periods of length $L = 20$, for a total height $l_z = 200$ nm, and has a width coincident with the length $l_x = l_y = 300$ nm, so that the block size remains unchanged. In this case, both the collected powers $P_{X,yz}$ and $P_{X,xz}$ are comparable for

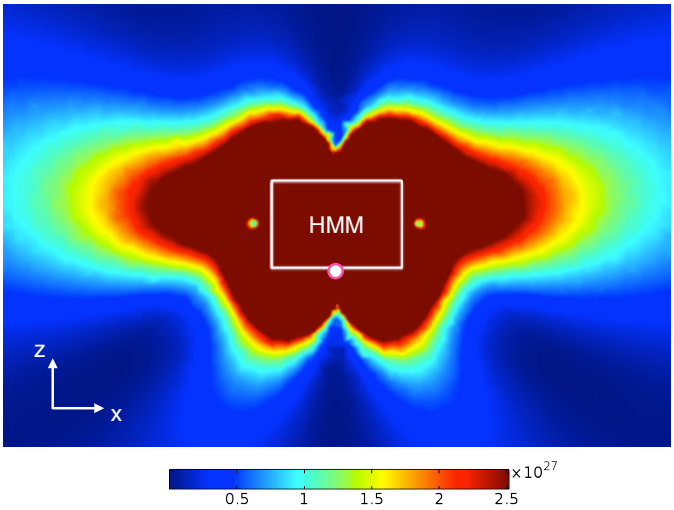

Figure A.1: Spatial power distibution (magnitude of the Poynting vector) in the cross-sectional plane $y = 0$ of a Z-dipole 5 nm below a 3D block of Ag/Si effective medium in air. The dipole, whose location is indicated by a pink-bordered white dot, emits at $\lambda_1 = 530$ nm. The effective medium parameters correspond to the optimized filling ratio $\rho_B = 0.58$.

ρ_A and ρ_B, whereas P_Z is 6 times larger at ρ_B than at ρ_A. The quantitative difference with the effective medium result can be understood by recalling that EMT overestimates the power coupled from a dipole into a HMM [153]. Lateral extraction, both for the effective and the layered medium, is best achieved with a Z-dipole, which compared to an X-dipole exhibits a stronger coupling to a HMM [145, 217]. Fig. A.2 compares the far-field radiation patterns of a Z-dipole-ML block system at unoptimized and optimized filling ratios. At ρ_B, a dominant horizontal emission is generated by side outcoupling (upper lobe), accompanied by scattering from the lower block edges closer to the dipole (lower lobe). At ρ_A instead, two lobes symmetrically departing from the dipole-ML block system indicate that the main light extraction mechanism is scattering from the upper and lower edges of the block, rather than outcoupling from the lateral faces.

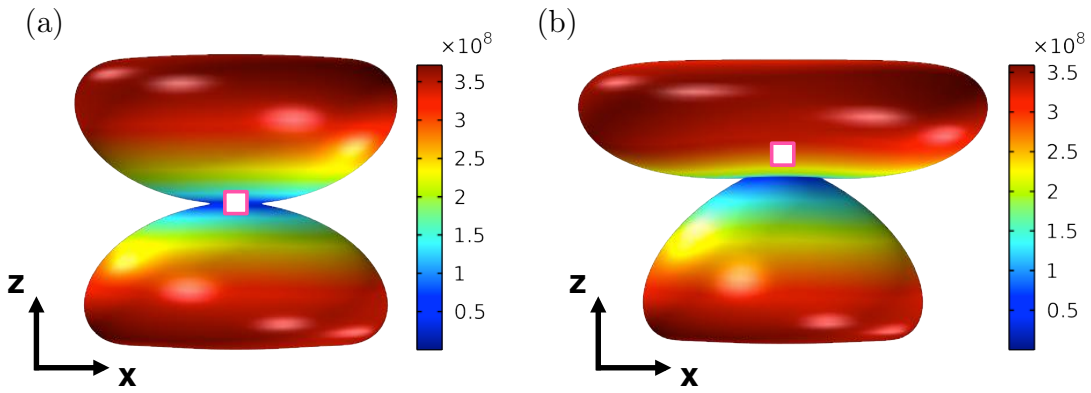

Figure A.2: Far-field emission pattern (electric far-field norm) at $\lambda_1 = 530$ nm of a Z-dipole 5 nm below a 3D block of Ag/Si layered medium in air. (a) Filling ratio $\rho_A = 0.54$; (b) filling ratio $\rho_B = 0.58$. The pink-bordered white square indicates the position of the dipole-ML block system with respect to the emission pattern.

A.3 Additional plots for the Ag/Si and Ag/SiO_2 systems

Fig. A.3 shows the real and imaginary parts of the effective components for the Ag/Si and Ag/SiO_2 MLs discussed in the main text. Since the losses associated

to the Re{$\varepsilon_\perp$}-near-zero region are low, it is possible to achieve side outcoupling. A Re{ε_{zz}}-near-zero region is also present, but it corresponds to a resonant pole of Eq. (5.3): the related high loss prevents effective top outcoupling.

Fig. A.4 compares the effective medium dispersion of the Ag/Si ML discussed in the main text at two filling ratios $\rho_A = 0.54$ and $\rho_B = 0.58$. In both cases the effective medium exhibits a Type I behavior, distorted from the ideal case of Fig. 5.3(b) by the presence of loss; however, at ρ_A the portion of laterally outcoupled large-k waves is negligible, whereas at ρ_B, optimized for lateral extraction, the outcoupled large-k

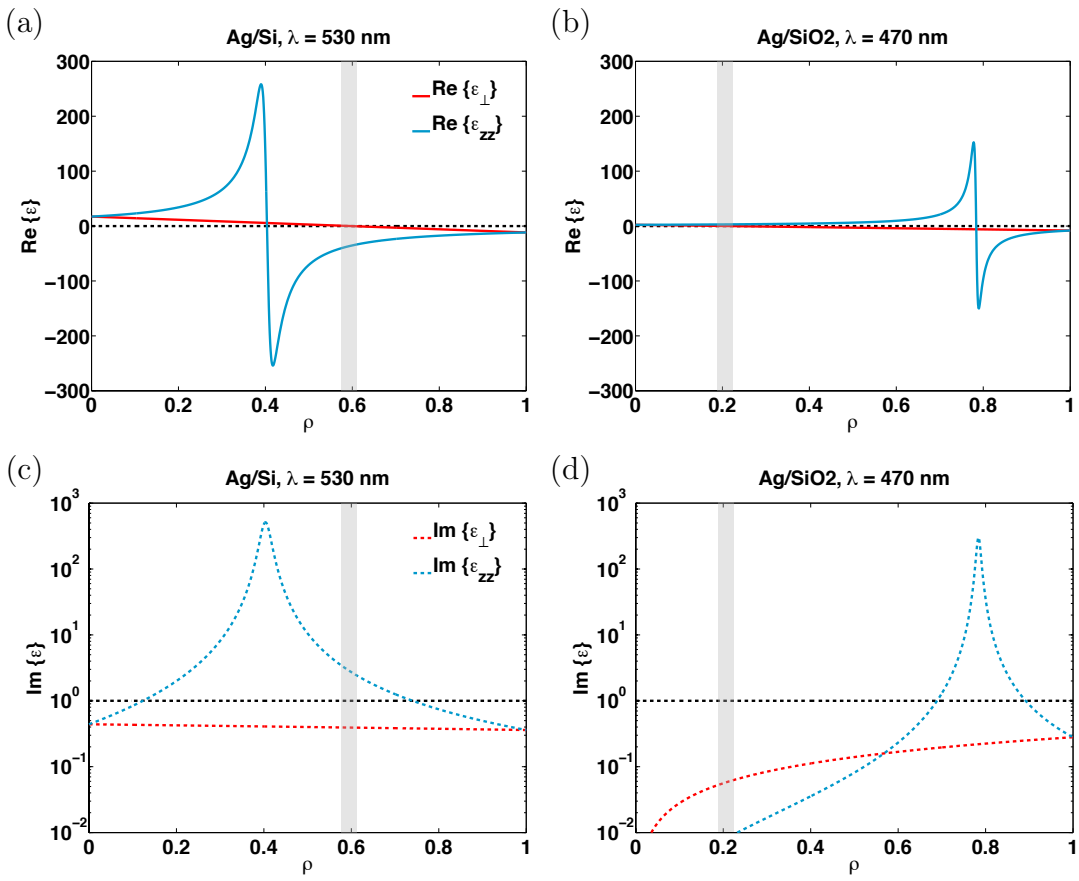

Figure A.3: Real (a,b) and imaginary (c,d, logarithmic scale) parts of the effective permittivity components as a function of the filling ratio ρ in (a,c) Ag/Si ML at $\lambda = 530$ nm, and in (b,d) Ag/SiO_2 ML at $\lambda = 470$ nm. The grey vertical stripe denotes the Re{$\varepsilon_\perp$}-near-zero region.

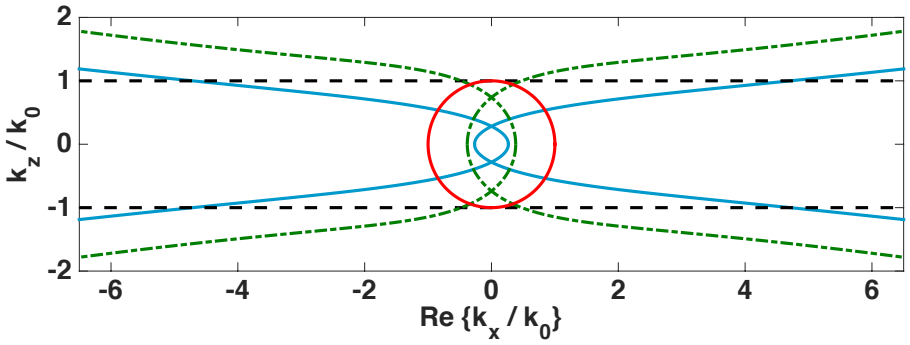

Figure A.4: Dispersion of the Ag/Si effective medium at $\lambda_1 = 530$ nm for different filling ratios ρ. Dash-dotted green curve: $\rho_A = 0.54$; solid blue curve: $\rho_B = 0.58$; red curve: dispersion of air.

bandwidth becomes significant.

Appendix A, in part, has been submitted for publication. L. Ferrari, J. S. T. Smalley, Y. Fainman and Z. Liu, "Hyperbolic metamaterials for dispersion-assisted directional light emission". The dissertation author is the first author of this paper.

Appendix B

Modulation bandwidth estimation

The relation of measured PL lifetime to modulation bandwidth is generally a complicated function that depends on the optical, electrical, and thermal properties of the LED, which ultimately depend on device geometry and packaging. However, the maximum modulation bandwidth may be easily found through a rate equation model derived for cavity-based LEDs [269]. The frequency response H is given by

$$H(\omega) = \frac{\Gamma}{\tau_p} = \frac{1}{\left(1+\frac{i\omega}{\gamma_p}\right)\left(1+\frac{i\omega}{\gamma_{eff}}\right)}, \tag{B.1}$$

where ω is the angular frequency ($\omega = 2\pi f$), Γ is the modal confinement factor and τ_p is the photon lifetime. The photon and spontaneous emission decay rates are $\gamma_p = \tau_p^{-1}$ and $\gamma_{eff} = \tau_{eff}^{-1}$, respectively, where τ_{eff} was defined by Eq. (6.5). In the absence of a cavity, the quality factor $Q = \omega/\gamma_p$, is determined by the natural linewidth of emission, which corresponds to the full-width at half-maximum (FWHM) of the PL spectra of Fig. 6.2(a). From Fig. 6.2(a), $\tau_p \approx [c/(430\text{ nm}) - c/(455\text{ nm})] = 3.9 \times 10^{-15}$ s, which is much smaller than τ_{eff}, of the order of tens of ps. Hence the frequency response is limited by γ_{eff}. Then, in this limit, we can write the maximum 3dB modulation bandwidth f'_{3dB} as

$$f'_{3dB} = max[f_{3dB}] = \frac{1}{2\pi\tau_{eff}}. \tag{B.2}$$

Fig. B.1 compares the frequency response of the control LED and of the PLED of Chapter 6, calculated according to Eq. (B.1). The experimentally measured lifetimes imply that the PLED can achieve a 3dB bandwidth exceeding 1 GHz. We note that the modal confinement factors of the control LED and the PLED are essentially identical, so that the Γ term has no effect on the comparison. Clearly, the PLED exhibits potential for high-speed operation in VLC. The excellent outcoupling efficiency, combined with the sub-100 ps PL lifetime, suggests that the PLED can indeed serve as both an efficient and a fast LED for VLC applications.

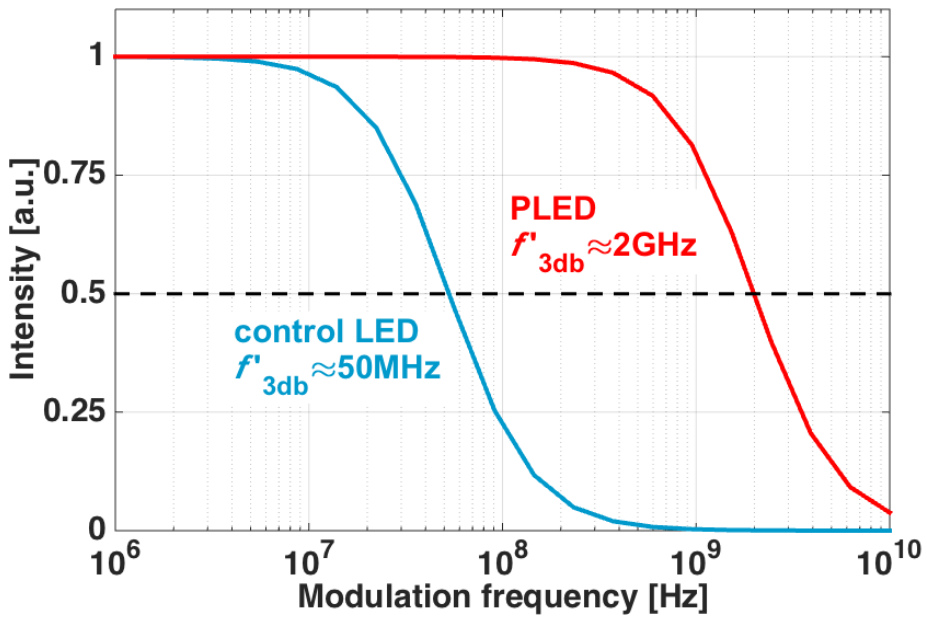

Figure B.1: Upper bounds of the 3dB bandwidth for the control LED and the PLED based on lifetime measurements. While the maximum 3dB bandwidth is limited to less than 100 MHz for the control LED, it exceeds 1 GHz for the PLED.

Appendix B, in part, is being prepared for submission for publication. L. Ferrari, J. S. T. Smalley, H. Qian, A. Tanaka, D. Lu, S. Dayeh, Y. Fainman and Z. Liu, “Design and analysis of blue InGaN/GaN plasmonic LED for high-speed, high-efficiency optical communications”. The dissertation author is the co-first author of this paper.

Bibliography

[1] Y. Liu and X. Zhang. Metamaterials: a new frontier of science and technology. *Chem. Soc. Rev.*, 40:2494–2507, 2011.

[2] V. G. Veselago. The electrodynamics of substances with simultaneously negative values of ε and μ. *Physics-Uspekhi*, 10(4):509–514, 1968.

[3] V. M. Shalaev. Optical negative-index metamaterials. *Nat. Photon.*, 1(1):41–48, 2007.

[4] H. Raether. *Surface plasmons on smooth and rough surfaces and on gratings*. Number 111 in Springer tracts in modern physics. Springer, 1988.

[5] S. A. Maier. *Plasmonics: Fundamentals and Applications: Fundamentals and Applications*. Springer, 2007.

[6] W. L. Barnes, A. Dereux, and T. W. Ebbesen. Surface plasmon subwavelength optics. *Nature*, 424(6950):824–830, 2003.

[7] S. A. Maier and H. A. Atwater. Plasmonics: Localization and guiding of electromagnetic energy in metal/dielectric structures. *Journal of Applied Physics*, 98(1):011101, 2005.

[8] J. M. Pitarke, V. M. Silkin, E. V. Chulkov, and P. M. Echenique. Theory of surface plasmons and surface-plasmon polaritons. *Reports on Progress in Physics*, 70(1):1, 2007.

[9] Z. Liu, H. Lee, Y. Xiong, C. Sun, and X. Zhang. Far-field optical hyperlens magnifying sub-diffraction-limited objects. *Science*, 315(5819):1686, 2007.

[10] J. Sun, M. I. Shalaev, and N. M. Litchinitser. Experimental demonstration of a non-resonant hyperlens in the visible spectral range. *Nat. Commun.*, 6:7201, 2015.

[11] Y. Xiong, Z. Liu, and X. Zhang. A simple design of flat hyperlens for lithography and imaging with half-pitch resolution down to 20 nm. *Applied Physics Letters*, 94(20):203108, 2009.

[12] J. Sun, T. Xu, and N. M. Litchinitser. Experimental demonstration of demagnifying hyperlens. *Nano Letters*, 16(12):7905–7909, 2016.

[13] D. Ji, H. Song, X. Zeng, H. Hu, K. Liu, N. Zhang, and Q. Gan. Broadband absorption engineering of hyperbolic metafilm patterns. *Scientific Reports*, 4:4498, 2014.

[14] C. T. Riley, J. S. T. Smalley, J. R. J. Brodie, Y. Fainman, D. J. Sirbuly, and Z. Liu. Near-perfect broadband absorption from hyperbolic metamaterial nanoparticles. *Proceedings of the National Academy of Sciences*, 114(6):1264–1268, 2017.

[15] J. Shi, B. Liu, P. Li, L. Y. Ng, and S. Shen. Near-field energy extraction with hyperbolic metamaterials. *Nano Letters*, 15(2):1217–1221, 2015.

[16] A. D. Neira, G. A. Wurtz, P. Ginzburg, and A. V. Zayats. Ultrafast all-optical modulation with hyperbolic metamaterial integrated in si photonic circuitry. *Opt. Express*, 22(9):10987–10994, 2014.

[17] Y. Sun, Z. Zheng, J. Cheng, G. Sun, and G. Qiao. Highly efficient second harmonic generation in hyperbolic metamaterial slot waveguides with large phase matching tolerance. *Opt. Express*, 23(5):6370–6378, 2015.

[18] D. Lu, J. J. Kan, E. E. Fullerton, and Z. Liu. Enhancing spontaneous emission rates of molecules using nanopatterned multilayer hyperbolic metamaterials. *Nat. Nano.*, 9(1):48–53, 2014.

[19] L. Ferrari, D. Lu, D. Lepage, and Z. Liu. Enhanced spontaneous emission inside hyperbolic metamaterials. *Opt. Express*, 22(4):4301–4306, 2014.

[20] K. L. Tsakmakidis, R. W. Boyd, E. Yablonovitch, and X. Zhang. Large spontaneous-emission enhancements in metallic nanostructures: towards LEDs faster than lasers. *Opt. Express*, 24(16):17916–17927, 2016.

[21] K. J. Russell, T.-L. Liu, S. Cui, and E. L. Hu. Large spontaneous emission enhancement in plasmonic nanocavities. *Nat. Photon.*, 6(7):459–462, 2012.

[22] G. M. Akselrod, C. Argyropoulos, T. B. Hoang, C. Ciracì, C. Fang, J. Huang, D. R. Smith, and M. H. Mikkelsen. Probing the mechanisms of large Purcell enhancement in plasmonic nanoantennas. *Nat. Photon.*, 8(11):835–840, 2014.

[23] M. S. Eggleston, K. Messer, L. Zhang, E. Yablonovitch, and M. C. Wu. Optical antenna enhanced spontaneous emission. *Proceedings of the National Academy of Sciences*, 112(6):1704–1709, 2015.

[24] L. Novotny and B. Hecht. *Principles of Nano-Optics*. Cambridge University Press, 2nd edition, 2012.

[25] G. P. Agrawal. *Fiber-Optic Communication Systems*. Wiley, 4th edition, 2010.

[26] L. Ferrari, C. Wu, D. Lepage, X. Zhang, and Z. Liu. Hyperbolic metamaterials and their applications. *Progress in Quantum Electronics*, 40:1–40, 2015.

[27] H. Chun, S. Rajbhandari, G. Faulkner, D. Tsonev, E. Xie, J. J. D. McKendry, E. Gu, M. D. Dawson, D. C. O'Brien, and H. Haas. LED based wavelength division multiplexed 10 Gb/s visible light communications. *Journal of Lightwave Technology*, 34(13):3047–3052, 2016.

[28] J. A. Simpson, B. L. Hughes, and J. F. Muth. Smart transmitters and receivers for underwater free-space optical communication. *IEEE Journal on Selected Areas in Communications*, 30(5):964–974, 2012.

[29] J. Vinogradov, R. Kruglov, K. L. Chi, J. W. Shi, M. Bloos, S. Loquai, and O. Ziemann. GaN light-emitting diodes for up to 5.5-Gb/s short-reach data transmission over SI-POF. *IEEE Photonics Technology Letters*, 26(24):2473–2475, 2014.

[30] D. R. Smith and D. Schurig. Electromagnetic wave propagation in media with indefinite permittivity and permeability tensors. *Phys. Rev. Lett.*, 90:077405, 2003.

[31] S. Ishii, A. V. Kildishev, E. Narimanov, V. M. Shalaev, and V. P. Drachev. Sub-wavelength interference pattern from volume plasmon polaritons in a hyperbolic medium. *Laser & Photonics Reviews*, 7(2):265–271, 2013.

[32] C. L. Cortes, W. Newman, S. Molesky, and Z. Jacob. Quantum nanophotonics using hyperbolic metamaterials. *Journal of Optics*, 14(6):063001, 2012.

[33] B. Wood, J. B. Pendry, and D. P. Tsai. Directed subwavelength imaging using a layered metal-dielectric system. *Phys. Rev. B*, 74:115116, 2006.

[34] B. E. A. Saleh and M. C. Teich. *Fundamentals of Photonics*. Wiley Series in Pure and Applied Optics. Wiley, 2007.

[35] Y. Liu, G. Bartal, and X. Zhang. All-angle negative refraction and imaging in a bulk medium made of metallic nanowires in the visible region. *Opt. Express*, 16(20):15439–15448, 2008.

[36] J. Yao, Z. Liu, Y. Liu, Y. Wang, C. Sun, G. Bartal, A. M. Stacy, and X. Zhang. Optical negative refraction in bulk metamaterials of nanowires. *Science*, 321(5891):930, 2008.

[37] C. Kittel. *Introduction to Solid State Physics*. John Wiley & Sons, Inc., New York, 6th edition, 1986.

[38] P. R. West, S. Ishii, G. V. Naik, N. K. Emani, V. M. Shalaev, and A. Boltasseva. Searching for better plasmonic materials. *Laser & Photonics Reviews*, 4(6):795–808, 2010.

[39] L. V. Alekseyev, V. A. Podolskiy, and E. E. Narimanov. Homogeneous hyperbolic systems for terahertz and far-infrared frequencies. *Advances in OptoElectronics*, 2012, 2012.

[40] J. Sun, J. Zhou, B. Li, and F. Kang. Indefinite permittivity and negative refraction in natural material: Graphite. *Applied Physics Letters*, 98(10):101901, 2011.

[41] R. K. Fisher and R. W. Gould. Resonance cones in the field pattern of a short antenna in an anisotropic plasma. *Phys. Rev. Lett.*, 22:1093–1095, 1969.

[42] S. M. Rytov. Electromagnetic properties of a finely stratified medium. *Soviet Physics JETP*, 2(10):466–475, 1956.

[43] H. N. S. Krishnamoorthy, Z. Jacob, E. Narimanov, I. Kretzschmar, and V. M. Menon. Topological transitions in metamaterials. *Science*, 336(6078):205–209, 2012.

[44] N. Engheta. Pursuing near-zero response. *Science*, 340(6130):286–287, 2013.

[45] A. J. Hoffman, L. Alekseyev, S. S. Howard, K. J. Franz, D. Wasserman, V. A. Podolskiy, E. E. Narimanov, D. L. Sivco, and C. Gmachl. Negative refraction in semiconductor metamaterials. *Nat. Mater.*, 6(12):946–950, 2007.

[46] A. Boltasseva and H. A. Atwater. Low-loss plasmonic metamaterials. *Science*, 331(6015):290–291, 2011.

[47] I. V. Iorsh, I. S. Mukhin, I. V. Shadrivov, P. A. Belov, and Y. S. Kivshar. Hyperbolic metamaterials based on multilayer graphene structures. *Phys. Rev. B*, 88:039904, 2013.

[48] A. M. DaSilva, Y.-C. Chang, T. Norris, and A. H. MacDonald. Enhancement of photonic density of states in finite graphene multilayers. *Phys. Rev. B*, 88:195411, 2013.

[49] M. A. K. Othman, C. Guclu, and F. Capolino. Graphene-based tunable hyperbolic metamaterials and enhanced near-field absorption. *Opt. Express*, 21(6):7614–7632, 2013.

[50] A. Andryieuski, A. V. Lavrinenko, and D. N. Chigrin. Graphene hyperlens for terahertz radiation. *Phys. Rev. B*, 86:121108, 2012.

[51] T. Zhang, L. Chen, and X. Li. Graphene-based tunable broadband hyperlens for far-field subdiffraction imaging at mid-infrared frequencies. *Opt. Express*, 21(18):20888–20899, 2013.

[52] D. Korobkin, B. Neuner III, C. Fietz, N. Jegenyes, G. Ferro, and G. Shvets. Measurements of the negative refractive index of sub-diffraction waves propagating in an indefinite permittivity medium. *Opt. Express*, 18(22):22734–22746, 2010.

[53] Y. Guo, C. L. Cortes, S. Molesky, and Z. Jacob. Broadband super-Planckian thermal emission from hyperbolic metamaterials. *Applied Physics Letters*, 101(13):131106, 2012.

[54] Y. Guo and Z. Jacob. Thermal hyperbolic metamaterials. *Opt. Express*, 21(12):15014–15019, 2013.

[55] Z. Jacob, J.-Y. Kim, G. V. Naik, A. Boltasseva, E. E. Narimanov, and V. M. Shalaev. Engineering photonic density of states using metamaterials. *Applied Physics B*, 100(1):215–218, 2010.

[56] J. Kim, V. P. Drachev, Z. Jacob, G. V. Naik, A. Boltasseva, E. E. Narimanov, and V. M. Shalaev. Improving the radiative decay rate for dye molecules with hyperbolic metamaterials. *Opt. Express*, 20(7):8100–8116, 2012.

[57] M. Y. Shalaginov, S. Ishii, J. Liu, J. Liu, J. Irudayaraj, A. Lagutchev, A. V. Kildishev, and V. M. Shalaev. Broadband enhancement of spontaneous emission from nitrogen-vacancy centers in nanodiamonds by hyperbolic metamaterials. *Applied Physics Letters*, 102(17):173114, 2013.

[58] X. Ni, G. V. Naik, A. V. Kildishev, Y. Barnakov, A. Boltasseva, and V. M. Shalaev. Effect of metallic and hyperbolic metamaterial surfaces on electric and magnetic dipole emission transitions. *Applied Physics B*, 103(3):553–558, 2011.

[59] K. V. Sreekanth, T. Biaglow, and G. Strangi. Directional spontaneous emission enhancement in hyperbolic metamaterials. *Journal of Applied Physics*, 114(13):134306, 2013.

[60] K. V. Sreekanth, A. De Luca, and G. Strangi. Experimental demonstration of surface and bulk plasmon polaritons in hypergratings. *Sci. Rep.*, 3, 2013.

[61] T. Tumkur, G. Zhu, P. Black, Yu. A. Barnakov, C. E. Bonner, and M. A. Noginov. Control of spontaneous emission in a volume of functionalized hyperbolic metamaterial. *Applied Physics Letters*, 99(15):151115, 2011.

[62] T. U. Tumkur, L. Gu, J. K. Kitur, E. E. Narimanov, and M. A. Noginov. Control of absorption with hyperbolic metamaterials. *Applied Physics Letters*, 100(16):161103, 2012.

[63] J. Rho, Z. Ye, Y. Xiong, X. Yin, Z. Liu, H. Choi, G. Bartal, and X. Zhang. Spherical hyperlens for two-dimensional sub-diffractional imaging at visible frequencies. *Nat. Commun.*, 1:143, 2010.

[64] G. V. Naik, J. Liu, A. V. Kildishev, V. M. Shalaev, and A. Boltasseva. Demonstration of Al:ZnO as a plasmonic component for near-infrared metamaterials. *Proceedings of the National Academy of Sciences*, 109(23):8834–8838, 2012.

[65] X. Yang, J. Yao, J. Rho, X. Yin, and X. Zhang. Experimental realization of three-dimensional indefinite cavities at the nanoscale with anomalous scaling laws. *Nat. Photon.*, 6(7):450–454, 2012.

[66] L. Shen, T.-J. Yang, and Y.-F. Chau. Effect of internal period on the optical dispersion of indefinite-medium materials. *Phys. Rev. B*, 77:205124, 2008.

[67] A. A. Orlov, P. M. Voroshilov, P. A. Belov, and Y. S. Kivshar. Engineered optical nonlocality in nanostructured metamaterials. *Phys. Rev. B*, 84:045424, 2011.

[68] A. V. Chebykin, A. A. Orlov, A. V. Vozianova, S. I. Maslovski, Y. S. Kivshar, and P. A. Belov. Nonlocal effective medium model for multilayered metal-dielectric metamaterials. *Phys. Rev. B*, 84:115438, 2011.

[69] A. V. Chebykin, A. A. Orlov, C. R. Simovski, Yu. S. Kivshar, and P. A. Belov. Nonlocal effective parameters of multilayered metal-dielectric metamaterials. *Phys. Rev. B*, 86:115420, 2012.

[70] W. Yan, M. Wubs, and N. A. Mortensen. Hyperbolic metamaterials: Nonlocal response regularizes broadband supersingularity. *Phys. Rev. B*, 86:205429, 2012.

[71] S. Raza, T. Christensen, M. Wubs, S. I. Bozhevolnyi, and N. A. Mortensen. Nonlocal response in thin-film waveguides: loss versus nonlocality and breaking of complementarity. *Phys. Rev. B*, 88:115401, 2013.

[72] W. Yan, N. A. Mortensen, and M. Wubs. Hyperbolic metamaterial lens with hydrodynamic nonlocal response. *Opt. Express*, 21(12):15026–15036, 2013.

[73] E. Amooghorban, N. A. Mortensen, and M. Wubs. Quantum optical effective-medium theory for loss-compensated metamaterials. *Phys. Rev. Lett.*, 110:153602, 2013.

[74] P. A. Belov, R. Marqués, S. I. Maslovski, I. S. Nefedov, M. Silveirinha, C. R. Simovski, and S. A. Tretyakov. Strong spatial dispersion in wire media in the very large wavelength limit. *Phys. Rev. B*, 67:113103, 2003.

[75] M. G. Silveirinha. Nonlocal homogenization model for a periodic array of ε-negative rods. *Phys. Rev. E*, 73:046612, 2006.

[76] B. M. Wells, A. V. Zayats, and V. A. Podolskiy. Nonlocal response of plasmonic nanorod metamaterials. In *Conference on Lasers and Electro-Optics 2012*, page JTh2A.81. Optical Society of America, 2012.

[77] A. J. Kerman, E. A. Dauler, W. E. Keicher, J. K. W. Yang, K. K. Berggren, G. Gol'tsman, and B. Voronov. Kinetic-inductance-limited reset time of superconducting nanowire photon counters. *Applied Physics Letters*, 88(11):111116, 2006.

[78] C. R. Simovski, P. A. Belov, A. V. Atrashchenko, and Y. S. Kivshar. Wire metamaterials: physics and applications. *Advanced Materials*, 24(31):4229–4248, 2012.

[79] J. Yao, Y. Wang, K.-T. Tsai, Z. Liu, X. Yin, G. Bartal, A. M. Stacy, Y.-L. Wang, and X. Zhang. Design, fabrication and characterization of indefinite metamaterials of nanowires. *Philosophical Transactions of the Royal Society A*, 369(1950):3434–3446, 2011.

[80] V. A. Podolskiy and E. E. Narimanov. Strongly anisotropic waveguide as a nonmagnetic left-handed system. *Phys. Rev. B*, 71:201101, 2005.

[81] J. Elser, R. Wangberg, V. A. Podolskiy, and E. E. Narimanov. Nanowire metamaterials with extreme optical anisotropy. *Applied Physics Letters*, 89(26):261102, 2006.

[82] A. Eftekhari. *Nanostructured Materials in Electrochemistry*. Wiley-VCH Verlag GmbH & Co. KGaA, 2008.

[83] P. Evans, W. R. Hendren, R. Atkinson, G. A. Wurtz, W. Dickson, A. V. Zayats, and R. J. Pollard. Growth and properties of gold and nickel nanorods in thin film alumina. *Nanotechnology*, 17(23):5746, 2006.

[84] M. A. Noginov, Yu. A. Barnakov, G. Zhu, T. Tumkur, H. Li, and E. E. Narimanov. Bulk photonic metamaterial with hyperbolic dispersion. *Applied Physics Letters*, 94(15):151105, 2009.

[85] I. S. Nefedov. Electromagnetic waves propagating in a periodic array of parallel metallic carbon nanotubes. *Phys. Rev. B*, 82:155423, 2010.

[86] J. Yao, K.-T. Tsai, Y. Wang, Z. Liu, G. Bartal, Y.-L. Wang, and X. Zhang. Imaging visible light using anisotropic metamaterial slab lens. *Opt. Express*, 17(25):22380–22385, 2009.

[87] M. A. Noginov, H. Li, Yu. A. Barnakov, D. Dryden, G. Nataraj, G. Zhu, C. E. Bonner, M. Mayy, Z. Jacob, and E. E. Narimanov. Controlling spontaneous emission with metamaterials. *Opt. Lett.*, 35(11):1863–1865, 2010.

[88] A. V. Kabashin, P. Evans, S. Pastkovsky, W. Hendren, G. A. Wurtz, R. Atkinson, R. Pollard, V. A. Podolskiy, and A. V. Zayats. Plasmonic nanorod metamaterials for biosensing. *Nat. Mater.*, 8(11):867–871, 2009.

[89] I. I. Smolyaninov. Optical microscopy beyond the diffraction limit. *HFSP Journal*, 2(3):129–131, 2008.

[90] E. Betzig and J. K. Trautman. Near-field optics: Microscopy, spectroscopy, and surface modification beyond the diffraction limit. *Science*, 257(5067):189–195, 1992.

[91] S. W. Hell. Far-field optical nanoscopy. *Science*, 316(5828):1153–1158, 2007.

[92] B. Huang, W. Wang, M. Bates, and X. Zhuang. Three-dimensional super-resolution imaging by stochastic optical reconstruction microscopy. *Science*, 319(5864):810–813, 2008.

[93] N. Fang, H. Lee, C. Sun, and X. Zhang. Sub-diffraction-limited optical imaging with a silver superlens. *Science*, 308(5721):534–537, 2005.

[94] Z. Liu, S. Durant, H. Lee, Y. Pikus, N. Fang, Y. Xiong, C. Sun, and X. Zhang. Far-field optical superlens. *Nano Letters*, 7(2):403–408, 2007.

[95] X. Zhang and Z. Liu. Superlenses to overcome the diffraction limit. *Nat. Mater.*, 7(6):435–441, 2008.

[96] S. A. Ramakrishna, J. B. Pendry, M. C. K. Wiltshire, and W. J. Stewart. Imaging the near field. *Journal of Modern Optics*, 50(9):1419–1430, 2003.

[97] D. R. Smith, P. Kolinko, and D. Schurig. Negative refraction in indefinite media. *J. Opt. Soc. Am. B*, 21(5):1032–1043, 2004.

[98] P. A. Belov. Backward waves and negative refraction in uniaxial dielectrics with negative dielectric permittivity along the anisotropy axis. *Microwave and Optical Technology Letters*, 37(4):259–263, 2003.

[99] T. G. Mackay, A. Lakhtakia, and R. A. Depine. Uniaxial dielectric media with hyperbolic dispersion relations. *Microwave and Optical Technology Letters*, 48(2):363–367, 2006.

[100] A. Fang, T. Koschny, and C. M. Soukoulis. Optical anisotropic metamaterials: negative refraction and focusing. *Phys. Rev. B*, 79:245127, 2009.

[101] D. R. Smith, D. Schurig, J. J. Mock, P. Kolinko, and P. Rye. Partial focusing of radiation by a slab of indefinite media. *Applied Physics Letters*, 84(13):2244–2246, 2004.

[102] H. Liu, Q. Lv, H. Luo, S. Wen, W. Shu, and D. Fan. Focusing of vectorial fields by a slab of indefinite media. *Journal of Optics A: Pure and Applied Optics*, 11(10):105103, 2009.

[103] G. Li, J. Li, and K. W. Cheah. Subwavelength focusing using a hyperbolic medium with a single slit. *Appl. Opt.*, 50(31):G27–G30, 2011.

[104] Z. Jacob, L. V. Alekseyev, and E. Narimanov. Optical hyperlens: Far-field imaging beyond the diffraction limit. *Opt. Express*, 14(18):8247–8256, 2006.

[105] D. Lu and Z. Liu. Hyperlenses and metalenses for far-field super-resolution imaging. *Nat. Commun.*, 3:1205, 2012.

[106] H. Lee, Z. Liu, Y. Xiong, C. Sun, and X. Zhang. Development of optical hyperlens for imaging below the diffraction limit. *Opt. Express*, 15(24):15886–15891, 2007.

[107] E. J. Smith, Z. Liu, Y. F. Mei, and O. G. Schmidt. System investigation of a rolled-up metamaterial optical hyperlens structure. *Applied Physics Letters*, 95(8):083104, 2009.

[108] J. B. Pendry and S. A. Ramakrishna. Near-field lenses in two dimensions. *Journal of Physics: Condensed Matter*, 14(36):8463, 2002.

[109] A. Salandrino and N. Engheta. Far-field subdiffraction optical microscopy using metamaterial crystals: Theory and simulations. *Phys. Rev. B*, 74:075103, 2006.

[110] S. Han, Y. Xiong, D. Genov, Z. Liu, G. Bartal, and X. Zhang. Ray optics at a deep-subwavelength scale: a transformation optics approach. *Nano Letters*, 8(12):4243–4247, 2008.

[111] A. V. Kildishev and V. M. Shalaev. Engineering space for light via transformation optics. *Opt. Lett.*, 33(1):43–45, 2008.

[112] V. M. Shalaev. Transforming light. *Science*, 322(5900):384–386, 2008.

[113] W. Wang, H. Xing, L. Fang, Y. Liu, J. Ma, L. Lin, C. Wang, and X. Luo. Far-field imaging device: planar hyperlens with magnification using multi-layer metamaterial. *Opt. Express*, 16(25):21142–21148, 2008.

[114] B. H. Cheng, Y. Z. Ho, Y.-C. Lan, and D. P. Tsai. Optical hybrid-superlens hyperlens for superresolution imaging. *IEEE Journal of Selected Topics in Quantum Electronics*, 19(3):4601305–4601305, 2013.

[115] A. V. Kildishev and E. E. Narimanov. Impedance-matched hyperlens. *Opt. Lett.*, 32(23):3432–3434, 2007.

[116] C. Ma and Z. Liu. Focusing light into deep subwavelength using metamaterial immersion lenses. *Opt. Express*, 18(5):4838–4844, 2010.

[117] C. Ma and Z. Liu. Metamaterial immersion lenses. In *Imaging and Applied Optics Congress*, page MWB5. Optical Society of America, 2010.

[118] C. Ma and Z. Liu. Breaking the imaging symmetry in negative refraction lenses. *Opt. Express*, 20(3):2581–2586, 2012.

[119] A. V. Kildishev, U. K. Chettiar, Z. Jacob, V. M. Shalaev, and E. E. Narimanov. Materializing a binary hyperlens design. *Applied Physics Letters*, 94(7):071102, 2009.

[120] N. Gibbons, J. J. Baumberg, C. L. Bower, M. Kolle, and U. Steiner. Scalable cylindrical metallodielectric metamaterials. *Advanced Materials*, 21(38-39):3933–3936, 2009.

[121] J. Kerbst, S. Schwaiger, A. Rottler, A. Koitmäe, M. Bröll, J. Ehlermann, A. Stemmann, C. Heyn, D. Heitmann, and S. Mendach. Enhanced transmission in rolled-up hyperlenses utilizing Fabry-Pérot resonances. *Applied Physics Letters*, 99(19):191905, 2011.

[122] S. Schwaiger, M. Bröll, A. Krohn, A. Stemmann, C. Heyn, Y. Stark, D. Stickler, D. Heitmann, and S. Mendach. Rolled-up three-dimensional metamaterials with a tunable plasma frequency in the visible regime. *Phys. Rev. Lett.*, 102:163903, 2009.

[123] S. Schwaiger, A. Rottler, and S. Mendach. Rolled-up metamaterials. *Advances in OptoElectronics*, 2012:10, 2012.

[124] D. Aronovich and G. Bartal. Nonlinear hyperlens. *Opt. Lett.*, 38(4):413–415, 2013.

[125] J. Wang, Y. Xu, H. Chen, and B. Zhang. Ultraviolet dielectric hyperlens with layered graphene and boron nitride. *J. Mater. Chem.*, 22:15863–15868, 2012.

[126] L. Ju, B. Geng, J. Horng, C. Girit, M. Martin, Z. Hao, H. A. Bechtel, X. Liang, A. Zettl, Y. R. Shen, and F. Wang. Graphene plasmonics for tunable terahertz metamaterials. *Nat. Nano.*, 6(10):630–634, 2011.

[127] P. A. Belov, C. R. Simovski, and P. Ikonen. Canalization of subwavelength images by electromagnetic crystals. *Phys. Rev. B*, 71:193105, 2005.

[128] G. Shvets, S. Trendafilov, J. B. Pendry, and A. Sarychev. Guiding, focusing, and sensing on the subwavelength scale using metallic wire arrays. *Phys. Rev. Lett.*, 99:053903, 2007.

[129] A. Ono, J. Kato, and S. Kawata. Subwavelength optical imaging through a metallic nanorod array. *Phys. Rev. Lett.*, 95:267407, 2005.

[130] P. Ikonen, C. Simovski, S. Tretyakov, P. Belov, and Y. Hao. Magnification of subwavelength field distributions at microwave frequencies using a wire medium slab operating in the canalization regime. *Applied Physics Letters*, 91(10):104102, 2007.

[131] Y. Zhao, G. Palikaras, P. A Belov, R. F. Dubrovka, C. R. Simovski, Y. Hao, and C. G. Parini. Magnification of subwavelength field distributions using a tapered array of metallic wires with planar interfaces and an embedded dielectric phase compensator. *New Journal of Physics*, 12(10):103045, 2010.

[132] B. D. F. Casse, W. T. Lu, Y. J. Huang, E. Gultepe, L. Menon, and S. Sridhar. Super-resolution imaging using a three-dimensional metamaterials nanolens. *Applied Physics Letters*, 96(2):023114, 2010.

[133] Y. Xiong, Z. Liu, and X. Zhang. Projecting deep-subwavelength patterns from diffraction-limited masks using metal-dielectric multilayers. *Applied Physics Letters*, 93(11):111116, 2008.

[134] K. Okamoto, I. Niki, A. Shvartser, Y. Narukawa, T. Mukai, and A. Scherer. Surface-plasmon-enhanced light emitters based on InGaN quantum wells. *Nat. Mater.*, 3(9):601–605, 2004.

[135] M. Francardi, L. Balet, A. Gerardino, N. Chauvin, D. Bitauld, L. H. Li, B. Alloing, and A. Fiore. Enhanced spontaneous emission in a photonic-crystal light-emitting diode. *Applied Physics Letters*, 93(14):143102, 2008.

[136] G. Shambat, B. Ellis, A. Majumdar, J. Petykiewicz, M. A. Mayer, T. Sarmiento, J. Harris, E. E. Haller, and J. Vučković. Ultrafast direct modulation of a single-mode photonic crystal nanocavity light-emitting diode. *Nat. Commun.*, 2:539, 2011.

[137] M. D. Eisaman, J. Fan, A. Migdall, and S. V. Polyakov. Single-photon sources and detectors. *Review of Scientific Instruments*, 82(7):071101, 2011.

[138] J. H. Prechtel, A. V. Kuhlmann, J. Houel, L. Greuter, A. Ludwig, D. Reuter, A. D. Wieck, and R. J. Warburton. Frequency-stabilized source of single photons from a solid-state qubit. *Phys. Rev. X*, 3:041006, 2013.

[139] H. G. Frey, S. Witt, K. Felderer, and R. Guckenberger. High-resolution imaging of single fluorescent molecules with the optical near-field of a metal tip. *Phys. Rev. Lett.*, 93:200801, 2004.

[140] J. P. Dowling. Spontaneous emission in cavities: How much more classical can you get? *Foundations of Physics*, 23(6):895–905, 1993.

[141] E. M. Purcell. Spontaneous emission probabilities at radio frequencies. *Phys. Rev.*, 69:681–681, 1946.

[142] K. J. Vahala. Optical microcavities. *Nature*, 424(6950):839–846, 2003.

[143] M. T. Hill, Y.-S. Oei, B. Smalbrugge, Y. Zhu, T. de Vries, P. J. van Veldhoven, F. W. M. van Otten, T. J. Eijkemans, J. P. Turkiewicz, H. de Waardt, E. J. Geluk, S.-H. Kwon, Y.-H. Lee, R. Notzel, and M. K. Smit. Lasing in metallic-coated nanocavities. *Nat. Photon.*, 1(10):589–594, 2007.

[144] G. W. Ford and W. H. Weber. Electromagnetic interactions of molecules with metal surfaces. *Physics Reports*, 113(4):195 – 287, 1984.

[145] W. L. Barnes. Fluorescence near interfaces: the role of photonic mode density. *Journal of Modern Optics*, 45(4):661–699, 1998.

[146] O. Kidwai, S. V. Zhukovsky, and J. E. Sipe. Effective-medium approach to planar multilayer hyperbolic metamaterials: strengths and limitations. *Phys. Rev. A*, 85:053842, 2012.

[147] S. V. Zhukovsky, O. Kidwai, and J. E. Sipe. Physical nature of volume plasmon polaritons in hyperbolic metamaterials. *Opt. Express*, 21(12):14982–14987, 2013.

[148] J. B. Khurgin and A. Boltasseva. Reflecting upon the losses in plasmonics and metamaterials. *MRS Bulletin*, 37:768–779, 2012.

[149] O. Kidwai, S. V. Zhukovsky, and J. E. Sipe. Dipole radiation near hyperbolic metamaterials: applicability of effective-medium approximation. *Opt. Lett.*, 36(13):2530–2532, 2011.

[150] A. N. Poddubny, P. A. Belov, P. Ginzburg, A. V. Zayats, and Y. S. Kivshar. Microscopic model of Purcell enhancement in hyperbolic metamaterials. *Phys. Rev. B*, 86:035148, 2012.

[151] A. N. Poddubny, P. A. Belov, and Y. S. Kivshar. Spontaneous radiation of a finite-size dipole emitter in hyperbolic media. *Phys. Rev. A*, 84:023807, 2011.

[152] A. S. Potemkin, A. N. Poddubny, P. A. Belov, and Y. S. Kivshar. Green function for hyperbolic media. *Phys. Rev. A*, 86:023848, 2012.

[153] C. Guclu, S. Campione, and F. Capolino. Hyperbolic metamaterial as super absorber for scattered fields generated at its surface. *Phys. Rev. B*, 86:205130, 2012.

[154] W. D. Newman, C. L. Cortes, and Z. Jacob. Enhanced and directional single-photon emission in hyperbolic metamaterials. *J. Opt. Soc. Am. B*, 30(4):766–775, 2013.

[155] T. Hümmer, F. J. García-Vidal, L. Martín-Moreno, and D. Zueco. Weak and strong coupling regimes in plasmonic QED. *Phys. Rev. B*, 87:115419, 2013.

[156] Z. Liu, W. Li, X. Jiang, and J. C. Cao. Spontaneous emission from a medium with elliptic and hyperbolic dispersion. *Phys. Rev. A*, 87:053836, 2013.

[157] Z. Jacob, I. I. Smolyaninov, and E. E. Narimanov. Broadband Purcell effect: radiative decay engineering with metamaterials. *Applied Physics Letters*, 100(18):181105, 2012.

[158] Z. Jacob and V. M. Shalaev. Plasmonics goes quantum. *Science*, 334(6055):463–464, 2011.

[159] S.-A. Biehs, M. Tschikin, and P. Ben-Abdallah. Hyperbolic metamaterials as an analog of a blackbody in the near field. *Phys. Rev. Lett.*, 109:104301, 2012.

[160] B. Liu and S. Shen. Broadband near-field radiative thermal emitter/absorber based on hyperbolic metamaterials: direct numerical simulation by the Wiener chaos expansion method. *Phys. Rev. B*, 87:115403, 2013.

[161] S.-A. Biehs, M. Tschikin, R. Messina, and P. Ben-Abdallah. Super-Planckian near-field thermal emission with phonon-polaritonic hyperbolic metamaterials. *Applied Physics Letters*, 102(13):131106, 2013.

[162] X. Ni, S. Ishii, M. D. Thoreson, V. M. Shalaev, S. Han, S. Lee, and A. V. Kildishev. Loss-compensated and active hyperbolic metamaterials. *Opt. Express*, 19(25):25242–25254, 2011.

[163] R. S. Savelev, I. V. Shadrivov, P. A. Belov, N. N. Rosanov, S. V. Fedorov, A. A. Sukhorukov, and Y. S. Kivshar. Loss compensation in metal-dielectric layered metamaterials. *Phys. Rev. B*, 87:115139, 2013.

[164] C. Argyropoulos, N. M. Estakhri, F. Monticone, and A. Alù. Negative refraction, gain and nonlinear effects in hyperbolic metamaterials. *Opt. Express*, 21(12):15037–15047, 2013.

[165] M. T. Hill, M. Marell, E. S. P. Leong, B. Smalbrugge, Y. Zhu, M. Sun, P. J. van Veldhoven, E. Jan Geluk, F. Karouta, Y.-S. Oei, R. Nötzel, C.-Z. Ning, and M. K. Smit. Lasing in metal-insulator-metal sub-wavelength plasmonic waveguides. *Opt. Express*, 17(13):11107–11112, 2009.

[166] J. Seidel, S. Grafström, and L. Eng. Stimulated emission of surface plasmons at the interface between a silver film and an optically pumped dye solution. *Phys. Rev. Lett.*, 94:177401, 2005.

[167] I. De Leon and P. Berini. Amplification of long-range surface plasmons by a dipolar gain medium. *Nat. Photon.*, 4(6):382–387, 2010.

[168] M. A. Noginov, V. A. Podolskiy, G. Zhu, M. Mayy, M. Bahoura, J. A. Adegoke, B. A. Ritzo, and K. Reynolds. Compensation of loss in propagating surface plasmon polariton by gain in adjacent dielectric medium. *Opt. Express*, 16(2):1385–1392, 2008.

[169] M. A. Noginov, G. Zhu, M. Mayy, B. A. Ritzo, N. Noginova, and V. A. Podolskiy. Stimulated emission of surface plasmon polaritons. *Phys. Rev. Lett.*, 101:226806, 2008.

[170] S. Xiao, V. P. Drachev, A. V. Kildishev, X. Ni, U. K. Chettiar, H.-K. Yuan, and V. M. Shalaev. Loss-free and active optical negative-index metamaterials. *Nature*, 466(7307):735–738, 2010.

[171] X. Meng, A. V. Kildishev, K. Fujita, K. Tanaka, and V. M. Shalaev. Wavelength-tunable spasing in the visible. *Nano Letters*, 13(9):4106–4112, 2013.

[172] M. A. Noginov, G. Zhu, A. M. Belgrave, R. Bakker, V. M. Shalaev, E. E. Narimanov, S. Stout, E. Herz, T. Suteewong, and U. Wiesner. Demonstration of a spaser-based nanolaser. *Nature*, 460(7259):1110–1112, 2009.

[173] M. Ambati, S. H. Nam, E. Ulin-Avila, D. A. Genov, G. Bartal, and X. Zhang. Observation of stimulated emission of surface plasmon polaritons. *Nano Letters*, 8(11):3998–4001, 2008.

[174] J. Grandidier, G. C. des Francs, S. Massenot, A. Bouhelier, L. Markey, J.-C. Weeber, C. Finot, and A. Dereux. Gain-assisted propagation in a plasmonic waveguide at telecom wavelength. *Nano Letters*, 9(8):2935–2939, 2009.

[175] R. F. Oulton, V. J. Sorger, T. Zentgraf, R.-M. Ma, C. Gladden, L. Dai, G. Bartal, and X. Zhang. Plasmon lasers at deep subwavelength scale. *Nature*, 461(7264):629–632, 2009.

[176] F. H. L. Koppens, D. E. Chang, and F. J. García de Abajo. Graphene plasmonics: a platform for strong light–matter interactions. *Nano Letters*, 11(8):3370–3377, 2011.

[177] V. W. Brar, M. S. Jang, M. Sherrott, J. J. Lopez, and H. A. Atwater. Highly confined tunable mid-infrared plasmonics in graphene nanoresonators. *Nano Letters*, 13(6):2541–2547, 2013.

[178] M. A. K. Othman, C. Guclu, and F. Capolino. Graphene–dielectric composite metamaterials: evolution from elliptic to hyperbolic wavevector dispersion and the transverse epsilon-near-zero condition. *Journal of Nanophotonics*, 7(1):073089–073089, 2013.

[179] E. D. Palik. *Handbook of Optical Constants of Solids*. Number 2 in Academic Press handbook series. Academic Press, 1991.

[180] S. H. Mousavi, I. Kholmanov, K. B. Alici, D. Purtseladze, N. Arju, K. Tatar, D. Y. Fozdar, J. W. Suk, Y. Hao, A. B. Khanikaev, R. S. Ruoff, and G. Shvets. Inductive tuning of Fano-resonant metasurfaces using plasmonic response of graphene in the mid-infrared. *Nano Letters*, 13(3):1111–1117, 2013.

[181] Y. Cui, K. H. Fung, J. Xu, H. Ma, Y. Jin, S. He, and N. X. Fang. Ultrabroadband light absorption by a sawtooth anisotropic metamaterial slab. *Nano Letters*, 12(3):1443–1447, 2012.

[182] J. Yao, X. Yang, X. Yin, G. Bartal, and X. Zhang. Three-dimensional nanometer-scale optical cavities of indefinite medium. *Proceedings of the National Academy of Sciences*, 108(28):11327–11331, 2011.

[183] H. Hu, D. Ji, X. Zeng, K. Liu, and Q. Gan. Rainbow trapping in hyperbolic metamaterial waveguide. *Sci. Rep.*, 3, 2013.

[184] K. L. Tsakmakidis, A. D. Boardman, and O. Hess. Trapped rainbow storage of light in metamaterials. *Nature*, 450(7168):397–401, 2007.

[185] J. Park, K.-Y. Kim, I.-M. Lee, H. Na, S.-Y. Lee, and B. Lee. Trapping light in plasmonic waveguides. *Opt. Express*, 18(2):598–623, 2010.

[186] M. S. Jang and H. Atwater. Plasmonic rainbow trapping structures for light localization and spectrum splitting. *Phys. Rev. Lett.*, 107:207401, 2011.

[187] I. S. Nefedov, C. A. Valagiannopoulos, S. M. Hashemi, and E. I. Nefedov. Total absorption in asymmetric hyperbolic media. *Sci. Rep.*, 3, 2013.

[188] E. E. Narimanov, H. Li, Yu. A. Barnakov, T. U. Tumkur, and M. A. Noginov. Reduced reflection from roughened hyperbolic metamaterial. *Opt. Express*, 21(12):14956–14961, 2013.

[189] Y. He, S. He, J. Gao, and X. Yang. Giant transverse optical forces in nanoscale slot waveguides of hyperbolic metamaterials. *Opt. Express*, 20(20):22372–22382, 2012.

[190] P. Ginzburg, A. V. Krasavin, A. N. Poddubny, P. A. Belov, Y. S. Kivshar, and A. V. Zayats. Self-induced torque in hyperbolic metamaterials. *Phys. Rev. Lett.*, 111:036804, 2013.

[191] T. A. Morgado, S. I. Maslovski, and M. G. Silveirinha. Ultrahigh Casimir interaction torque in nanowire systems. *Opt. Express*, 21(12):14943–14955, 2013.

[192] F. Capasso, J.N. Munday, D. Iannuzzi, and H. B. Chan. Casimir forces and quantum electrodynamical torques: physics and nanomechanics. *Selected Topics in Quantum Electronics, IEEE Journal of*, 13(2):400–414, 2007.

[193] J. N. Munday, D. Iannuzzi, Y. Barash, and F. Capasso. Torque on birefringent plates induced by quantum fluctuations. *Phys. Rev. A*, 71:042102, 2005.

[194] S. Savoia, G. Castaldi, and V. Galdi. Optical nonlocality in multilayered hyperbolic metamaterials based on Thue-Morse superlattices. *Phys. Rev. B*, 87:235116, 2013.

[195] J. M. McMahon, S. K. Gray, and G. C. Schatz. Nonlocal optical response of metal nanostructures with arbitrary shape. *Phys. Rev. Lett.*, 103:097403, 2009.

[196] A. I. Fernández-Domínguez, A. Wiener, F. J. García-Vidal, S. A. Maier, and J. B. Pendry. Transformation-optics description of nonlocal effects in plasmonic nanostructures. *Phys. Rev. Lett.*, 108:106802, 2012.

[197] A. Wiener, A. I. Fernández-Domínguez, A. P. Horsfield, J. B. Pendry, and S. A. Maier. Nonlocal effects in the nanofocusing performance of plasmonic tips. *Nano Letters*, 12(6):3308–3314, 2012.

[198] T. V. Teperik, P. Nordlander, J. Aizpurua, and A. G. Borisov. Quantum effects and nonlocality in strongly coupled plasmonic nanowire dimers. *Opt. Express*, 21(22):27306–27325, 2013.

[199] G. V. Naik, V. M. Shalaev, and A. Boltasseva. Alternative plasmonic materials: beyond gold and silver. *Advanced Materials*, 25(24):3264–3294, 2013.

[200] A. Kinkhabwala, Z. Yu, S. Fan, Y. Avlasevich, K. Mullen, and W. E. Moerner. Large single-molecule fluorescence enhancements produced by a bowtie nanoantenna. *Nat. Photon.*, 3(11):654–657, 2009.

[201] I. De Leon and P. Berini. Theory of noise in high-gain surface plasmon-polariton amplifiers incorporating dipolar gain media. *Opt. Express*, 19(21):20506–20517, 2011.

[202] A. G. Brolo. Plasmonics for future biosensors. *Nat. Photon.*, 6(11):709–713, 2012.

[203] M. J. Levene, J. Korlach, S. W. Turner, M. Foquet, H. G. Craighead, and W. W. Webb. Zero-mode waveguides for single-molecule analysis at high concentrations. *Science*, 299(5607):682–686, 2003.

[204] P. Yeh. *Optical Waves in Layered Media*. Wiley Series in Pure and Applied Optics. Wiley, 2005.

[205] P. B. Johnson and R. W. Christy. Optical constants of the noble metals. *Phys. Rev. B*, 6:4370–4379, 1972.

[206] D. E. Aspnes and A. A. Studna. Dielectric functions and optical parameters of Si, Ge, GaP, GaAs, GaSb, InP, InAs, and InSb from 1.5 to 6.0 eV. *Phys. Rev. B*, 27:985–1009, 1983.

[207] P. Berini. Long-range surface plasmon polaritons. *Adv. Opt. Photon.*, 1(3):484–588, 2009.

[208] K. V. Sreekanth, K. H. Krishna, A. De Luca, and G. Strangi. Large spontaneous emission rate enhancement in grating coupled hyperbolic metamaterials. *Scientific Reports*, 4:6340, 2014.

[209] T. Galfsky, H. N. S. Krishnamoorthy, W. Newman, E. E. Narimanov, Z. Jacob, and V. M. Menon. Active hyperbolic metamaterials: enhanced spontaneous emission and light extraction. *Optica*, 2(1):62–65, 2015.

[210] T.-H. Kao and Y.-C. Hung. Enhancement of light extraction based on nanowire hyperbolic metamaterials in a grating structure. *Proceedings SPIE*, 9883:98830U, 2016.

[211] X. Zhang, J.-J. Xiao, Q. Zhang, F. Qin, X. Cai, and F. Ye. Dual-band unidirectional emission in a multilayered metal-dielectric nanoantenna. *ACS Omega*, 2(3):774–783, 2017.

[212] R. Alaee, R. Filter, D. Lehr, F. Lederer, and C. Rockstuhl. A generalized Kerker condition for highly directive nanoantennas. *Opt. Lett.*, 40(11):2645–2648, 2015.

[213] X. M. Zhang, J. J. Xiao, Q. Zhang, L. M. Li, and Y. Yao. Plasmonic TM-like cavity modes and the hybridization in multilayer metal-dielectric nanoantenna. *Opt. Express*, 23(12):16122–16132, 2015.

[214] R. Guo, M. Decker, I. Staude, D. N. Neshev, and Y. S. Kivshar. Bidirectional waveguide coupling with plasmonic Fano nanoantennas. *Applied Physics Letters*, 105(5):053114, 2014.

[215] P. Segovia, G. Marino, A. V. Krasavin, N. Olivier, G. A. Wurtz, P. A. Belov, P. Ginzburg, and A. V. Zayats. Hyperbolic metamaterial antenna for second-harmonic generation tomography. *Opt. Express*, 23(24):30730–30738, 2015.

[216] L. Carletti, A. Locatelli, D. Neshev, and C. De Angelis. Shaping the radiation pattern of second-harmonic generation from AlGaAs dielectric nanoantennas. *ACS Photonics*, 3(8):1500–1507, 2016.

[217] C. Guclu, T. S. Luk, G. T. Wang, and F. Capolino. Radiative emission enhancement using nano-antennas made of hyperbolic metamaterial resonators. *Applied Physics Letters*, 105(12):123101, 2014.

[218] I. S. Maksymov. Magneto-plasmonic nanoantennas: basics and applications. *Reviews in Physics*, 1:36 – 51, 2016.

[219] P. R. West, N. Kinsey, M. Ferrera, A. V. Kildishev, V. M. Shalaev, and A. Boltasseva. Adiabatically tapered hyperbolic metamaterials for dispersion control of high-k waves. *Nano Letters*, 15(1):498–505, 2015.

[220] P. Shekhar, J. Atkinson, and Z. Jacob. Hyperbolic metamaterials: fundamentals and applications. *Nano Convergence*, 1(1):14, 2014.

[221] A. Orlov, I. Iorsh, P. Belov, and Y. Kivshar. Complex band structure of nanostructured metal-dielectric metamaterials. *Opt. Express*, 21(2):1593–1598, 2013.

[222] S. Campione, T. S. Luk, S. Liu, and M. B. Sinclair. Realizing high-quality, ultralarge momentum states and ultrafast topological transitions using semiconductor hyperbolic metamaterials. *J. Opt. Soc. Am. B*, 32(9):1809–1815, 2015.

[223] A. Yariv and P. Yeh. *Photonics: Optical Electronics in Modern Communications*. Oxford University Press, Oxford, 6th edition, 2006.

[224] J. S. T. Smalley, F. Vallini, S. A. Montoya, L. Ferrari, S. Shahin, C. T. Riley, B. Kanté, E. E. Fullerton, Z. Liu, and Y. Fainman. Luminescent hyperbolic metasurfaces. *Nat. Commun.*, 8:13793, 2017.

[225] I. Avrutsky, I. Salakhutdinov, J. Elser, and V. Podolskiy. Highly confined optical modes in nanoscale metal-dielectric multilayers. *Phys. Rev. B*, 75:241402, 2007.

[226] J. S. T. Smalley, F. Vallini, B. Kanté, and Y. Fainman. Modal amplification in active waveguides with hyperbolic dispersion at telecommunication frequencies. *Opt. Express*, 22(17):21088–21105, 2014.

[227] J. S. T. Smalley, F. Vallini, S. Shahin, B. Kanté, and Y. Fainman. Gain-enhanced high-k transmission through metal-semiconductor hyperbolic metamaterials. *Opt. Mater. Express*, 5(10):2300–2312, 2015.

[228] J. S. T. Smalley, F. Vallini, S. Montoya, E. E. Fullerton, and Y. Fainman. Practical realization of deeply subwavelength metal-dielectric nanostructures based on InGaAsP. *Proceedings SPIE*, 9544:95440S, 2015.

[229] J. S. Smalley, F. Vallini, S. Montoya, L. Ferrari, C. Riley, S. Shahin, B. Kante, E. E. Fullerton, Z. Liu, and Y. Fainman. Light-emitting hyperbolic metasurfaces at telecom frequencies. In *Advanced Photonics 2016 (IPR, NOMA, Sensors, Networks, SPPCom, SOF)*, page NoM3C.3. Optical Society of America, 2016.

[230] S. Zhao, H. P.T. Nguyen, Md. G. Kibria, and Z. Mi. III-Nitride nanowire optoelectronics. *Progress in Quantum Electronics*, 44:14–68, 2015.

[231] A. Boltasseva and H. A. Atwater. Low-loss plasmonic metamaterials. *Science*, 331(6015):290–291, 2011.

[232] C. T. Riley, J. S. T. Smalley, K. W. Post, D. N. Basov, Y. Fainman, D. Wang, Z. Liu, and D. J. Sirbuly. High-quality, ultraconformal aluminum-doped zinc oxide nanoplasmonic and hyperbolic metamaterials. *Small*, 12(7):892–901, 2016.

[233] A. K. Geim and I. V. Grigorieva. Van der Waals heterostructures. *Nature*, 499(7459):419–425, 2013.

[234] G. Clark, J. R. Schaibley, J. Ross, T. Taniguchi, K. Watanabe, J. R. Hendrickson, S. Mou, W. Yao, and X. Xu. Single defect light-emitting diode in a van der Waals heterostructure. *Nano Letters*, 16(6):3944–3948, 2016.

[235] C. Palacios-Berraquero, M. Barbone, D. M. Kara, X. Chen, I. Goykhman, D. Yoon, A. K. Ott, J. Beitner, K. Watanabe, T. Taniguchi, A. C. Ferrari, and M. Atatüre. Atomically thin quantum light-emitting diodes. *Nat. Commun.*, 7:12978, 2016.

[236] S. Dai, Q. Ma, M. K. Liu, T. Andersen, Z. Fei, M. D. Goldflam, M. Wagner, K. Watanabe, T. Taniguchi, M. Thiemens, F. Keilmann, G. C. A. M. Janssen, S.-E. Zhu, P. Jarillo-Herrero, M. M. Fogler, and D. N. Basov. Graphene on hexagonal boron nitride as a tunable hyperbolic metamaterial. *Nat. Nano.*, 10(8):682–686, 2015.

[237] Y.-C. Chang, C.-H. Liu, C.-H. Liu, S. Zhang, S. R. Marder, E. E. Narimanov, Z. Zhong, and T. B. Norris. Realization of mid-infrared graphene hyperbolic metamaterials. *Nat. Commun.*, 7:10568, 2016.

[238] G. T. Papadakis and H. A. Atwater. Field-effect induced tunability in hyperbolic metamaterials. *Phys. Rev. B*, 92:184101, 2015.

[239] S. Prayakarao, B. Mendoza, A. Devine, C. Kyaw, R. B. van Dover, V. Liberman, and M. A. Noginov. Tunable VO2/Au hyperbolic metamaterial. *Applied Physics Letters*, 109(6):061105, 2016.

[240] L. U. Khan. Visible light communication: applications, architecture, standardization and research challenges. *Digital Communications and Networks*, 3(2):78 – 88, 2017.

[241] P. H. Pathak, X. Feng, P. Hu, and P. Mohapatra. Visible light communication, networking, and sensing: a survey, potential and challenges. *IEEE Communications Surveys Tutorials*, 17(4):2047–2077, 2015.

[242] S. Pimputkar, J. S. Speck, S. P. DenBaars, and S. Nakamura. Prospects for LED lighting. *Nat. Photon.*, 3(4):180–182, 2009.

[243] C.-S. A. Gong, Y.-C. Lee, J.-L. Lai, C.-H. Yu, L. R. Huang, and C.-Y. Yang. The high-efficiency LED driver for visible light communication applications. *Scientific Reports*, 6:30991, 2016.

[244] T. Galfsky, Z. Sun, C. R. Considine, C.-T. Chou, W.-C. Ko, Y.-H. Lee, E. E. Narimanov, and V. M. Menon. Broadband enhancement of spontaneous emission in two-dimensional semiconductors using photonic hypercrystals. *Nano Letters*, 16(8):4940–4945, 2016.

[245] L. Liu, L. Zhao, S. Zhu, Z. Yu, P. An, C. Yang, C. Wu, and J. Li. Design of GaN-based surface plasmon LEDs to enhance the modulation bandwidth and light output. *Physica Status Solidi (c)*, 13(5-6):283–288, 2016.

[246] H. Murotani, Y. Yamada, Y. Honda, and H. Amano. Excitation density dependence of radiative and nonradiative recombination lifetimes in InGaN/GaN multiple quantum wells. *Physica Status Solidi (b)*, 252(5):940–945, 2015.

[247] S.-C. Zhu, Z.-G. Yu, L.-X. Zhao, J.X. Wang, and J.-M. Li. Enhancement of the modulation bandwidth for GaN-based light-emitting diode by surface plasmons. *Optics express*, 23(11):13752–13760, 2015.

[248] A.B. Djurišić, Y. Chan, and E.H. Li. Novel model for the optical function of GaN. *Applied Physics A*, 74(5):669–674, 2002.

[249] M.-K. Kwon, J.-Y. Kim, B.-H. Kim, I.-K. Park, C.-Y. Cho, C. C. Byeon, and S.-J. Park. Surface-plasmon-enhanced light-emitting diodes. *Advanced Materials*, 20(7):1253–1257, 2008.

[250] S. J. Pearton. *Design and Fabrication of Gallium High-Power Rectifiers*, pages 179–212. Springer London, London, 2006.

[251] D. Y. Lei, J. Li, A. I. Fernández-Domínguez, H. C. Ong, and S. A. Maier. Geometry dependence of surface plasmon polariton lifetimes in nanohole arrays. *ACS Nano*, 4(1):432–438, 2010.

[252] S. Bagheri, K. Weber, T. Gissibl, T. Weiss, F. Neubrech, and H. Giessen. Fabrication of square-centimeter plasmonic nanoantenna arrays by femtosecond direct laser writing lithography: effects of collective excitations on SEIRA enhancement. *ACS Photonics*, 2(6):779–786, 2015.

[253] V. K. Tikhomirov, K. Driesen, C. Görller-Walrand, and M. Mortier. Broadband telecommunication wavelength emission in Yb^{3+}-Er^{3+}-Tm^{3+} co-doped nano-glass-ceramics. *Opt. Express*, 15(15):9535–9540, 2007.

[254] Z. Gao, Y. Liu, J. Ren, Z. Fang, X. Lu, E. Lewis, G. Farrell, J. Yang, and P. Wang. Selective doping of Ni^{2+} in highly transparent glass-ceramics containing nano-spinels $ZnGa_2O_4$ and $Zn_{1+x}Ga_{2-2x}Ge_xO_4$ for broadband near-infrared fiber amplifiers. *Scientific Reports*, 7:1783, 2017.

[255] L. Zhang and E. Wang. Metal nanoclusters: new fluorescent probes for sensors and bioimaging. *Nano Today*, 9(1):132 – 157, 2014.

[256] T. Galfsky, J. Gu, E. E. Narimanov, and V. M. Menon. Photonic hypercrystals for control of light-matter interactions. *Proceedings of the National Academy of Sciences*, 114(20):5125–5129, 2017.

[257] S.-A. Biehs and P. Ben-Abdallah. Near-field heat transfer between multilayer hyperbolic metamaterials. *Zeitschrift für Naturforschung A*, 72:115, 2017.

[258] J.-Y. Chang, S. Basu, and L. Wang. Indium tin oxide nanowires as hyperbolic metamaterials for near-field radiative heat transfer. *Journal of Applied Physics*, 117(5):054309, 2015.

[259] J.-Y. Chang, Y. Yang, and L. Wang. Tungsten nanowire based hyperbolic metamaterial emitters for near-field thermophotovoltaic applications. *International Journal of Heat and Mass Transfer*, 87:237–247, 2015.

[260] I. E. Titkov, S. Y. Karpov, A. Yadav, V. L. Zerova, M. Zulonas, B. Galler, M. Strassburg, I. Pietzonka, H. J. Lugauer, and E. U. Rafailov. Temperature-dependent internal quantum efficiency of blue high-brightness light-emitting diodes. *IEEE Journal of Quantum Electronics*, 50(11):911–920, 2014.

[261] K. A. Bachman, J. J. Peltzer, P. D. Flammer, T. E. Furtak, R. T. Collins, and R. E. Hollingsworth. Spiral plasmonic nanoantennas as circular polarization transmission filters. *Opt. Express*, 20(2):1308–1319, 2012.

[262] W.-C. Liao, S.-W. Liao, K.-J. Chen, Y.-H. Hsiao, S.-W. Chang, H.-C. Kuo, and M.-H. Shih. Optimized spiral metal-gallium-nitride nanowire cavity for ultrahigh circular dichroism ultraviolet lasing at room temperature. *Scientific Reports*, 6:26578, 2016.

[263] C. L. Yu, S.-W. Liao, Y.-H. Hsiao, H.-C. Kuo, and M.-H. Shih. Circular polarized lasing characteristics in metal/GaN double-spiral nanowire cavity. In *Conference on Lasers and Electro-Optics*, page STh1C.4. Optical Society of America, 2017.

[264] J. D. van der Laan, J. B. Wright, D. A. Scrymgeour, S. A. Kemme, and E. L. Dereniak. Evolution of circular and linear polarization in scattering environments. *Opt. Express*, 23(25):31874–31888, 2015.

[265] J. Jin, J. Luo, X. Zhang, H. Gao, X. Li, M. Pu, P. Gao, Z. Zhao, and X. Luo. Generation and detection of orbital angular momentum via metasurface. *Nat. Commun.*, 6:24286, 2016.

[266] V. Dolores-Calzadilla, B. Romeira, F. Pagliano, S. Birindelli, A. Higuera-Rodriguez, P. J. van Veldhoven, M. K. Smit, A. Fiore, and D. Heiss. Waveguide-coupled nanopillar metal-cavity light-emitting diodes on silicon. *Nat. Commun.*, 8:14323, 2017.

[267] J. K. Kitur, L. Gu, T. Tumkur, C. Bonner, and M. A. Noginov. Stimulated emission of surface plasmons on top of metamaterials with hyperbolic dispersion. *ACS Photonics*, 2(8):1019–1024, 2015.

[268] R. Chandrasekar, Z. Wang, X. Meng, S. I. Azzam, M. Y. Shalaginov, A. Lagutchev, Y. L. Kim, A. Wei, A. V. Kildishev, A. Boltasseva, and V. M. Shalaev. Lasing action with gold nanorod hyperbolic metamaterials. *ACS Photonics*, 4(3):674–680, 2017.

[269] E. K. Lau, A. Lakhani, R. S. Tucker, and M. C. Wu. Enhanced modulation bandwidth of nanocavity light emitting devices. *Opt. Express*, 17(10):7790–7799, 2009.